



UNIVERSIDAD DE CHILE
FACULTAD DE CIENCIAS FÍSICAS Y MATEMÁTICAS
DEPARTAMENTO DE GEOLOGÍA

**ORIGEN DE LA MINERALIZACIÓN DE HIERRO DEL COMPLEJO
VOLCÁNICO LAGUNA DEL MAULE, CHILE: ¿UN NUEVO EJEMPLO DE
DEPÓSITO TIPO ÓXIDO DE HIERRO-APATITO EN LOS ANDES?**

TESIS PARA OPTAR AL GRADO DE MAGÍSTER EN CIENCIAS, MENCIÓN
GEOLOGÍA

ERNESTO ANDRÉS COFRÉ ARZOLA

PROFESOR GUÍA:

DR. MARTIN REICH MORALES

MIEMBROS DE LA COMISIÓN:

DR. FERNANDO BARRA PANTOJA

DR. DIEGO MORATA CÉSPEDES

DRA. IRENE DEL REAL CONTRERAS

Este trabajo ha sido financiado por el Núcleo Milenio Trazadores de Metales en Zonas de
Subducción (NCN13_065)

SANTIAGO DE CHILE

2022

RESUMEN DE LA TESIS PARA OPTAR AL GRADO

DE: Magíster en Ciencias mención Geología

POR: Ernesto Cofré Arzola

FECHA: 2022

PROFESOR GUÍA: Martin Reich Morales

ORIGEN DE LA MINERALIZACIÓN DE HIERRO DEL COMPLEJO VOLCÁNICO LAGUNA DEL MAULE, CHILE: ¿UN NUEVO EJEMPLO DE DEPÓSITO TIPO ÓXIDO DE HIERRO-APATITO EN LOS ANDES?

Los depósitos de óxido de hierro-apatito (IOA), también conocidos como depósitos de magnetita-apatito o tipo Kiruna, son una fuente importante de hierro y potencialmente de elementos críticos como tierras raras y cobalto. A la fecha, el representante más joven de este tipo de mineralización a nivel mundial corresponde al depósito El Lago de edad Pleistoceno (~2 Ma), un caso aparentemente único debido a sus características volcánicas y su ocurrencia en la región Altiplano-Puna de los Andes Centrales. Sin embargo, existe evidencia de mineralización de tipo IOA asociada a actividad volcánica similarmente joven (<1.0 Ma) a lo largo de los Andes de Chile, la cual no se encuentra debidamente caracterizada y estudiada.

Es en este contexto que esta investigación se centra en el estudio de un ejemplo de mineralización de tipo IOA hospedada dentro del Complejo Volcánico Laguna del Maule en los Andes Centrales del Sur. La mineralización de tipo IOA ocurre como cuerpos vetiformes y brechas de magnetita, junto a apatito, piroxeno y actinolita, y se encuentra alojada en andesitas que conforman los remanentes del volcán La Zorra (1.013 ± 0.028 Ma edad $^{40}\text{Ar}/^{39}\text{Ar}$; Hildreth et al., 2010).

El presente estudio combina observaciones de campo, levantamientos aéreos con dron, observaciones petrográficas detalladas y microanálisis mediante microsonda electrónica (EMPA) de diferentes tipos texturales de magnetita. Las relaciones de campo y la caracterización petrográfica de la mineralización de magnetita, denominada aquí “Vetas del Maule”, permitió la identificación de cinco estilos u ocurrencias: i) Magnetita masiva, ii) Vetas de piroxeno-actinolita-magnetita, iii) Brechas hidrotermales con matriz de magnetita, iv) Magnetita diseminada, y v) Vetas de piroxeno-actinolita±magnetita. Los análisis de EMPA de los distintos tipos de magnetita revelan una tendencia a la disminución progresiva de las concentraciones de elementos menores tales como Ti, V, Al, Mn y Mg, desde variedades de magnetita rica en estos elementos (ej. i-ii) hasta variedades más bien empobrecidas en ellos (ej. iii-v). Los cálculos termométricos basados en las concentraciones de Mg en magnetita indican un rango de temperatura de formación que va desde los ~950°C hasta los 500°C, en general consistente con la disminución sistemática en las concentraciones de Ti, V, Al y Mn.

Los datos microanalíticos indican que la mineralización de magnetita de Vetas del Maule se formó bajo condiciones que evolucionaron desde magmático-hidrotermales a puramente hidrotermales. Dichos datos, en conjunto con el estilo de ocurrencia de los cuerpos de magnetita (ej. vetas y brechas), apuntan a la inyección de fluidos hidrotermales en un sistema volcánico como proceso desencadenante de la mineralización, posiblemente atribuible a procesos de descompresión de un reservorio de fluido en profundidad. Estos antecedentes permiten concluir que la mineralización de magnetita de Vetas del Maule es un nuevo ejemplo de mineralización de tipo IOA asociada a volcanismo reciente en los Andes. En consecuencia, los resultados presentados en este trabajo indican que este tipo de asociación puede ser más común de lo pensado anteriormente, lo que abre nuevas oportunidades de investigación y exploración de recursos de hierro-apatito a lo largo de la Cadena Andina.

Las verdades que revela la inteligencia permanecen estériles. Sólo el corazón es capaz de fecundar los sueños.

Anatole France

Y así muchos golpes, aunque con un hacha pequeña, cortaron y derribaron el roble de madera más dura.

Shakespeare, King Henry VI, Parte III

A mi madre Viviana y a mi padre Eduardo

AGRADECIMIENTOS

Quisiera dedicar este trabajo a diversas personas que me apoyaron, motivaron, y guiaron a lo largo de la realización de esta investigación. Todos fueron importantes y en cierta forma este resultado es producto del esfuerzo colectivo de todos.

En primer lugar agradezco a los miembros de la comisión de la presente tesis, Dr. Martin Reich, Dr. Fernando Barra, Dr. Diego Morata y a la Dra. Irene del Real. En especial quisiera agradecer a mi profesor guía, el Dr. Martin Reich, quien fue una constante fuente de sabiduría y apoyo a lo largo del proceso, otorgándome el privilegio de pertenecer al NMTM, grupo dedicado a la investigación geológica de alto nivel. Un espacio así solo puede ser mantenido a través del esfuerzo constante, liderazgo y enseñanza a través del ejemplo. De igual manera agradezco al Dr. Fernando Barra, por sus valiosas contribuciones, apoyo y compartir las responsabilidades de mantener un grupo de trabajo excelente.

Agradezco también a mis colaboradores internacionales, cuya asistencia remota posibilitó esta investigación: al Dr. Artur Deditius de la U. de Murdoch que realizó de manera remota los análisis de microsonda, ejes centrales de este trabajo, así como al Dr. Adam Simon de la U. de Michigan y a Malcolm Roberts de la U. de Western Australia.

De manera muy especial agradezco a mis padres Viviana y Eduardo quienes siempre me han apoyado en todo lo que me propongo, procurando que no me falte nada, haciendo de mis metas las suyas, solo motivados por el amor. A mi hermana Fernanda que siempre estuvo ahí apoyando con su cariño. A ellos les debo todo lo que poseo y he logrado hasta aquí, su moral y trabajo constante ha sido siempre un modelo a seguir.

A mis amigos de toda la vida: “Coco” Rojas, “Turco” Candía, “Wily” Salazar, “Loto”, Maca Henríquez, Amapola Albornoz, Caro Peña, Leo Aguirre, Gus Moraga y en especial a mi querido cuasi-hermano José Arroyo. Compartimos desde siempre penas y alegrías, me recuerdan que hay un bello mundo fuera del laboral, alegran mis días con sus planes y juntas.

A mis compañeros de la oficina del NMTM con los que compartimos el codo con codo de la producción científica y varios litros de café. Gracias por brindarme su compañerismo y amistad. Siempre se producían conversaciones muy interesantes producto de la variedad de experiencias que cada quien aportaba. En especial agradezco a José Tomás Ovalle (Tomi), quien me presentó la mineralización objeto de este trabajo, realizó los primeros análisis, ayudó en terreno y apoyo siempre a lo largo del proceso y a Gisella Palma (Gilla) quien contribuyó con el cálculo de temperaturas en las fases finales que permitió darle sentido a una investigación que pudo haber sido muy dispersa. También agradezco a Ricardo Fuentealba, Diego Muñoz y Domínica Kausel por su amistad, buena disposición y ayuda en las campañas de terreno, así como la asistencia con el manejo del dron.

Finalmente, agradezco el financiamiento aportado por el Núcleo Milenio NCN13_065 Trazadores de Metales en Zonas de Subducción (NMTM) y los funcionarios del Departamento de Geología de la U. de Chile por su constante trabajo y buena disposición.

TABLA DE CONTENIDO

1.0	CAPÍTULO 1 - INTRODUCCIÓN.....	1
1.1	Estructura y organización de la Tesis	1
1.2	Motivación del estudio.....	2
1.3	Hipótesis de la investigación	4
1.4	Objetivos.....	4
1.4.1	Objetivos específicos	5
1.5	Metodologías de estudio	5
2.0	CAPÍTULO 2 - MARCO GEOLÓGICO	7
2.1	Generalidades.....	7
2.2	Unidades estratificadas	9
2.2.1	Formación Nacientes del Teno	9
2.2.2	Grupo Mendoza.....	9
2.2.3	Grupo Bajada del Agrio	9
2.2.4	Formación Cura-Mallín.....	10
2.2.5	Formación Trapa-Trapa	10
2.2.6	Formación Campanario.....	10
2.2.7	Formación Cola de Zorro	11
2.3	Complejo volcánico Laguna del Maule (CVLM).....	11
2.3.1	Volcanes y secuencias volcánicas.....	12
2.4	Rocas intrusivas	15
2.4.1	Plutón El Indio	15
2.5	Geología estructural.....	15
2.5.1	Falla Troncoso.....	15
2.5.2	Falla Laguna Fea.....	16
2.6	Geofísica	16
2.6.1	Geodesia.....	16
2.6.2	Gravimetría	17
2.6.3	Magnetotelúrica	18
2.6.4	Sismicidad.....	20

3.0	CAPÍTULO 3 - ORIGIN OF VOLCANIC-HOSTED MAGNETITE AT THE LAGUNA DEL MAULE COMPLEX, CHILE: A NEW EXAMPLE OF ANDEAN IRON OXIDE-APATITE MINERALIZATION?.....	22
3.1	ABSTRACT.....	22
3.2	INTRODUCTION	23
3.3	GEOLOGICAL SETTING.....	25
3.3.1	The Laguna del Maule Volcanic Complex	25
3.4	SAMPLES AND METHODS	27
3.5	RESULTS	28
3.5.1	Magnetite mineralization styles	28
3.5.2	Magnetite geochemistry.....	31
3.6	DISCUSSION.....	32
3.6.1	A magmatic-hydrothermal origin of magnetite	32
3.6.2	Magnetite crystallization temperatures	33
3.6.3	Magnetite microtextures and re-equilibration.....	34
3.6.4	Genetic model	36
3.7	CONCLUSIONS	39
3.8	Figures	41
3.9	References.....	51
4.0	CAPÍTULO 4 - CONCLUSIONES.....	58
	BIBLIOGRAFÍA	60
	ANEXO	66

ÍNDICE DE FIGURAS

Figure 1. Mapa geológico del CVLM.....	8
Figure 2. Sección transversal conceptual del CVLM en profundidad.....	13
Figure 3. Interferograma de apertura sintética (InSAR) del CVLM.....	17
Figure 4. Modelo de contraste de densidad 3D en la Laguna del Maule.....	18
Figure 5. Vista en planta del modelo de resistividad eléctrica del CVLM.....	19
Figure 6. Modelo de resistividad eléctrica 2D de Chile a los 36°S.....	20
Figure 7. Modelo conceptual que relaciona la estructura cortical y el sistema magmático del CVLM como una cuenca de pull-apart dextral.....	21
Figure 8. Location and Geological map of the LMVC.....	41
Figure 9. Location of the IOA-type mineralization within La Zorra volcano.....	42
Figure 10. Field photographs showing the IOA-type mineralization styles.....	43
Figure 11. Photomicrographs of Vetas del Maule IOA-type mineralization.....	44
Figure 12. SEM images of magnetite textures.....	45
Figure 13. Summary table of mineralogy and magnetite textures according to the mineralization styles.....	46
Figure 14. Bivariant plots of EMPA elemental concentrations in magnetite.....	47
Figure 15. Temperatures recorded by Mg-in-magnetite geothermometer.....	48
Figure 16. Quantitative WDS maps of selected elements in magnetite.....	49
Figure 17. Schematic genetic model for the Vetas del Maule IOA-type mineralization hosted in andesites from La Zorra volcano.....	50

CAPÍTULO 1

INTRODUCCIÓN

1.1 Estructura y organización de la Tesis

El presente trabajo se centró en el mapeo y caracterización mineralógica, microtextural y geoquímica de la mineralización de óxido de hierro-apatito o IOA —del inglés *iron oxide-apatite*— alojada en las rocas volcánicas asociadas a los remanentes del volcán La Zorra, ubicado dentro del Complejo Volcánico Laguna del Maule, Región del Maule, Chile. La estructura de la tesis se indica a continuación.

El presente capítulo introductorio (Capítulo 1) presenta la motivación que dio origen a este estudio, la hipótesis de la investigación, los objetivos tanto generales como específicos y las metodologías utilizadas en la obtención de los resultados.

En el Capítulo 2 se presenta una revisión bibliográfica de las principales características geológicas y geofísicas del Complejo Volcánico Laguna del Maule relevantes para esta investigación, así como la descripción de las principales unidades volcánicas comprendidas dentro del área de estudio.

El Capítulo 3 consiste en el manuscrito “*Origin of volcanic-hosted magnetite at the Laguna del Maule Complex, Chile: A new example of Andean iron oxide-apatite mineralization?*”, que será enviado para revisión por pares a una revista indexada. Este capítulo reúne todos los resultados obtenidos durante el desarrollo de la investigación, junto con las discusiones y el modelo genético propuesto para las mineralizaciones estudiadas.

Finalmente, en el Capítulo 4 se presenta un resumen con las principales conclusiones del estudio.

De forma adicional se incluye un Anexo que contiene las tablas de datos de análisis EMPA utilizadas en este estudio. En el caso del manuscrito del Capítulo 3 este es citado como Appendix.

1.2 Motivación del estudio

Los depósitos de óxido de hierro-apatito (IOA) o de tipo “*Kiruna*” representan al miembro extremo rico en Fe pero pobre en Cu del clan de depósitos de tipo óxido de hierro-cobre-oro, del inglés IOCG (Sillitoe, 2003; Barton, 2014). Estos depósitos son una fuente importante de hierro a nivel global, y potencialmente de elementos críticos como tierras raras y cobalto. En general, la mena predominante en los depósitos IOA corresponde a magnetita, la cual puede estar acompañada de cantidades variables de apatito (1–50% modal), actinolita, piroxeno, epidota y sulfuros de Fe-(Cu) (Williams et al., 2005). Los depósitos IOA se distribuyen de manera global presentando edades que varían desde el Proterozoico (distritos de Kiruna y Grängesberg, Suecia, y Pea Ridge y Pilot Knob, Missouri), Paleozoico (Distrito de Bafq, Irán), Cretácico (Depósitos de la “Franja Ferrífera Chilena”) y Oligoceno a Plioceno (Cerro Mercado, México, y El Laco, Chile) (Nyström y Henríquez, 1994; Jonsson et al., 2013; Childress et al., 2016; Day et al., 2016; Heidarian et al., 2016; Westhues et al., 2017a, b; Simon et al., 2018; Corona-Esquivel et al., 2018; Ovalle et al., 2018; Peters et al., 2019).

El origen de los depósitos IOA es motivo de controversia y varias hipótesis han sido propuestas para explicar su formación. Una de las hipótesis propone el emplazamiento de un fundido rico en Fe-Ca-P-H₂O previamente separado de un fundido rico en Si mediante procesos de inmiscibilidad líquida (Nyström y Henríquez, 1994; Naslund et al., 2002; Velasco et al., 2016; Tornos et al., 2016; Hou et al., 2018; Mungall et al., 2018; Bain et al., 2020, 2021). Otra hipótesis propone el reemplazo total de la mineralogía de la roca caja original por magnetita producto de la acción de fluidos hidrotermales ricos en Fe a temperaturas medias a bajas, derivados de magmas de composición intermedia (Hitzman et al., 1992; Rhodes y Oreskes, 1999; Sillitoe y Burrows, 2002; Barton y Johnson, 2004; Barton, 2014; Dare et al., 2015). Más recientemente, se ha propuesto un modelo magmático-hidrotermal basado en procesos de flotación magmática de magnetita por efecto de nucleación heterogénea de burbujas de fluido, la cual permite extraer y concentrar el Fe contenido en el magma de manera eficiente para su posterior precipitación (Knipping et al., 2015a, b; Simon et al., 2018; Palma et al., 2020).

En las últimas décadas una serie de estudios han demostrado que la composición y las microtexturas de la magnetita pueden entregar información útil para dilucidar las

condiciones de formación y evolución de depósitos IOA (Dupuis y Beaudoin, 2011; Nadoll et al., 2014; Dare et al., 2015). Sin embargo, estudios recientes han demostrado que tanto las microtexturas como la composición química de la magnetita ígnea e hidrotermal son reflejo de procesos fisicoquímicos complejos, y cuyos controles dependen de factores tales como la temperatura, presión, fugacidad de oxígeno y disponibilidad de elementos traza en el fundido y/o fluido asociado a la mineralización (Simon et al., 2018; Huang y Beaudoin, 2019).

En el contexto del margen sudamericano, y en particular del margen andino chileno, la mayoría de los depósitos IOA están concentrados principalmente en la provincia metalogénica del Cinturón de Hierro de la Cordillera de la Costa, conocido comúnmente como la “Franja Ferrífera Chilena” (Ruiz et al., 1965; Pichón, 1981; Oyarzún y Frutos, 1984; Ménard, 1990), cuyos exponentes datan del Cretácico Inferior e incluyen depósitos tales como Los Colorados, El Romeral, El Tofo o Cerro Negro Norte, emplazados en un arco volcánico inmaduro de corteza delgada (~35 km). Excepcionalmente, el depósito de El Laco correspondería a un exponente aislado emplazado en la Cordillera de Los Andes (arco volcánico actual). Este depósito es inusual debido a su ubicación en la región del Altiplano-Puna, de corteza particularmente gruesa (~60 km), su carácter subvolcánico/aéreo único con ocurrencia de texturas volcánicas similares a “lavas” de magnetita, y su edad pleistocena (~2 Ma), la más joven registrada para este tipo de depósitos a nivel mundial (Nyström y Henríquez, 1994; Sillitoe y Burrows, 2002; Naranjo et al., 2010; Tornos et al., 2016; Velasco et al., 2016; Ovalle et al., 2018).

Estudios resumidos en Palma et al. (2020) sugieren que los depósitos IOA chilenos comprenden un grupo con grados variables de afinidad magmática e hidrotermal asociadas a la profundidad de su emplazamiento. Aquí el depósito subvolcánico/aéreo de El Laco representaría el estilo o sub-tipo del clan formado a profundidades más someras. Adicionalmente Ovalle et al. (2018) ha propuesto que el origen de los depósitos IOA subvolcánico/aéreos tales como El Laco sería producto una conjunción óptima de procesos que llevaron a la concentración de hierro en un sistema volcánico activo, los cuales involucran una transición entre condiciones magmático-hidrotermales en profundidad, a puramente hidrotermales en niveles más someros.

En este estudio se reporta la existencia de mineralización afin al tipo óxido de hierro-apatito o IOA emplazada en los remanentes del volcán La Zorra (<1.0 Ma), ubicado dentro del Complejo Volcánico Laguna del Maule (CVLM), Región del Maule, Chile, en los Andes Centrales del Sur. Los cuerpos de magnetita que forman el depósito, aquí denominado “Vetas del Maule”, presentan múltiples similitudes con el depósito de El Laco en el Altiplano Chileno. El presente estudio busca caracterizar en detalle la mineralización de magnetita, su petrografía y geoquímica de elementos mayores, menores y trazas, con el fin de estimar sus condiciones de formación, aportando información acerca de la ocurrencia de mineralización de tipo IOA en el contexto Andino.

1.3 Hipótesis de la investigación

Basado en las observaciones de terreno y ocurrencias de magnetita se plantea que la mineralización de magnetita asociada al volcán La Zorra en el CVLM presenta rasgos mineralógicos y texturales acordes a los depósitos de tipo IOA.

La mineralización de magnetita descrita se habría formado de manera similar a los depósitos de magnetita de El Laco, es decir, como resultado de procesos que involucran una transición entre condiciones magmático-hidrotermales a puramente hidrotermales. Dicha transición se vería reflejada en una variación sistemática de las concentraciones de elementos tales como el Ti, V, Al, Mn y Mg en la magnetita asociada a distintos estilos u ocurrencias de mineralización.

1.4 Objetivos

En base a la hipótesis planteada, esta investigación tiene por objetivo general determinar los factores que dieron origen a la mineralización de magnetita de Vetas del Maule y establecer las condiciones bajo las cuales evolucionó el sistema volcánico-hidrotermal. Para este fin se plantea la construcción de un modelo genético de la mineralización de magnetita en base a los datos geológicos, mineralógicos, microtexturales y geoquímicos.

Con el propósito de caracterizar geológicamente la mineralización de magnetita se plantean los siguientes objetivos específicos:

1.4.1 Objetivos específicos

- Realizar un mapeo de detalle, describiendo los cuerpos en superficie, caracterizando su geometría, relaciones de contacto, disposición espacial y posición dentro del edificio volcánico.
- Describir la mineralogía de las ocurrencias de magnetita y su alteración hidrotermal asociada, identificando las fases minerales presentes, sus microtexturas y relaciones paragenéticas.
- Determinar la composición química de elementos mayores, menores y trazas en la magnetita, con el propósito de constreñir el ambiente de formación (ígneo, magmático-hidrotermal o hidrotermal) y la temperatura de cristalización.
- Establecer relaciones entre las ocurrencias macroscópicas de los cuerpos, la geoquímica y microtexturas de la magnetita.
- Comparar las características geológicas, mineralógicas, microtexturales y geoquímicas observadas con las de otros depósitos de tipo IOA con énfasis en el depósito subvolcánico/aéreo El Laco, y proponer un modelo genético para la mineralización de magnetita.

1.5 Metodologías de estudio

- Se recopilaron los antecedentes geológicos y geofísicos de la zona de estudio. Adicionalmente se realizó una revisión de estudios anteriores relacionados con la génesis de depósitos de tipo IOA.
- Se efectuaron tres campañas de terreno durante abril de 2017, enero de 2019 y enero de 2020 con el objetivo establecer la ubicación de los cuerpos mineralizados, realizar un mapeo de superficie y toma de muestras. Para esta última se favorecieron afloramientos representativos de la ladera sureste del volcán La Zorra, donde se emplaza la mineralización de tipo IOA.
- Durante la campaña de terreno del año 2020 se obtuvieron fotografías aéreas del volcán utilizando un dron DJI Mavic 2 Pro quadcopter equipado con una cámara de

20 MP, operado a través de la aplicación “DroneDeploy” con el objeto de complementar las observaciones en terreno y construir un modelo de elevación digital 3D del volcán La Zorra. El modelo se elaboró utilizando los softwares Agisoft Metashape Professional y ArcGIS arcScene.

- Se confeccionó un proyecto GIS con la información recopilada en la bibliografía, imágenes satelitales, imágenes aéreas e información de terreno.
- Se realizó la descripción petrográfica de cortes transparentes pulidos de muestras seleccionadas mediante un microscopio petrográfico en el Laboratorio de Microscopia del Departamento de Geología de la Universidad de Chile. En combinación al análisis de muestras de mano, se describió la mineralogía, principales alteraciones y paragénesis de los cuerpos mineralizados.
- Se complementó la descripción petrográfica de los cortes transparentes mediante la utilización de un microscopio electrónico de barrido (SEM) FEI Quanta 250, para lo cual se cubrieron con una película de carbono. La técnica permitió además estudiar las relaciones microtexturales, patrones de zonación, inclusiones minerales, exsoluciones y sobrecrecimientos en las diversas fases minerales con énfasis en la magnetita. Se complementó la identificación de las diversas fases minerales realizando análisis químicos semicuantitativos mediante un detector de electrones retrodispersados (BSE), incorporado en el microscopio electrónico.
- En colaboración con el Dr. Artur Deditius y el Dr. Malcolm Roberts se efectuaron microanálisis EMPA en magnetita en el Centre of Microscopy, Characterisation and Analysis (CMCA) of the University of Western Australia, utilizando una microsonda electrónica JEOL JXA8530F Plus. Además se realizaron mapas de espectrometría de dispersión de longitud de onda de rayos X (WDS) en granos de magnetita seleccionados.
- Se determinaron las temperaturas de cristalización de la magnetita mediante el geotermómetro empírico de Mg en magnetita propuesto por Canil y Lacourse (2020). Las concentraciones de Mg para los cálculos fueron obtenidas del análisis EMPA.

Una descripción más detallada de los métodos utilizados se presenta en el Capítulo 3.4 *Samples and Methods*. Las condiciones en que se realizaron los análisis EMPA están incorporadas en el anexo.

CAPÍTULO 2

MARCO GEOLÓGICO

2.1 Generalidades

El Complejo Volcánico Laguna del Maule (CVLM) se ubica dentro del arco volcánico andino, específicamente en la Zona Volcánica Sur Transicional (ZVST), que corresponde a una franja de 300 km de N a S entre los 34.5°–37° S donde el arco alcanza un ancho de ~150 km (Fig. 1A), la corteza en general posee un espesor de entre 35–40 km y hasta de 40-50 km bajo el CVLM (Hildreth y Moor bath, 1988; Hildreth et al., 2010). Desde un punto de vista tectónico, la ZVST se caracteriza por una convergencia dextral-oblicua entre las placas de Nazca y Sudamericana con una tasa de convergencia de 7–9 cm/año que ha sido relativamente constante durante los últimos 20 Ma (Pardo-Casas y Molnar, 1987). Esto ha generado un contexto transpresivo en esta sección del arco volcánico (Arancibia et al., 1999; Lavenu y Cembrano, 1999; Cembrano et al., 2002; Melnick et al., 2006).

La geología de los Andes en la Región del Maule está conformada por afloramientos cenozoicos y mesozoicos distribuidos a lo largo de la Cordillera Principal Occidental y Oriental. Componentes del orógeno que son prominentes más al norte (Sierras Pampeanas, Precordillera o Cordillera Frontal) no están presentes a esta latitud, y en su lugar la vertiente oriental de la Cordillera Principal es parte de la faja corrida y plegada de piel gruesa de Malargüe (Hildreth et al., 2010). La extensión más meridional de esta faja se dispone al este del CVLM, presentando abundantes afloramientos sedimentarios y volcano-sedimentarios mesozoicos y cenozoicos (Fig. 1A) (Pose, 2007). Hacia el oeste el CVLM colinda con el Complejo Volcánico Tatara-San Pedro, activo desde el Plioceno al Holoceno (Fig. 1A) (Siebert et al., 2011).

En el CVLM propiamente tal no existen afloramientos de rocas mesozoicas, aunque sí hay afloramientos cercanos en el Cajón Troncoso, aproximadamente 12 km hacia el SW, y más allá del Paso Pehuenche hacia el este, a partir de unos 10 km desde la Laguna del Maule (Fig. 1A) (Hildreth et al., 2010). Las rocas mesozoicas corresponden a secuencias sedimentarias marinas y continentales depositadas en cuencas de trasarco paralelas al arco desde el Jurásico Inferior al Cretácico Inferior, asociadas a transgresiones y regresiones

marinas (Charrier et al., 1996; Flynn et al., 2003, 2007). Las rocas cenozoicas cubren la mayoría de la Cordillera Principal Occidental y corresponden a rocas volcano-sedimentarias con diversos grados de deformación y rocas volcánicas que cubren unidades más antiguas (Fig. 1A). El arco volcánico cuaternario alcanza unos 60 km de ancho a esta latitud (36°).

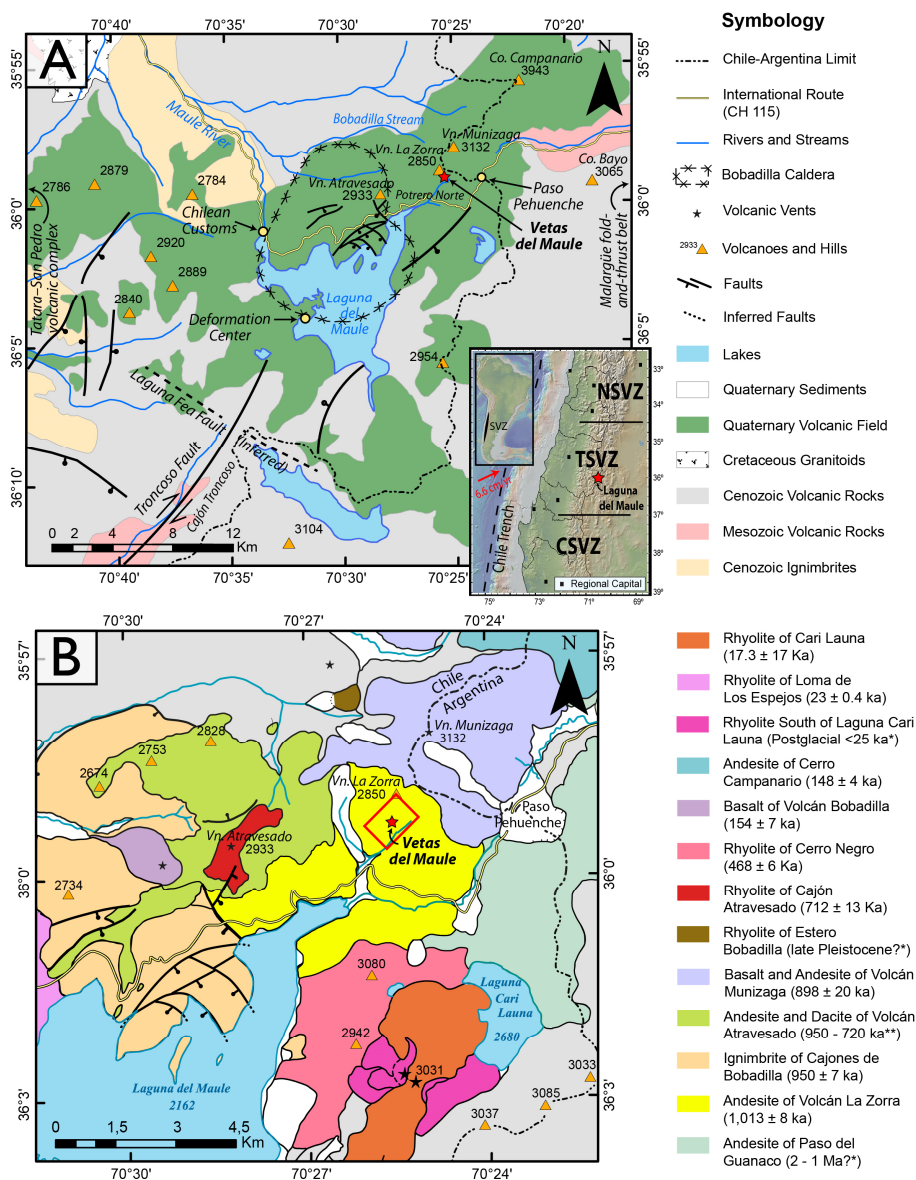


Figura 1. Mapa geológico del CVLM. (A) Mapa a escala 1:350,000 que muestra rocas pre-cuaternarias expuestas alrededor del CVLM. SVZ: zona volcánica sur; NSVZ: SVZ del norte; TSVZ: SVZ transicional; CSVZ: SVZ central. (B) Mapa geológico a escala 1:115,000 con las unidades volcánicas del sector NE del CVLM. Mapas, unidades y sus edades modificados de Hildreth et al. (2010). El trazado de las fallas se obtuvo de Muñoz y Niemeyer (1984), Hildreth et al. (2010) y Cardona et al. (2018). La ubicación del centro de deformación se obtuvo de Feigl et al. (2014). Edades de las unidades corresponden principalmente a dataciones $^{40}\text{Ar}/^{39}\text{Ar}$. Aquellas indicadas con (*) a edades estimadas estratigráficamente, y con (**) a rango estimado a partir de dataciones K/Ar.

2.2 Unidades estratificadas

2.2.1 Formación Nacientes del Teno (Jurásico Inferior – Jurásico Superior)

Secuencia sedimentaria de más de 400 m de espesor integrada por areniscas, areniscas calcáreas, lutitas, lutitas calcáreas y calizas de origen marino localmente con fauna de amonites. Se encuentra expuesta en pequeños afloramientos a lo largo del Cajón Troncoso. Suprayacen mediante discordancia angular a los Estratos Cajón Troncoso e infrayacen a las tobas de los Estratos del Estero Cristales. Estas dos últimas formaciones afloran de manera muy acotada en el mismo sector (Muñoz y Niemeyer, 1984).

2.2.2 Grupo Mendoza (Jurásico Superior – Cretácico Inferior)

En el contexto local, las rocas de este grupo están expuestas y asociadas a la faja corrida y plegada de Malargüe, aproximadamente unos 10 km al este del área de estudio. En esta zona el grupo se encuentra representado por: areniscas y pelitas rojas continentales de la Formación Tordillo (Jurásico Superior), pelitas y pelitas calcáreas con contenido fosilífero de la Formación Vaca Muerta (Jurásico Superior – Cretácico Inferior) y una intercalación de pelitas negras y calizas fosilíferas de la Formación Agrio (Cretácico Inferior). El espesor del grupo excede los 2,000 metros de espesor. Las tres formaciones se disponen de manera concordante entre sí. La Formación Tordillo se dispone discordantemente sobre evaporitas marinas de la Formación Aquilco (que aflora más al sur) hacia la base y la Formación Huitrín se dispone de manera paraconcordante a la Formación Agrio hacia techo (Pose, 2007).

2.2.3 Grupo Bajada del Agrio (Cretácico Inferior – Cretácico Superior temprano)

De manera similar al Grupo Mendoza, las rocas de este grupo se localizan en el sector de la faja corrida y plegada de Malargüe hacia el este. En esta zona el grupo se encuentra representado por niveles de pelitas calcáreas, areniscas finas, yeso y anhidrita de la Formación Huitrín y areniscas medias a gruesas con intercalaciones de niveles y conglomerádicos de la Formación Rayoso. Sus espesores en la zona son de 270 m y 50 m, respectivamente. En el contexto local, la Formación Huitrín se presenta con base y techo paraconcordante con las Formaciones Agrio y Rayoso, mientras que la Formación Rayoso se encuentra limitada hacia el techo por sedimentitas del Grupo Neuquén que aflora más al sur (Pose, 2007).

2.2.4 *Formación Cura-Mallín (Oligoceno tardío – Mioceno temprano)*

En el área cercana a la Laguna del Maule, esta formación aflora principalmente en el sector del Cajón Troncoso. En el sector está compuesta por una secuencia de rocas piroclásticas, sedimentitas clásticas y coladas de lava subordinadas, de composición intermedia. A estas latitudes (36°–37°) se dispone la subcuenca norte, conocida como depocentro de Chillán que posee más de 2,000 m de espesor (aunque es menor en el Cajón Troncoso). La base de la Formación Cura-Mallín se apoya mediante discordancia angular, sobre la Formación Nacientes del Teno e infrayace en concordancia, a las rocas de la Formación Trapa-Trapa y, con discordancia angular, a las rocas de las Formación Campanario, Cola de Zorro y unidades del volcanismo cuaternario (Muñoz y Niemeyer, 1984; Folguera y Ramos, 2001; Hildreth et al., 2010).

2.2.5 *Formación Trapa-Trapa (Mioceno medio – Mioceno superior)*

Corresponde a una secuencia de lavas andesíticas, rocas volcanoclásticas y sedimentitas continentales que aflora principalmente hacia el suroeste de la Laguna del Maule y puntualmente en sectores del Cajón Troncoso, en el Estero Cristales. Posee un espesor de entre 200 y 1,200 m dependiendo del nivel alcanzado por la erosión. Cubre de manera concordante y transicional a la Formación Cura-Mallín y su techo lo constituye la superficie de discordancia que la separa de las formaciones Cola de Zorro y Campanario (Muñoz y Niemeyer, 1984).

2.2.6 *Formación Campanario (Mioceno superior – Plioceno inferior)*

Se designa de este modo a la secuencia de tobas, tobas brechosas, brechas, ignimbritas y coladas de lava andesíticas a dacíticas que afloran en los alrededores y norte de la Laguna del Maule. La formación posee un espesor de más de 300 m y cubre en discordancia angular a las formaciones Nacientes del Teno, Cura-Mallín y Trapa-Trapa e infrayace concordantemente a la Formación Cola de Zorro (Muñoz y Niemeyer, 1984). Basado en el criterio de autores previos, Muñoz y Niemeyer (1984) integró en esta formación a todas las rocas cenozoicas pre-pleistocenas del sector de Laguna del Maule. Cabe destacar que en el área adyacente a la Laguna del Maule Hildreth et al. (2010), basado en la composición química y edades obtenidas mediante datación $^{40}\text{Ar}/^{39}\text{Ar}$, considera varios afloramientos asignados anteriormente a la Formación Campanario como unidades de lava individualizadas

asociadas a centros eruptivos desde el Pleistoceno hasta la actualidad, en particular los afloramientos al norte de la Laguna del Maule.

2.2.7 *Formación Cola de Zorro (Plioceno – Pleistoceno)*

Esta formación agrupa varios afloramientos de lavas máficas e intermedias que se disponen subhorizontales y sin deformar provenientes de varios centros de erupción sin identificar. Estas rocas han sido interpretadas como asociadas a erupciones fisurales. La formación se encuentra ampliamente distribuida a lo largo de la parte axial de los Andes con espesores variables entre 400 y 1,500 m. Suprayace en discordancia angular, a la Formación Cura-Mallín, y en forma concordante, a la Formación Campanario. Está cubierta en discordancia de erosión por los conos volcánicos y lavas del volcanismo Pleistoceno-Holoceno y por depósitos morrénicos y piroclásticos (Muñoz y Niemeyer, 1984; Melnick et al., 2006). De manera similar a la Formación Campanario, en el área adyacente a la Laguna del Maule Hildreth et al. (2010) reasignó varios de sus afloramientos a unidades de lava individualizadas asociadas a centros eruptivos desde el Pleistoceno hasta la actualidad.

2.3 **Complejo volcánico Laguna del Maule (CVLM)**

El CVLM corresponde a un complejo volcánico de aproximadamente 500 km² de extensión alrededor de una caldera volcánica de 15 × 25 km centrada en el extremo norte del lago homónimo. El complejo comprende un enjambre de pequeños estratovolcanes, domos de lava y conos piroclásticos de edad pleistocena a holocena, con composiciones desde basaltos a riolitas (Hildreth et al., 2010). Su actividad eruptiva comenzó hace 1.5 Ma con la formación de la Caldera Bobadilla y termina con la última erupción efusiva hace 2,000 años. Se han estimado por lo menos 50 erupciones que forman más de 36 domos riolíticos y riodacíticos (Hildreth et al., 2010; Singer et al., 2018). Se ha detectado una significativa tasa de deformación anual bajo el CVLM, lo que corresponde a una de las deformaciones verticales asociadas a volcanes más grandes a nivel mundial (Fournier et al., 2010; Feigl et al., 2014; Le Mével et al., 2016; Singer et al., 2018; Novoa et al., 2019).

Basados en estudios detallados de las unidades volcánicas post-glaciales de los últimos 25 ka, varios autores han sugerido que las erupciones del CVLM derivan de un

mismo sistema magmático silícico integrado (Andersen et al., 2013, 2017; Singer et al., 2014, 2018). Entre la evidencia más prominente se incluye que (i) las erupciones andesíticas y riolíticas concentradas en el sector oeste de la laguna se corresponden con erupciones coetáneas riolíticas en el sector sur y este de la laguna (separadas 10–12 km), con composiciones de elementos mayores y trazas casi idénticas, y (ii) que aunque las erupciones máficas han sido más bien ocasionales, existe evidencia de inyecciones frecuentes de magma máfico en la riolita de todo el complejo, lo que indicaría la existencia de un cuerpo de magma extenso y de baja densidad bloqueando el ascenso del magma máfico (Singer et al., 2014, Andersen et al., 2017).

En consecuencia, se ha propuesto un modelo de “*mush* magmático” en profundidad basado en el modelo de Hildreth (2004), donde el sistema magmático se dispone como una capa relativamente delgada de granitoide solidificado contra la roca caja, dentro del cual hay un *mush* rígido de cristales con menor fundido intersticial (Fig. 2). Este se mantendría parcialmente fundido producto del constante flujo de calor e inyecciones de magma máfico en las partes basales del sistema (Singer et al., 2014).

El amalgamamiento de lentes de fundido cerca del techo crearía una zona de barrera de baja densidad, pobre en cristales y dominada por fundido, que bloquearía el ascenso del magma máfico hacia la superficie (Fig. 2). Esta zona de barrera a su vez constituiría un reservorio magmático segregado y diferenciado que puede alimentar erupciones riolíticas. Se estima que producto de la expansión lateral esta zona-reservorio tendría una forma de disco aplanado hacia los bordes, lugar donde se concentraría el estrés estructural y se generaría la formación de diques periféricos (Singer et al., 2014). Los cambios en el grosor local de esta zona propiciarían el ascenso hacia la superficie de lavas más diferenciadas donde sea más grueso, es decir en la zona sur y este de la laguna, o menos diferenciadas donde sea más delgado, en la zona norte y oeste de la laguna (Andersen et al., 2017).

2.3.1 *Volcanes y secuencias volcánicas*

El CVLM ha tenido pocos edificios mayores, sin embargo, ha eruptado más de 250 km³ de productos en los últimos 1.5 Ma desde al menos 130 centros de emisión identificados (Hildreth et al., 2010). Hildreth et al. (2010) definió más de 100 unidades volcánicas, describiendo detalladamente y datando mediante ⁴⁰Ar/³⁹Ar más de 60 de ellas, sin embargo,

solo se profundizará en las más relevantes para esta investigación. A continuación se describe la unidad volcánica “Andesitas del Volcán La Zorra” en donde se emplaza la mineralización de tipo IOA estudiada aquí, así como las unidades volcánicas adyacentes a modo de contexto.

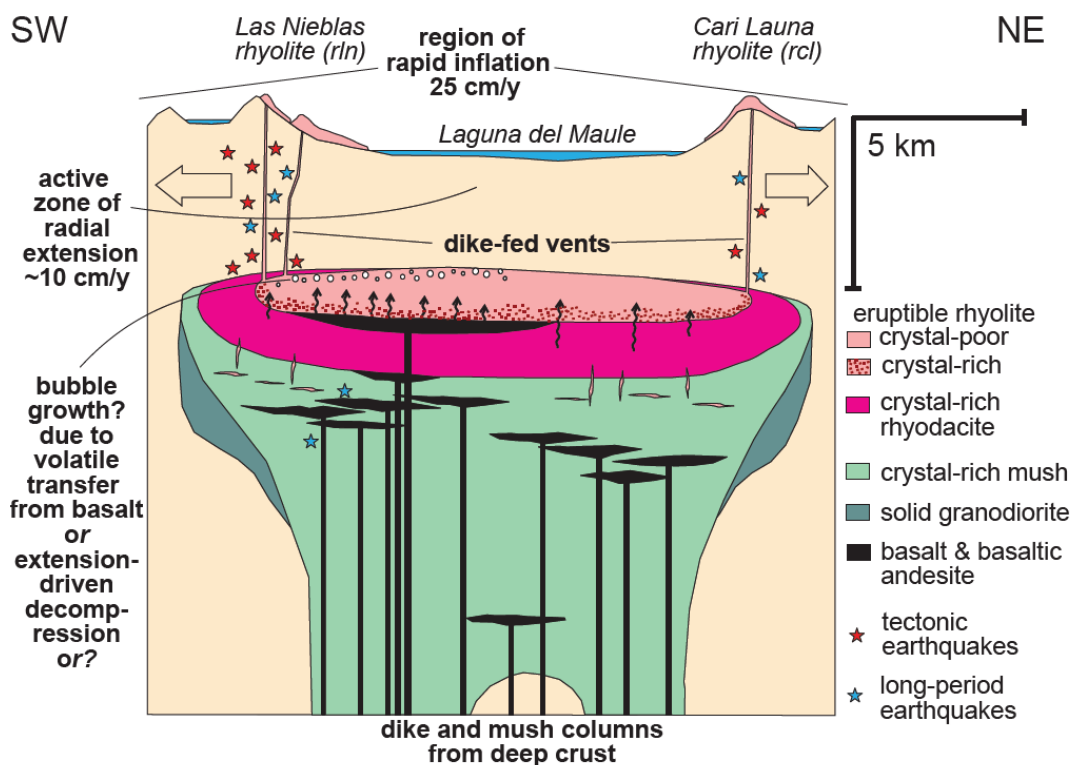


Figura 2. Sección transversal conceptual del CVLM en profundidad basada en el modelo de *mush* magmático de Hildreth (2004). Obtenido de Singer et al. (2014).

2.3.1.1 Andesitas del Volcán La Zorra

Unidad asociada a un estratocono de forma radial en forma de caldera formada a partir de una erupción explosiva cuaternaria centrado 3 km al SW del Paso Pehuenche, al NE de la Laguna del Maule. Presenta alteración hidrotermal y está severamente erosionado. La unidad posee una composición andesítica con 58–62 % de SiO₂ y posee dos dataciones; una con el método K/Ar de 1.16 ± 0.04 Ma (Drake, 1976) y otra con el método ⁴⁰Ar/³⁹Ar de 1.013 ± 0.028 Ma (Hildreth et al., 2010). Sus lavas poseen abundante ortopiroxeno, clinopiroxeno, fenocristales de plagioclasa y algunos flujos también tienen anfíbol subordinado (Hildreth et al., 2010). El área de estudio y mineralización de Vetas del Maule se encuentra totalmente contenida dentro de esta unidad litológica.

2.3.1.2 Basalto y Andesita del Volcán Munizaga

Corresponde a un estratocono máfico centrado 2 km al NW del Paso Pehuenche. La unidad presenta un 50–55 % de SiO₂. Posee fenocristales de plagioclasa y en menor cantidad olivino y clinopiroxeno. Mediante el método ⁴⁰Ar/³⁹Ar se ha obtenido una edad de 0.898 ± 0.02 Ma. Sobreyace las lavas del volcán La Zorra por el norte y noreste (Hildreth et al., 2010).

2.3.1.3 Andesita del Paso del Guanaco

Paquete de al menos nueve flujos de andesitas de piroxeno, notoriamente laminados, ubicados sobre la frontera entre Chile-Argentina desde la Laguna Cari Launa hasta el Paso Pehuenche. Presenta un 55–62% de SiO₂. La unidad está escasamente descrita y no se menciona su relación estratigráfica con las Andesitas del Volcán La Zorra. Hildreth et al. (2010) le asigna un rango de edad de 2–1 Ma sujeto a gran incertidumbre y sugiere que su centro eruptivo correspondería al Cerro Bayo (sin cartografiar), 5 km hacia el este de la frontera Chile-Argentina.

2.3.1.4 Riolitas de Cerro Negro

Domo riolítico ubicado inmediatamente adyacente al flanco NE de la Laguna del Maule. La unidad posee composiciones entre 75–78% de SiO₂. Contiene 1–3% modal de fenocristales de plagioclasa y algo de biotita. El flujo laminar es predominante, por lo que se deduce que la unidad se compone del apilamiento de finos flujos de lava y ceniza. Sobreyacen a las lavas del volcán La Zorra por el sur. Posee dos dataciones, una con el método K/Ar de 0.447 ± 0.007 Ma (Drake, 1976) y otra con el método ⁴⁰Ar/³⁹Ar de 0.468 ± 0.006 Ma (Hildreth et al., 2010).

2.3.1.5 Andesitas y Dacitas del Volcán Atravesado

Conjunto de lavas andesíticas intermedias disectadas por erosión glacial intensa ubicada inmediatamente al norte de la Laguna del Maule. No se aprecia una caldera central pero se ha deducido que esta se encontraba al interior de la Caldera Bobadilla, sobre lo que hoy es la Laguna del Maule. Posee un amplio rango de contenido de sílice que fluctúa entre 54–65%. Presenta un contacto difuso y casi horizontal con las lavas del volcán La Zorra por el oeste. Posee una datación con el método K/Ar de 0.720 ± 0.080 Ma (Drake, 1976) aunque se le estima un rango de edad entre los 0.95 y los 0.72 Ma (Hildreth et al., 2010).

2.4 Rocas intrusivas

No se registran unidades intrusivas al interior del CVLM propiamente tal. Solo se tiene registro de algunos cantos rodados de granodiorita de hornblenda-biotita en los sectores de la Laguna Cari Launa y sobre el cono de escoria de Cerro Negro, sin haberse identificado su afloramiento (Hildreth et al., 2010). El cuerpo intrusivo de importancia más cercano corresponde al plutón El Indio ubicado un par de kilómetros al NW del CVLM.

2.4.1 Plutón El Indio (o Los Indios)

Intrusivo tonalítico a granodiorítico de gran tamaño que aflora hacia el NW del CVLM, a lo largo de una franja norte-sur desde 6 km al sur de la confluencia de Ríos de La Plata y Maule hasta 4 km al norte del Río Puelche. El contenido de sílice varía entre 54–68% (Hildreth et al., 2010). Al lado oeste del intrusivo afloran rocas cretácicas mientras que en el sector este se encuentran unidades de lavas e ignimbritas neógenas a cuaternarias. Posee una datación en biotita con el método $^{40}\text{Ar}/^{39}\text{Ar}$ de 79.8 a 79.4 Ma (Nelson et al., 1999).

2.5 Geología estructural

Las estructuras presentes a nivel regional se agrupan en dos dominios estructurales con orientaciones principales N-S a NNE-SSW. A su vez, al este existe el dominio de la cuenca de trasarco mesozoica que posee principalmente fallas inversas de vergencia al E y el dominio de la Cuenca de Abanico al oeste que consiste en fallas inversas de vergencia E y W. Ambas presentan fallas con un nivel de despegue de aproximadamente 10 km de profundidad (Astaburuaga, 2014).

2.5.1 Falla Troncoso

Corresponde a la falla principal en la zona del CVLM y se extiende desde el borde SW de la Laguna del Maule hasta 30 km al SW (González y Vergara, 1962). Es de carácter dextral con una leve componente normal y tiene una orientación aproximada N45°E, coincidiendo con el Cajón Troncoso. Cardona et al. (2018) sugieren que la falla continua en su proyección hacia el NE de la laguna en la zona de Potrero Norte, donde se observan fallas con orientaciones N35–45°E.

2.5.2 *Falla Laguna Fea*

Falla inferida mediante sísmica con orientación WNW-ESE que se especula interceptaría a la falla Troncoso al SW de la Laguna del Maule. Esta falla sería principalmente normal con una leve componente sinistral (Cardona et al., 2018).

En la Figura 1 se presenta el mapa geológico del CVLM con las unidades litológicas y estructuras más relevantes para esta investigación. Las unidades estratificadas mesozoicas y cenozoicas están representadas de manera generalizada (Fig. 1A), mientras que las unidades más relevantes del volcanismo cuaternario se encuentran diferenciadas en unidades específicas basadas en el trabajo de Hildreth et al. (2010) (Fig. 1B).

2.6 **Geofísica**

2.6.1 *Geodesia*

Estudios geofísicos recientes que utilizan sistemas de posicionamiento global (GPS) de alta precisión han registrado un importante cambio de volumen de carácter anual por debajo del CVLM, correspondiente a una de las mayores deformaciones verticales registradas en un complejo volcánico (Fournier et al., 2010; Feigl et al., 2014; Le Mével et al., 2016; Singer et al., 2018; Novoa et al., 2019). Esto ha sido interpretado como inflación de una cámara magmática o inyección de fluidos hidrotermales (Fournier et al., 2010).

Esta deformación ha sido analizada y modelada mediante Radar Interferométrico de Apertura Sintética (InSAR) y Sistema Global de Navegación por Satélite (GNSS) (Fig. 3) por diversos autores (Feigl et al., 2014; Le Mével et al., 2016; Singer et al., 2018; Novoa et al., 2019). Estos autores han propuesto un modelo numérico que consiste en la intrusión de un sill riolítico de forma rectangular “plano” con dimensiones de 9 km × 5 km, con rumbo N14°E y manteo de 20° respecto a la horizontal, ubicado a 5 km de profundidad bajo la Laguna del Maule. Este se abriría de 60 a 100 cm/año perpendicular a su rumbo debido a la continua inyección de magma (Feigl et al., 2014) (Fig. 4).

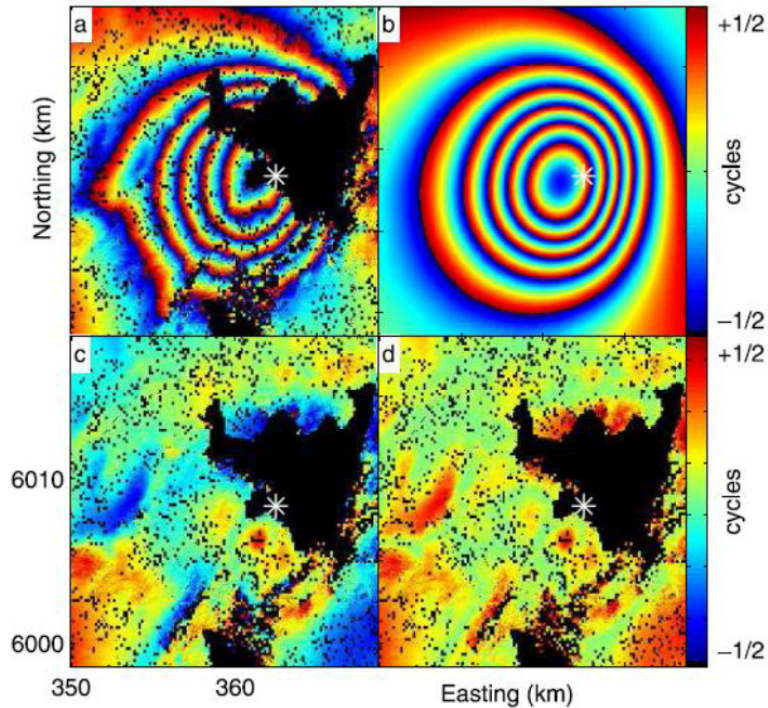


Figura 3. Interferograma de apertura sintética (InSAR) que muestra el centro de mayor alzamiento superficial en el CVLM. Cada ciclo de fase, es decir, el cambio de color de azul al rojo dentro de una misma banda, representa un cambio de 118.1 mm en la altura medida con respecto a la próxima franja. Franjas más estrechas indican mayor elevación en un mismo tiempo. Modificado de Feigl et al. (2014).

2.6.2 Gravimetría

Por otro lado, estudios gravimétricos han detectado un cuerpo de baja densidad (1.7 g/cm^3) a 1.3 km de profundidad bajo la zona de mayor alzamiento. Esta es interpretada como fluidos hidrotermales que ascienden desde cuerpos magmáticos ubicados a 10 km de profundidad utilizando zonas de fractura.

Además se ha detectado un cambio de baja densidad ($156 \text{ a } 307 \text{ kg/m}^3$), localizado desde 1.5 a 2 km de profundidad al SW de la Laguna del Maule (Fig. 4) interpretado como fluidos hidrotermales que llenan poros preexistentes de la roca (Miller et al., 2017a).

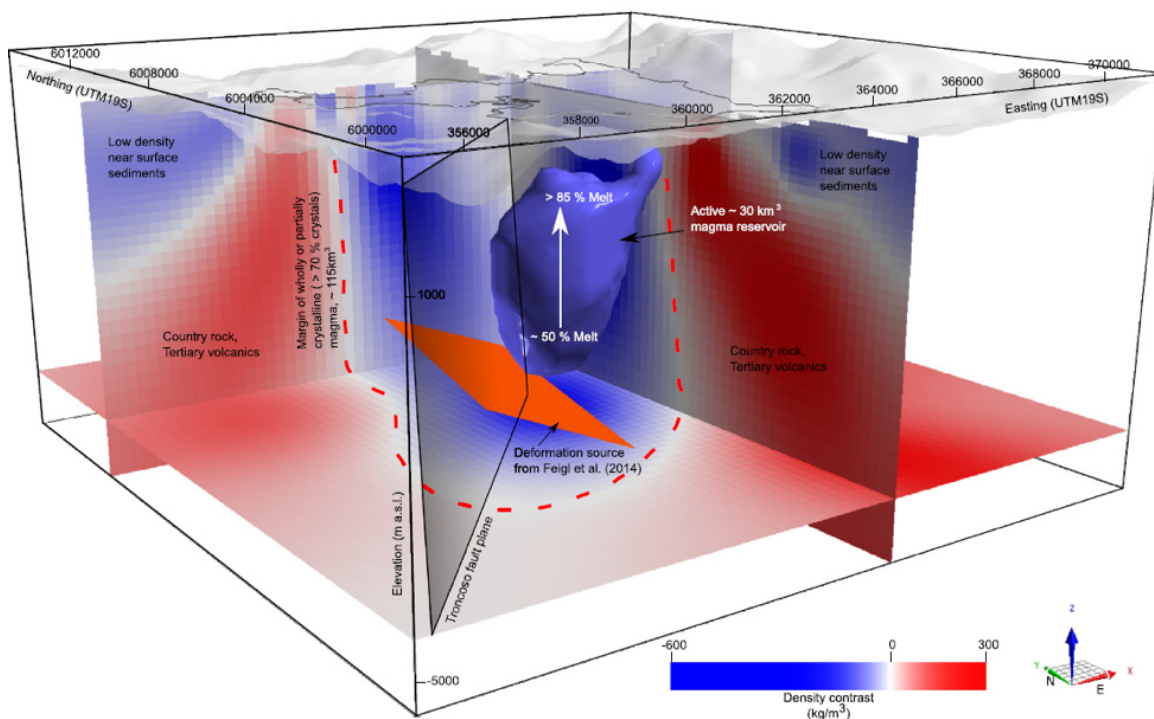


Figura 4. Modelo de contraste de densidad 3D en la Laguna del Maule y alrededores. En azul se muestran las zonas de baja densidad interpretadas como zonas de fusión parcial de magma y/o fluidos hidrotermales. El plano vertical y transparente con marco negro y orientación NE representa la falla Troncoso. El rectángulo rojo representa el sill riolítico propuesto por Feigl et al. (2014). Obtenido de Miller et al. (2017a).

2.6.3. Magnetotelúrica

Estudios de magnetotelúrica han descrito cuatro cuerpos conductivos a distintas profundidades bajo el CVLM (Fig. 5) (Cordell et al., 2018):

- **(C1):** Un cuerpo de $0,5 \Omega\text{m}$ ubicado a 200 m de profundidad bajo la Laguna del Maule, con un espesor aproximado de 200 m en forma de parches aparentemente discretos alrededor y bajo la laguna interpretados como capas de esmectitas relacionadas a un reservorio hidrotermal.
- **(C2):** Un cuerpo de $<10 \Omega\text{m}$ desde 1 km de profundidad, con un espesor aproximado de 1 km, en la misma ubicación que la anomalía gravimétrica de Miller et al. (2017a) y el centro de mayor alzamiento superficial identificado con geodesia por Fournier et al. (2010) y Feigl et al. (2014). Se ha sugerido que podrían corresponder a fluidos hidrotermales.

- **(C3):** Dos cuerpos entre los 4 km y 6 km de profundidad, con un espesor aproximado de 2 km, tanto al NW como NE de la laguna (este último aproximadamente bajo la ladera norte del volcán La Zorra) interpretados como un fundido riolítico hidratado (>5 wt% H₂O) y una componente de agua hidrotermal libre. Su ubicación es consistente con las mediciones geodésicas y gravimétricas.
- **(C4):** Un cuerpo a 8 km bajo la superficie y espesor indefinido en profundidad con centro ubicado aproximadamente 4 km desde el borde norte de la laguna e interpretado como un reservorio magmático que proporciona magma y fluidos hidrotermales a los reservorios magmáticos más someros.

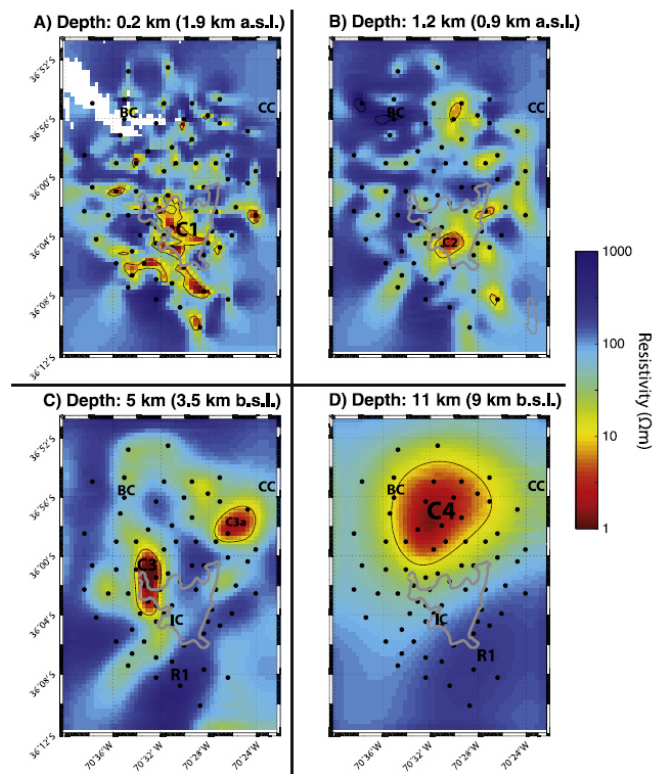


Figura 5. Vista en planta del modelo de resistividad eléctrica del CVLM a distintas profundidades. BC = sector de Baños Campanario, CC = Cerro Campanario, IC = Centro de la Deformación, a.s.l. = above sea level, b.s.l. = below sea level. Laguna del Maule delimitada en gris. En rojo cuerpos de alta conductividad eléctrica. Modificado de Cordell et al. (2018).

Adicionalmente, Reyes-Wagner et al. (2017) realizaron mediciones magnetotelélicas regionales desde la Cordillera de la Costa hasta la Precordillera, a los 36° S (Fig. 6). A partir de estos análisis se ha interpretado que existe un cuerpo magmático bajo el Complejo

Volcánico Tatara-San Pedro identificado como una cámara profunda y otros cuerpos conductivos bajo el CVLM identificados como una cámara magmática más somera, o un reservorio de fluidos hidrotermales.

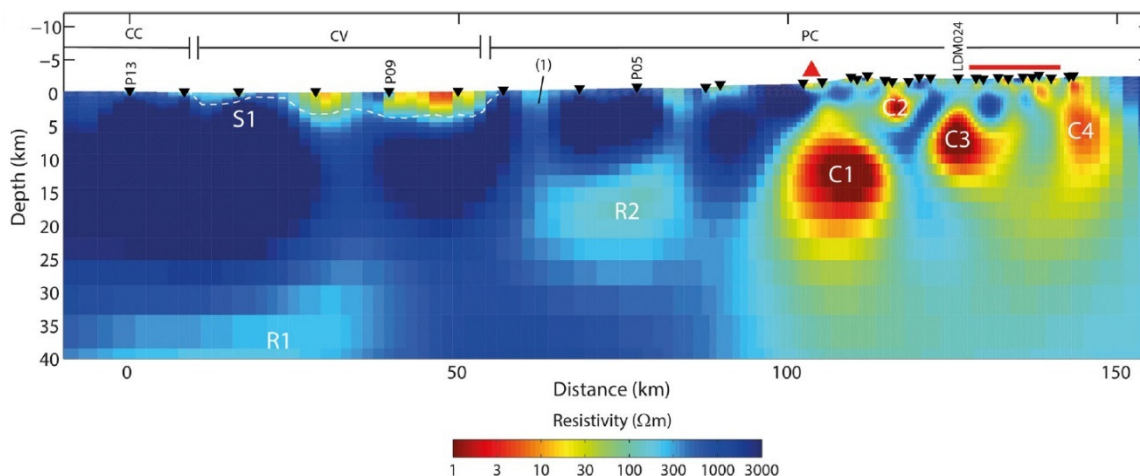


Figura 6. Modelo de resistividad eléctrica 2D de Chile a los 36°S. El triángulo rojo representa el Complejo Volcánico Tatara-San Pedro y el rectángulo rojo representa el CVLM. En rojo se muestran los cuerpos de alta conductividad eléctrica, interpretados como magma y/o fluidos hidrotermales. Modificado de Reyes-Wagner et al. (2017).

2.6.4 Sismicidad

También existen análisis de información sísmica obtenida entre abril de 2011 y diciembre de 2014 bajo los complejos volcánicos Tatara-San Pedro y Laguna del Maule (Cardona et al., 2018). Estos muestran una concentración de sismos en la intersección de la falla Troncoso con la falla Laguna Fea, cerca del lugar donde se ha registrado el valor máximo de alzamiento de la superficie obtenido mediante geodesia (Fig. 7). Esto ha sido interpretado como el producto de la interacción de la falla con un reservorio hidrotermal altamente presurizado y confinado. Esto es consistente con la localización de actividad de los sismos de tipo LP y TR, comúnmente asociados a movimientos de fluidos. Los sismos ubicados bajo el CVLM se ubican a una profundidad aproximada de 4 a 6 km, lo que coincide con las anomalías obtenidas mediante métodos magnetoteléuricos.

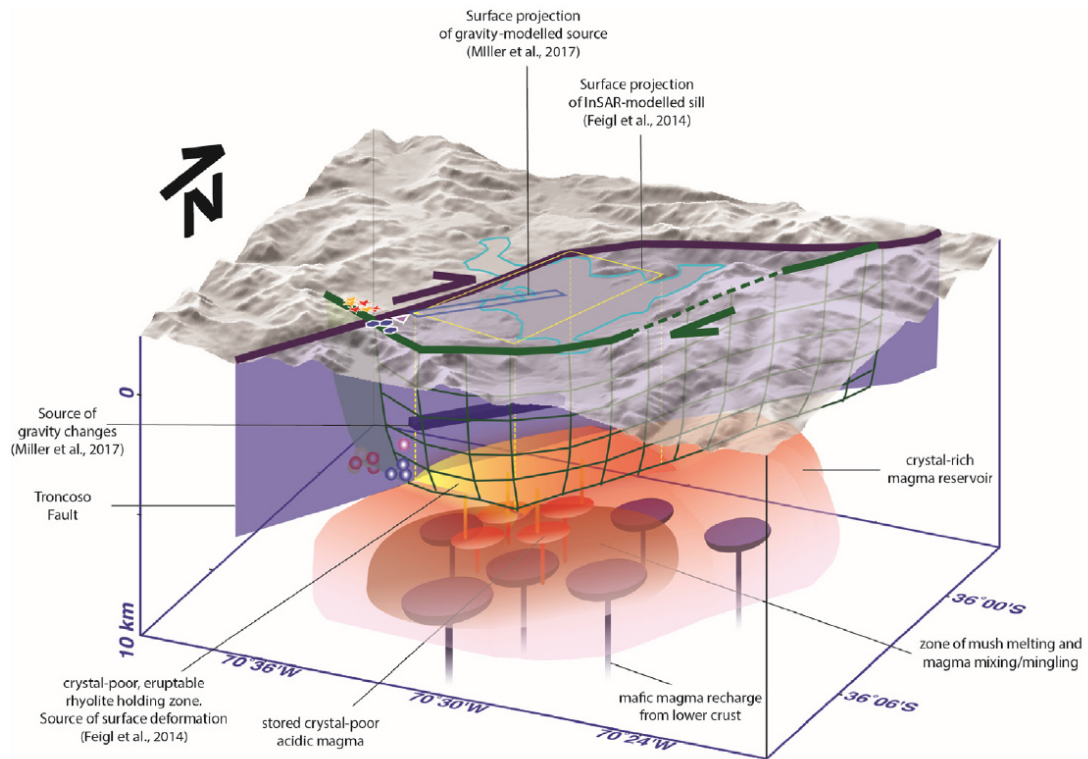


Figura 7. Modelo conceptual que relaciona la estructura cortical y el sistema magmático del CVLM como una cuenca de pull-apart dextral. El plano y líneas moradas corresponden a la falla Troncoso, en verde la falla Laguna Fea. Los círculos y estrellas sobre la superficie representan los epicentros de los enjambres sísmicos. Los círculos en subsuperficie representan los hipocentros de los sismos. Obtenido de Cardona et al. (2018).

CAPÍTULO 3

ORIGIN OF VOLCANIC-HOSTED MAGNETITE AT THE LAGUNA DEL MAULE COMPLEX, CHILE: A NEW EXAMPLE OF ANDEAN IRON OXIDE-APATITE MINERALIZATION?

Ernesto COFRÉ-ARZOLA¹, Martin REICH^{1,2}, José Tomás OVALLE^{1,2}, Gisella PALMA¹, Fernando BARRA^{1,2}, Artur DEDITIUS³, Adam C. SIMON⁴, Malcolm ROBERTS⁵

¹ Department of Geology and Millennium Nucleus for Metal Tracing Along Subduction, FCFM, Universidad de Chile, Santiago, Plaza Ercilla 803, Chile

² Andean Geothermal Center of Excellence (CEGA), FCFM, Universidad de Chile, Santiago, Plaza Ercilla 803, Chile

³ School of Engineering and Information Technology, Murdoch University, Murdoch, Australia.

⁴ Department of Earth and Environmental Sciences, University of Michigan, 1100 North University Ave., Ann Arbor, Michigan 48109-1005

⁵ Centre for Microscopy, Characterization and Analysis (CMCA), The University of Western Australia, Perth, WA 6009, Australia.

Corresponding author: ercofrea@gmail.com

3.1 ABSTRACT

Iron oxide-apatite (IOA) deposits, also known as magnetite-apatite or Kiruna-type deposits, are a major source of iron and potentially of rare-earth elements. To date, the youngest representative of this group corresponds to the Pleistocene (~2 Ma) El Laco deposit. El Laco is considered a unique type of IOA deposit due to its location in the Chilean Altiplano and volcanic-like features. Here we report the occurrence of a young (~1.0 Ma) IOA-type mineralization hosted within the Laguna del Maule Volcanic Complex in the south-central Andes, an unusually large and recent silicic volcanic system. We combined field observations and aerial drone images with detailed petrographic observations and electron microprobe analysis (EMPA) to characterize the magnetite mineralization— named here “Vetas del Maule”— hosted within andesites of La Zorra volcano. Five different styles of magnetite mineralization were identified: i) Massive magnetite, ii) Pyroxene-actinolite-magnetite veins,

iii) Hydrothermal breccias, iv) Disseminated magnetite, and v) Pyroxene-actinolite veins with minor magnetite. Electron microprobe analyses of the different types of magnetite reveal a consistent trend of decreasing [Ti+V], [Al+Mn] and Mg concentrations, from massive magnetite and pyroxene-actinolite-magnetite veins to pyroxene-actinolite veins. Mg-in-magnetite thermometry indicates a formation temperature ranging between ~950 and 500°C. Our data suggest that magnetite mineralization formed in a volcanic setting under conditions that evolved from magmatic-hydrothermal to purely hydrothermal. Ultimately, the Vetas del Maule provide evidence that volcanic-related IOA mineralization may be more common than previously thought, opening new opportunities of research and exploration for this ore deposit type in volcanic arcs.

3.2 INTRODUCTION

Iron oxide-apatite (IOA) deposits represent the Cu-poor end-member of the IOCG clan (Sillitoe, 2003; Barton, 2014). They are a major source of iron and potentially, rare-earth elements and other commodities such as phosphorus, thorium and cobalt. Iron oxide-apatite mineralization is dominated by magnetite, which can be accompanied by variable amounts (1–50% modal) of apatite, actinolite, pyroxene, epidote and Fe-(Cu) sulfides (Williams et al., 2005). IOA deposits occur globally with reported ages ranging from Proterozoic (Kiruna and Grängesberg districts, Sweden, and Pea Ridge and Pilot Knob, Missouri), Paleozoic (Bafq district, Iran), Cretaceous (Chilean Iron Belt), and Oligocene to Pleistocene (Cerro de Mercado, Mexico, and El Laco, Chile) (Nyström and Henríquez, 1994; Jonsson et al., 2013; Childress et al., 2016; Day et al., 2016; Heidarian et al., 2016; Westhues et al., 2017a,b; Simon et al., 2018; Corona-Esquivel et al., 2018; Ovalle et al., 2018; Peters et al., 2019).

The origin of IOA deposits remains controversial and several hypotheses have been proposed over the years to explain their formation. Liquid immiscibility models propose that massive magnetite ore bodies are formed by emplacement of hydrous Fe-Ca-P melts (Nyström and Henríquez, 1994; Naslund et al., 2002; Velasco et al., 2016; Tornos et al., 2016; Hou et al., 2018; Mungall et al., 2018; Bain et al., 2020, 2021). Magmatic flotation and metasomatic replacement models, on the other hand, involve magnetite precipitation from Fe-rich magmatic-hydrothermal fluids sourced from intermediate magmas (Hitzman et al., 1992; Rhodes and Oreskes, 1999; Sillitoe and Burrows, 2002; Barton and Johnson, 2004;

Barton, 2014; Dare et al., 2015; Knipping et al., 2015a,b; Westhues et al., 2017a,b; Simon et al., 2018). Regardless of the specific ore-forming mechanisms, all models invoke processes operating in a upper crustal environment, within a subduction- or back-arc-related tectonic setting at least for the Andean IOA deposits.

During the last decade, several studies have focused on IOA deposits located in the Chilean Iron Belt and the Andean Cordillera (Simon et al., 2018, and references therein). More recently, Palma et al. (2020) concluded that IOA deposits can be classified in sub-types based on their geological occurrence and mineralogical/geochemical features. IOA sub-types range from deep, high-temperature deposits (Los Colorados), to more transitional examples where hydrothermal signatures are dominant (e.g., El Romeral and Cerro Negro Norte). Pegmatitic-like, apatite-rich (>40% modal) systems such as the Carmen, Fresia and Mariela deposits, and the subvolcanic/aerial deposit of El Laco, would represent shallow examples of this deposit class (Ovalle et al., 2018; Palma et al., 2019, 2020, 2021; La Cruz et al., 2020; Childress et al., 2020). The youngest IOA deposit reported so far is El Laco (~2 Ma), located in the Altiplano-Puna region of the Chilean Andes. El Laco is apparently a unique case because of its volcanic features resembling magnetite “lava flows”, and due to its location within the Andean Cordillera (Nyström and Henríquez, 1994; Sillitoe and Burrows, 2002; Naranjo et al., 2010; Tornos et al., 2016; Velasco et al., 2016; Ovalle et al., 2018).

In this study, we report the occurrence of a ~1.0 Ma IOA-type mineralization — named here “Vetas del Maule” (*transl.* Veins of Maule)— hosted within the Laguna del Maule Volcanic Complex (LMVC) in the south-central Andes (35°59'S, 70°25'30"W) (Fig. 8). The LMVC comprises an area of 500 km² around a 15×20 km volcanic caldera, whose formation marks the beginning of volcanic activity around 1.5 Ma ago (Hildreth et al., 2010). Intense volcanism was registered since then, with an estimated of at least 50 eruptions and the formation of dozens of lava domes (Hildreth et al., 2010).

Magnetite is hosted within andesitic lavas of the La Zorra volcano, which has been dated at 1.013 ± 0.028 Ma (⁴⁰Ar/³⁹Ar plateau age, Hildreth et al., 2010). We aim to unravel the geological and physicochemical conditions of magnetite formation and provide further insights on the occurrence of IOA-type mineralization in the Andean metallogenic belt. To achieve this goal, we carried out field observations and aerial drone imaging, followed by a detailed petrographic characterization of the different magnetite occurrences using polarized

light microscopy and scanning electron microscopy (SEM). In addition, we performed electron microprobe analyses (EMPA) and constructed wavelength dispersive spectrometry (WDS) elemental maps of magnetite. Geochemical data were used to characterize each magnetite type and to constrain formation temperature by using the Mg-in-magnetite geothermometer (Canil and Lacourse, 2020). The new data is used to propose a genetic model for the Vetas del Maule magnetite mineralization.

3.3 GEOLOGICAL SETTING

3.3.1 The Laguna del Maule Volcanic Complex

The Laguna del Maule Volcanic Complex (LMVC) is located within the Transitional Southern Volcanic Zone (TSVZ) in south-central Chile (34°30'–37°S) (Fig. 8A). The geotectonic configuration is defined by a dextral-oblique convergence between the South American and Nazca plates, with a convergence rate of 7–9 cm/year that has been relatively constant during the last 20 Ma (Pardo-Casas and Molnar, 1987; Hildreth and Moorbath, 1988). The TSVZ is characterized by an average crustal thickness of ~35–40 km, reaching up to 40–50 km below the LMVC (Hildreth and Moorbath, 1988; Hildreth et al., 2010). Cenozoic rocks outcrop in most part of the western flank of the Andes Cordillera, corresponding mainly to volcano-sedimentary and volcanic rocks that cover Mesozoic marine and continental sedimentary rocks (Hildreth et al., 2010) (Fig. 8A).

The LMVC comprises the largest volume of postglacial rhyolites in the Andes (~40 km³) formed during recent explosive and effusive eruptions (Hildreth et al., 2010; Singer et al., 2014; Wespestad et al., 2019). The volcanic complex covers an area of approximately 500 km² with a 15 × 20 km volcanic caldera centered near the northern edge of the Laguna del Maule lake, and is considered one of the most hazardous active volcanic systems in the Southern Andean Volcanic Zone. Its eruptive activity began 1.5 Ma ago with the formation of the Bobadilla Caldera (Fig. 8A) and the last effusive eruption occurred about 2 ka ago. At least 50 eruptions have been documented, forming more than 36 rhyolitic and rhyodacitic domes (Hildreth et al., 2010; Singer et al., 2014, 2018).

Two main structures are recognized in the area: the Troncoso and the Laguna Fea faults (Fig. 8A). The dextral strike-slip, N45°E trending Troncoso fault extends for 30 km to the SW from the Laguna del Maule lake coinciding with a wide and deep valley known as

Cajón Troncoso (Fig. 8A). This fault probably extends to the NE in the Potrero Norte area (Cardona et al., 2018). The normal W-NW-trending Laguna Fea fault has been inferred through seismic studies and is postulated that intersects the Troncoso fault SW of the Laguna del Maule lake (Fig. 8A) (Cardona et al., 2018).

Based on detailed studies of post-glacial volcanic units of the last 25 ka, several authors have concluded that the eruptions derive from a silicic magma system (Andersen et al., 2013, 2017; Singer et al., 2014, 2018). Consequently, a “magmatic mush” model at depth has been proposed, in which the magmatic system comprises a relatively thin layer of solidified granitoid against the host rock, within which there is a rigid “mush” of crystals with minor interstitial melt (Singer et al., 2014). The mush remains partially molten as a result of the constant flow of heat and injections of mafic magma in the basal parts of the system.

The amalgamation of melt-rich lenses near the roof creates a low-density, crystal-poor, melt-dominated barrier zone that would block the rise of mafic magma to the surface. This barrier zone in turn constitutes a segregated and differentiated magmatic reservoir that can feed rhyolitic eruptions. As a result of lateral spreading, the magma body takes the shape of a flattened disc, which concentrates the structural stress and formation of dikes towards the edges (Singer et al., 2014). Variations in the local thickness of the barrier zone would favor the ascent of more differentiated lavas where it is thicker (south and east of the lake) or less differentiated where it is thinner (north and west of the lake) (Andersen et al., 2017).

Recent geophysical studies using high-precision global positioning systems (GPS) and synthetic aperture interferometric radar (InSAR) techniques have detected a significant volume change below the LMVC, corresponding to one of the largest vertical deformations registered in a volcanic complex (Fournier et al., 2010; Feigl et al., 2014; Le Mével et al., 2016; Singer et al., 2018; Novoa et al., 2019). This phenomenon has been interpreted as caused by inflation of a shallow magmatic sill or injection of hydrothermal fluids under the SW edge of the Laguna del Maule lake (Feigl et al., 2014; Le Mével et al., 2016). In addition, magnetotelluric studies have detected several conductive bodies at different depths, including magmatic bodies at 8 and 4–6 km depth and various discrete bodies interpreted as small hydrothermal reservoirs at 0.2–2 km depth (Cordell et al., 2018).

The Vetas del Maule are hosted within the La Zorra volcano (Hildreth et al., 2010; Figs. 8B; 9). This volcano is a severely eroded volcanic edifice composed of andesites with 58–62 wt.% SiO₂ and have been dated at 1.013 ± 0.028 Ma (⁴⁰Ar/³⁹Ar plateau age; Hildreth et al., 2010). Other adjacent volcanic units dated by using ⁴⁰Ar/³⁹Ar thermochronology range from ~0.95 to 0.47 Ma (Hildreth et al., 2010; Fig. 8B).

Previous authors have identified zones or patches of moderate to intense argillic alteration in the La Zorra andesites. The hydrothermal alteration is controlled by the inferred extension of the Troncoso fault and is represented by quartz-jarosite-kaolinite-smectite-pyrite subvertical N65°E veinlets and abundant clays (Hildreth et al., 2010; Rojas, 2019).

3.4 SAMPLES AND METHODS

Mapping and sampling were carried out during three field campaigns. Due to the steep topography of the study area (Fig. 9A), a drone was used to obtain images of the outcrops and build a digital elevation model of the La Zorra volcano (Fig. 9B). We used a DJI Mavic 2 Pro quadcopter, equipped with a 20 MP camera. The flight was open planned and operated using DroneDeploy. The software Agisoft Metashape Professional and ArcGIS arcScene were used to reconstruct the 3D digital elevation model (Fig. 9B). The drone was flown at a speed of 12 m/s, an elevation of 450–500 m, and images were obtained with a lateral and longitudinal overlap of 65%. The average size of the images was 5472 × 3648 pixels, and each image was automatically georeferenced with 3D coordinates from the drone GPS.

Surface samples were collected at altitudes between 2,400 and 2,850 m a.s.l. from outcrops on the SW, SE and NW slopes of La Zorra volcano (Fig. 9A). Nearly all samples are from the “inner” SE slope, where most of the mineralization —magnetite, actinolite and pyroxene breccias, veins and disseminated grains, —was found. Polished thin sections were prepared for polarized light microscopy, SEM inspection and EMPA analysis. Carbon coated polished thin sections were studied by using a FEI Quanta 250 SEM at the Andean Geothermal Center of Excellence (CEGA), Department of Geology, Universidad de Chile. The SEM was used to characterize textural relationships, zoning patterns, mineral inclusions, exsolutions and overgrowths, with an emphasis on magnetite. Backscattered-electron (BSE) images were obtained using an accelerating voltage of between 15 and 20 kV, a filament

current of 80 μA , a beam intensity of ~ 1 nA, a spot size of 5 μm , and a working distance of 10 mm.

Electron microprobe analysis (EMPA) of magnetite was carried out at the Centre of Microscopy, Characterisation and Analysis (CMCA) of the University of Western Australia. The instrument used was a JEOL JXA8530F Plus field-emission electron microprobe equipped with five tunable wavelength dispersive spectrometers (WDS). The accelerating voltage was 20 kV, and a focused beam (~ 1 μm) was set to avoid hitting inclusions and thin exsolution lamellae. Interference corrections were carried out for Ti concentrations because V $\text{K}\beta$ affects the Ti $\text{K}\alpha$ signal. The beam current was set to 40–50 nA. A counting time of 20 s was used for Fe, while higher counting times were used for the other elements: 30 s for Na, K, and 60 s for Si, Al, Mg, Ti, Ca, Fe, Cr, Ni, V, Mn, Zn, Cu. Background corrections for all elements were made by using the Mean Atomic Number (MAN) Method of Donovan and Tingle (1996). Additionally, quantitative wavelength-dispersive X-ray spectrometry (WDS) maps of Cr, Ca, Mn, Si, Na, Al, V, Ti, Mg were obtained on selected magnetite grains. Operating conditions were 40° take-off angle and a beam energy of 20 keV was used. The beam current was 50 nA and counting times were 20–60 ms/step. ZAF corrections were applied for all elements and interference corrections were performed for Fe $\text{K}\alpha$ and V $\text{K}\alpha$ because of Mn $\text{K}\beta$ and Ti $\text{K}\beta$ overlap, respectively. The standards used for both EMPA and WDS included natural and synthetic oxides and silicates (Appendix).

3.5 RESULTS

3.5.1 Magnetite mineralization styles

The IOA-type mineralization recognized at La Zorra volcano comprises magnetite, actinolite and pyroxene occurring in breccias, veins and as disseminated grains or aggregates. Overall, five mineralization styles were identified and are described below.

3.5.1.1 Massive magnetite

Decimeter to meter-scale, irregular, massive magnetite bodies occur near the top of La Zorra SE slope at an altitude of $\sim 2,730$ m a.s.l. (Figs. 9B; 10A). These bodies display sharp contacts with the andesitic host rock (Fig. 10B), and are composed of approximately 95% magnetite with minor amounts of ilmenite, rutile, clinopyroxene (augite),

orthopyroxene (hypersthene) and apatite. Phlogopite occurs at the margins of the magnetite body (Fig. 11A). Magnetite textures show: (i) thin ($\sim 0.5\text{--}2\ \mu\text{m}$) ilmenite oxy-exsolutions configuring a trellis texture (Fig. 12A), (ii) thin ($\sim 10\text{--}75\ \mu\text{m}$) alternating inclusion-rich and inclusion-poor bands (Fig. 12C), and (iii) irregular inclusion-rich zones (Fig. 12D). Disseminated magnetite aggregates are found occasionally within the andesite host rock, near the contacts with the bodies.

3.5.1.2 Pyroxene-actinolite-magnetite veins

Pale- to dark-green pyroxene-actinolite-magnetite veins were found in close spatial association with the massive magnetite bodies described above. The veins have thicknesses ranging from a few decimeters up to some meters, and run sinuously for about 30 m downward the slope, in some cases bifurcating and surrounding andesite blocks (Figs. 9D; 10C).

These veins are formed by an intergrowth of large ($\sim 500\ \mu\text{m}$) crystals of orthopyroxene (hypersthene), clinopyroxene (augite), actinolite and magnetite with minor apatite, ilmenite and chlorite (Figs. 10D, 11B). Pyroxene is more abundant than actinolite, and is observed with relatively fresh cores and often altered rims to irregular fibrous masses of a Mg-Fe-Si-O phase, probably cummingtonite. Magnetite textures are similar to those described for the massive magnetite bodies, including thin and thick ilmenite lamellae. Thin alternating bands of microinclusions and irregular inclusion-rich zones are also recognized (Fig. 12A-D). Some magnetite grains display late magnetite overgrowths (Fig. 12E).

3.5.1.3 Pyroxene-actinolite veins

Three pyroxene-actinolite veins were observed along the inner SE slope of the La Zorra volcano (Fig. 9B). All three have an approximate NNW orientation. The first vein is located at $\sim 2,400\ \text{m a.s.l.}$, near the base of the SE slope, and is approximately half a meter thick and $\sim 15\ \text{m}$ long (Figs. 9B; 10E). The second is a $\sim 2\ \text{m} \times 6\ \text{m}$ remnant of a larger NNW trending vein found at $\sim 2,600\ \text{m a.s.l.}$, and located at the middle of the inner SE slope (Figs. 9B, C, and 10F). The third is a small, 1 m thick vein, a couple meters long at about the same altitude than the previous vein (Fig. 9B, C). All three veins display a sharp contact with the andesitic host rock.

Pyroxene-actinolite veins contain euhedral to subhedral crystals of orthopyroxene (hypersthene), clinopyroxene (augite) and actinolite (Figs. 10E, F; 11C). Minor pyrite, quartz, apatite, calcite, titanite, ilmenite and magnetite were also observed, as well as a few grains of zircon and thorite. Pyroxene and actinolite display variable degrees of chloritization. Titanite grains are common, and present ilmenite or rutile relicts in their interior showing replacement textures (Fig. 11D). There is almost no magnetite in the samples and when present it appears as pristine, anhedral grains or occasionally with a porous textures at the grain edge.

3.5.1.4 Hydrothermal breccias

Two outcrops of hydrothermal breccias were identified; one at an altitude of 2,800 m a.s.l. (~80 m to the east of the massive magnetite outcrop on the inner SE slope), and the second at a lower altitude (~2450 m a.s.l.) (Fig. 9B; 10G). The breccias occur as irregular decimeter to decameter masses and are composed of angular and rounded clasts of albitized andesite, immersed in a fine-grained dark green matrix consisting of pyroxene, actinolite, chlorite, apatite, magnetite and minor ilmenite and pyrite (Fig. 11E, F). Magnetite in the breccia matrix show different forms of ilmenite lamellae in anhedral grains. Also, thin banded textures as well as porous magnetite were observed (Fig. 12A-C, F).

3.5.1.5 Disseminated magnetite

Tens of micrometers to cm-sized disseminated magnetite grains are observed in the host rock adjacent or close to the magnetite mineralization, especially abundant near to hydrothermal breccias (Fig. 10H, I). In most cases they correspond to anhedral magnetite grains dispersed within albitized andesite (Fig. 11G, H), although often they occur as euhedral magnetite crystals that are filling vesicles (Fig. 10H). In some cases, the disseminated magnetite is closely related to thin (tens of micrometers to cm thick) veinlets of magnetite (Fig. 10I). Magnetite grains show thin and thick ilmenite oxy-exsolution lamellae, and often porosity restricted to rims (Fig. 12A, B, F).

Figure 13 summarizes the mineralogy of the different mineralization styles and main magnetite textures.

3.5.2 Magnetite geochemistry

3.5.2.1 EMPA analyses

All EMPA analyses and a statistical summary of the data are reported in Appendix. Most trace elements in magnetite including Si, Na, Al, V, Ti, Mg, Ca, K, Mn exhibit variable concentrations ranging between <100 ppm, i.e., the average detection limit of the EMPA, up to a few wt%. Ni, Cr, Cu and Zn are rarely detected (Appendix).

The compositional variability of each magnetite can be represented in magnetite discriminant diagrams (Fig 14A, B). EMPA data of each magnetite type was plotted in the [Ti+V] vs. [Al+Mn] diagram (Fig. 14A). The five different mineralization styles configure a general trend of decreasing [Ti+V] and [Al+Mn] concentration forming distinct clusters. Magnetite in the pyroxene-actinolite-magnetite veins and the massive magnetite bodies show the highest concentrations of [Ti+V] and [Al+Mn], plotting in the “porphyry” field, with some data points plotting within the “Fe-Ti, V” field. Hydrothermal breccias and disseminated magnetite also plot within the “porphyry” field, with relatively lower [Ti+V] and [Al+Mn] concentrations. Pyroxene-actinolite veins, on the other hand, deviate from this trend and show distinctly lower concentrations of [Ti+V] and [Al+Mn] plotting below the “Kiruna” field. In addition, a group of points from the massive magnetite bodies plot in the “porphyry”, “IOCG” and “Kiruna” fields.

The EMPA data were also plotted in the Fe vs (V/Ti) with most points falling within the hydrothermal magnetite field and Fe concentrations between ~66 and 72 wt% (Fig. 14B). Overall, a general trend of decreasing V/Ti ratios and slight increase in Fe are observed for some mineralization styles forming distinct clusters. For example, the pyroxene-actinolite-magnetite, pyroxene-actinolite veins, and massive magnetite bodies show the highest V/Ti ratios (0.7–10), followed by disseminated magnetite with intermediate V/Ti ratios (0.3–3) and hydrothermal breccias with relatively lower V/Ti ratios (<0.5). Only a few sparse data points from all styles—except for pyroxene-actinolite veins—plot in the magmatic magnetite field.

3.6 DISCUSSION

3.6.1 *A magmatic-hydrothermal origin of magnetite*

The different styles of magnetite mineralization identified at Vetas del Maule share similar compositional and textural features with Kiruna-type iron oxide-apatite deposits worldwide, especially those in the Coastal Cordillera of northern Chile and the Pleistocene El Laco deposit in the Chilean Altiplano. These deposits display similar mineralization styles including massive magnetite bodies, hydrothermal breccias and veins, as well as disseminations in permeable volcano-sedimentary host rocks (Sillitoe, 2003; Williams et al., 2005; Barton 2014; Simon et al., 2018; Palma et al., 2020, and references therein).

Magnetite is the main constituent of IOA deposits and therefore, its trace element geochemistry has been extensively investigated in diverse mineralized systems, including Fe-Ti, V (nelsonite), porphyry, skarn, IOCG and BIF deposits (Dupuis and Beaudoin 2011; Nadoll et al., 2014; Knipping et al., 2015b; Wen et al., 2017; Palma et al., 2020). Those studies have used the concentration of key elements such as Fe, Ca, Al, Mn, Mg, Ga, Ti and V, to construct discrimination diagrams and evaluate geochemical trends to estimate the magnetite formation temperature.

The Vetas del Maule magnetite data plotted in the [Ti+V] vs. [Al+Mn] diagram configure a conspicuous trend of decreasing concentrations from pyroxene-actinolite-magnetite veins, massive magnetite, disseminated magnetite and hydrothermal breccias, to pyroxene-actinolite veins (Fig. 14A). Similar elemental variations have been reported and interpreted as being the result of cooling from high-temperature magmatic-hydrothermal conditions (1000–600°C) to lower-temperature, hydrothermal conditions (<600°C) (Nadoll et al., 2014; Knipping et al., 2015b; Ovalle et al., 2018; Rojas et al., 2018; Salazar et al., 2020; Palma et al., 2020, 2021). This suggests that the different magnetite types formed at different temperatures. In Figure 14B, most of the magnetite data plot in the hydrothermal field and show a marked decrease in V/Ti ratios. The V/Ti ratio decreases following a general trend from massive magnetite, pyroxene-actinolite-magnetite veins, disseminated magnetite, and hydrothermal breccias, similar to the trend observed in the [Ti+V] vs. [Al+Mn] diagram. We note that a few samples of each mineralization style plot in the magmatic (igneous) field, progressively increasing the number of samples towards higher V/Ti and Fe concentrations within the style, except for pyroxene-actinolite veins. We argue that this could be indicative

of reequilibration via fluid-mediated dissolution-precipitation processes affecting magnetite (Wen et al., 2017; Huang and Beaudoin 2019; Palma et al., 2020). Regardless, nearly all magnetite analyses plot within the hydrothermal field, strongly supporting that magnetite formed from a high-temperature hydrothermal fluid (Fig. 14B).

3.6.2 Magnetite crystallization temperatures

In order to constrain the formation temperature of each mineralization style, we used the empirical Mg-in-magnetite geothermometer recently proposed by Canil and Lacourse (2020), which is based on the change in X_{Mg} of magnetite with temperature caused by exchange reactions in spinel solid solutions. Thermometric calculations in single grains were performed using the following calculation:

$T_{Mg-Mag} (^{\circ}C) = -8344(\pm 320)/[\ln X_{Mg} - 4.1 (\pm 0.28)] - 273$, in which $X_{Mg} = Mg/(Mg + Fe_{total})$, and considering an uncertainty of ± 50 $^{\circ}C$.

The calculated temperatures for magnetite are restricted between ~ 950 and $\sim 500^{\circ}C$ (Fig. 15). The highest temperatures are recorded in the massive magnetite ($950\text{--}750^{\circ}C$, average $830^{\circ}C$, $N=524$), closely followed by pyroxene-actinolite-magnetite veins ($900\text{--}750^{\circ}C$, average $806^{\circ}C$, $N=210$), hydrothermal breccias ($800\text{--}550^{\circ}C$, average $649^{\circ}C$, $N=247$, which also shows the widest range of temperature), disseminated magnetite ($650\text{--}525^{\circ}C$, average $576^{\circ}C$, $N=89$), and pyroxene-actinolite veins ($600\text{--}525$ $^{\circ}C$, average $575^{\circ}C$, $N=30$). Even though there is some overlap between mineralization styles, a distinct difference in temperature between the various mineralization styles is observed with a well-defined cooling trend from $\sim 950^{\circ}C$ to $\sim 500^{\circ}C$ (Fig. 15).

High temperatures registered in magnetite from Vetás del Maule are similar to those obtained in other IOA type deposits with several characteristics in common. Recently, Palma et al. (2021) compiled a large geochemical dataset and calculated the magnetite formation temperature for several IOA deposits of the Chilean Iron Belt, e.g., Fresia, Carmen, Mariela, Cerro Negro Norte, El Romeral and Los Colorados, and El Laco. Those authors found that magnetite crystallized over a wide temperature range for the Chilean Iron Belt (i.e., $\sim 850\text{--}320$ $^{\circ}C$) and El Laco ($\sim 950\text{--}400^{\circ}C$). The temperature range determined here for Vetás del Maule ($\sim 950\text{--}500^{\circ}C$) is highly consistent with reported temperatures for El Laco although

the latter has slightly lower minimum temperatures, possibly related to low-temperature oxidation and replacement by maghemite, hematite and goethite typically found at shallow levels at El Laco (Ovalle et al., 2018; Palma et al., 2021), whereas in Vetas del Maule low temperature magnetite might be associated with dissolution-reprecipitation and re-equilibration processes.

3.6.3 Magnetite microtextures and re-equilibration

Magnetite from Vetas del Maule displays complex microtextural features, similar to those described in several magnetite-bearing ore deposits worldwide (e.g., Knipping et al., 2015a; Wen et al., 2017; Deditius et al., 2018; Ovalle et al., 2018; Simon et al., 2018; Rojas et al., 2018; Huang and Beaudoin 2019; Salazar et al., 2020; Palma et al., 2020). Textures can provide valuable information to better understand the geochemical trends described for each magnetite type, and its relation to temperature and fO_2 fluctuations. In order to evaluate the effect of magnetite microtextures on the behavior of minor/trace elements, we performed quantitative WDS maps on representative magnetite grains (Fig. 16).

Magnetite contains both ilmenite oxy-exsolutions as well as variable amounts of ilmenite grains (Fig. 13). Typically, accessory magnetite with trellis-like ilmenite exsolutions and ilmenite grains have been described in igneous rocks, in magmatic Fe-Ti, V, Ni-Cu sulfide deposits (Buddington and Lindsley, 1964; Boutroy et al., 2014; Tan et al., 2016) and in a number of magmatic-hydrothermal ore systems, including Fe skarns (Hu et al., 2015; Wen et al., 2017), volcanic-hosted Fe-Cu (Wang et al., 2020), IOCG (Huang and Beaudoin 2019; Rodriguez-Mustafa et al., 2020), and IOA deposits (Borrok et al., 1998; Parente et al., 2019; Ovalle et al., 2018; Palma et al., 2020).

The presence of two or more types of ilmenite exsolutions coexisting within the same magnetite grain in nearly all mineralization styles indicate a complex evolution (Fig 12B, G). Similar coexistence of various ilmenite exsolution types (e.g., thin oxy-exsolution trellis and thick irregular exsolutions) has been studied in magmatic Fe-Ti oxide-bearing intrusions, and interpreted as product of different subsolidus exsolution mechanisms—including oxy-exsolution of ilmenite and inter-oxide re-equilibration—indicating multiple stages of ilmenite formation under fluctuating temperature and fO_2 conditions (Tan et al., 2016).

At Vetas del Maule, the most widespread thin ilmenite exsolutions in trellis would be consistent with an oxy-exsolution formation mechanism, while the occurrence of ilmenite grains adjacent to magnetite could indicate the action inter-oxide re-equilibration as formation mechanisms for the thicker lamellae, similar to that proposed for the lenticular-lamellae described in Tan et al. (2016). In this regard, WDS maps reveal that Ti displays a particularly complex distribution at the grain scale, most likely reflecting multiple superimposed formation processes (Fig. 16A).

Banded textures are also common and provide further insights on magnetite formation conditions. Textures with fine bands (Fig. 12C) show “dark”, micro- to nano-sized microinclusion-rich bands that are depleted in Fe (1–3 wt%; Fig. 16F), but enriched in Mg, Si (0.1–5 wt%; Fig. 16E, G), Al, Na and Ca (0.1–1 wt%; Fig. 16C, H) with respect to “light”, microinclusion-poor bands. It is also possible to observe magnetite with coarser (up to tens of μm) inclusion-rich irregular zones (Fig. 12D), depleted in Si, Ca, Al, Mg, Mn and Ti with concentrations of trace elements similar to magnetite of the “light”, microinclusion-poor bands.

Regular bands of microinclusions have been reported in other IOA deposits (e.g., Los Colorados, Carmen, Fresia, and El Laco) and are attributed to magnetite that crystallizes from magmatic-hydrothermal fluids (Knipping et al., 2015b; Deditius et al., 2018; Ovalle et al., 2018; Yin et al., 2019; Palma et al., 2020). It has been suggested that this texture originates from fluctuating supersaturation of mineralizing fluids with respect to oxide and silicate phases that can trigger the formation of mineral micro- to nanoparticles bands during progressive growth of the hydrothermal magnetite surface (Deditius et al., 2018; Huang and Beaudoin, 2021).

Notably, in three mineralization styles in which the presence of regular bands of microinclusions was observed they were both alone or coexisting with superimposed ilmenite lamellae within the same magnetite grain (Figs. 12B,G; 16). This could be interpreted as textural evidence that the magmatic-hydrothermal fluids responsible for the oscillatory bands of microinclusions texture were sufficiently enriched in Ti to precipitate titano-magnetite that subsequently exsolved ilmenite lamellae (Tan et al., 2016).

Overgrowth and porous textures in magnetite are also common at Vetas del Maule (Fig. 12E, F). These features are similar to those observed in other IOA deposits and

interpreted as result of dissolution-reprecipitation processes (Putnis 2009; Ovalle et al., 2018; Huang and Beaudoin 2019; Palma et al., 2020). In turn, several authors have related dissolution-reprecipitation textures to new injections of hydrothermal fluids that react with previously precipitated minerals (Putnis, 2009; 2015; Huang and Beaudoin, 2019).

Overall, the magnetite microtextures observed here are indicative of a fluid-dominated system that cooled over a wide temperature range (~950–500°C) as determined by magnetite thermometry, probably punctuated by multiple hydrothermal pulses of fluctuating fO_2 conditions.

3.6.4 Genetic model

The magnetite features identified here are remarkably similar to those described for the subvolcanic/aerial-type IOA deposit of El Laco in the Chilean Altiplano. The chemical composition of magnetite from El Laco and other IOA deposits within the Chilean Iron Belt, has been interpreted to reflect a transition from high-temperature igneous conditions (~1000–800°C) at depth to lower-temperature magmatic-hydrothermal conditions (>600°C) at shallow levels (Ovalle et al., 2018; Rojas et al., 2018; Salazar et al., 2020; La Cruz et al., 2020, Palma et al., 2020, 2021). Regardless of the primary igneous processes that concentrated Fe in the source magma, i.e., magnetite flotation (Knipping et al., 2015a), Fe-Ca-P liquid immiscibility (Hou et al., 2018) or carbonate-sulfate melts (Bain et al., 2020), geochemical evidence unequivocally point to magmatic and late-stage magmatic-hydrothermal fluids as responsible of the magnetite mineralization in those deposits (Troll et al., 2019; Palma et al., 2020).

Mg-in-magnetite geothermometry show a cooling trend from ~950 to 500°C similar to that observed in other IOA deposits (Fig. 15). The massive magnetite and pyroxene-actinolite-magnetite veins cluster at high temperatures (~950–750°C), while hydrothermal breccias, disseminated magnetite, and pyroxene-actinolite veins are related to progressively lower temperatures (~750–500°C). Based on our data, we propose that the formation of the Vetas del Maule IOA-type mineralization was the result of a sequence of processes during the evolution of La Zorra volcano (Fig. 17).

The first stage occurred under high temperature (~950–600°C), typical of high temperature magmatic-hydrothermal conditions. Massive magnetite, pyroxene-actinolite-

magnetite veins, hydrothermal breccias and disseminated magnetite were most likely formed from magmatic-hydrothermal fluids injected into faults of the volcanic edifice (Fig. 17A). The massive magnetite bodies and pyroxene-actinolite-magnetite veins show a similar trace element signature with compositions plotting in fields related to near-igneous temperature conditions (Fig. 14; Dupuis and Beaudoin, 2011; Nadoll et al., 2014; Wen et al., 2017). These two mineralization styles also record the highest average temperatures (mean values of 830°C and 806°C, respectively; Fig. 15), and are found in close spatial association (Figs. 9D; 10C). We therefore conclude that massive magnetite bodies and pyroxene-actinolite-magnetite veins were formed under near-igneous conditions. There are some mineralogical indications that massive magnetite precedes formation of pyroxene-actinolite-magnetite veins as evidenced by the scarce presence of actinolite and abundant pyroxene inclusions in the massive magnetite (Fig. 13), pointing to conditions above the stability field of actinolite, i.e., $\geq 780^\circ\text{C}$ at 1 kbar (Lledo and Jenkins, 2008), and in agreement with our thermometric estimations (Fig. 15). In addition, various pyroxene grains in the pyroxene-actinolite-magnetite veins have rims and fractures altered to irregular fibrous masses of a Mg-Fe-Si-O phase, probably cummingtonite ($\text{Mg}_7(\text{Si}_8\text{O}_{22})(\text{OH})_2$). Experimental studies on the upper thermal limit for Mg-rich actinolite by Lledo and Jenkins (2008) propose the change from [Opx, Cpx, Qz and H_2O] towards [actinolite] below 780°C at 1 kbar and towards [actinolite + cummingtonite] below 700°C at 1 kbar. In the cited experiments, cummingtonite tends to occur forming similar reaction rims. This Mg-Fe-Si-O phase is associated with magnetite overgrowths and porosity (Fig. 12E, H), which could suggest dissolution-reprecipitation processes caused by lower temperature fluids.

The formation of hydrothermal breccias and disseminated magnetite occurred at lower temperatures, as evidenced by magnetite thermometry, i.e., $\sim 750\text{--}500^\circ\text{C}$ with averages of 649°C and 576°C , respectively (Fig. 15), and may reflect a significant change in hydrostatic conditions within the volcanic edifice. Magnetite breccias have been described in other IOA deposits, and interpreted as formed by hydraulic injection of hydrothermal fluids under rapid decompression rates (Palma et al., 2020). In IOA deposits from the Chilean Iron Belt, fluid-filled open fractures and breccias suggest that magnetite precipitation was triggered by significant pressure drop at shallow crustal levels through suction-pump mechanisms (Sibson et al., 1975; Sibson, 2001; Cox et al., 2001; Olivares et al., 2010).

Further, abrupt pressure changes significantly decrease the solubility of FeCl_2 complexes in the fluid, increasing the efficiency of magnetite precipitation (Simon et al., 2004; Rojas et al., 2018). At El Laco, hydrothermal breccias bodies were ubiquitously observed in drill core samples and were interpreted as formed during the collapse of the volcanic edifice (Ovalle et al., 2018). Thus, it is likely that the hydrothermal breccias at Vetas del Maule are the product of a similar process, i.e., hydraulic injection of hydrothermal fluids with subsequent fracturing and rapid decompression rates or violent decompression due to collapse of the La Zorra volcano. Geophysical surveys have imaged active hydrothermal systems under large arc stratovolcanoes such as Fuji (Japan), Llaima and Osorno (Chile) at relatively shallow levels (~ 1 km) (Romero et al., 2021 and references therein), indicating the possible presence of hydrothermally altered cores inside them. These cores may deform under gravitational deformation and may trigger surface landslides before, during and after main failure events (Cecchi et al., 2004; Romero et al., 2021). At the Laguna del Maule Volcanic Complex, magnetotelluric studies have identified discrete zones between 200 m and 2 km interpreted as small hydrothermal reservoirs (Cordell et al., 2018). Thus, and even though a collapse of the volcanic edifice hypothesis remains to be tested with additional field and geological studies, this appears as one plausible process to explain the formation of the magnetite mineralization at LMVC.

Conversely, the pyroxene-actinolite veins probably formed during a late-stage characterized by spent hydrothermal fluids of relatively lower temperature ($\sim 600\text{--}525^\circ\text{C}$, average 575°C) that infiltrated other fractures and open spaces (Fig. 17B). Pyroxene-actinolite veins have some distinct characteristics when compared to the other mineralization styles. For example, they appear as isolated veins far from the other mineralization styles, and at a lower altitude within the volcanic slope, in some cases hundreds of meters below the other types (Fig. 9B). Also, no disseminated magnetite was found in their vicinity. This mineralization style also presents higher amounts of actinolite exceeding pyroxene, and titanite is especially abundant in large aggregates associated with minor pyrite and chalcopyrite (Fig. 11D), and most important, almost no magnetite. When present, magnetite is trace element poor and appears homogeneous or with porous rims. Particularly, the predominance of titanite over ilmenite at a temperature range of $\sim 600\text{--}525^\circ\text{C}$, point to a substantial increase in $f\text{O}_2$ (Xirouchakis et al., 2001a,b; Kohn, 2017). Previous studies have

documented that hydrothermal magnetite formed at low temperatures (<600°C) has lower concentrations of trace elements and higher Fe contents due to reequilibration associated with dissolution-precipitation processes (Wen et al., 2017; Ovalle et al., 2018; Huang and Beaudoin, 2019). These processes could also explain the deviation from common compositional trends observed in some magnetite grains in this study (Fig. 14). All these characteristics indicate abrupt changes in physicochemical conditions, and formation under lower temperatures and higher fO_2 , probably in the waning stages of the hydrothermal system.

Finally, recent intense glacial erosion and consequent isostatic rebound during retreat, would have exposed these magnetite bodies (Fig. 17C).

3.7 CONCLUSIONS

This study documents a new occurrence of IOA-type mineralization hosted within andesites of the eroded La Zorra volcano (~1.0 Ma) in the Laguna del Maule Volcanic Complex, south-central Andes. Based on field observations and petrographic characterization we identified five different mineralization types: i) irregular bodies of massive magnetite, ii) pyroxene-actinolite-magnetite veins, (iii) hydrothermal breccias, (iv) disseminated magnetite, and (v) pyroxene-actinolite veins with minor magnetite. A wide diversity of magnetite microtextures were identified, including trellis-like oxy-exsolutions, regular bands of microinclusions, overgrowths and porous textures, many of which have been described in several IOA deposits worldwide.

Electron microprobe analyses of magnetite show a trend of decreasing [Ti+V] and [Al+Mn] concentrations from massive magnetite and pyroxene-actinolite-magnetite veins to pyroxene-actinolite veins. Mg-in-magnetite thermometry indicate a temperature range of formation between ~950°–500°C, broadly consistent with the progressive decrease in [Ti+V] and [Al+Mn] concentration of magnetite through the mineralization styles. Our data suggest that magnetite at Vetás del Maule formed under magmatic-hydrothermal to purely hydrothermal conditions.

The geological and chemical characteristics of magnetite mineralization in Vetás del Maule are remarkably similar to those described in subvolcanic/aerial-type IOA deposits (Palma et al., 2020), particularly El Laco in the Altiplano of northern Chile. Therefore, we

conclude that the IOA-type mineralization reported in this study was the result of ore-forming processes that efficiently concentrated iron, probably hydraulic injection of hydrothermal fluids with subsequent fracturing and decompression or even during the collapse of an erupting volcanic system.

Ultimately, Vetás del Maule provides evidence that IOA-type mineralization may be more common than previously thought in modern volcanic arcs, providing new opportunities for research and exploration.

3.8 Figures

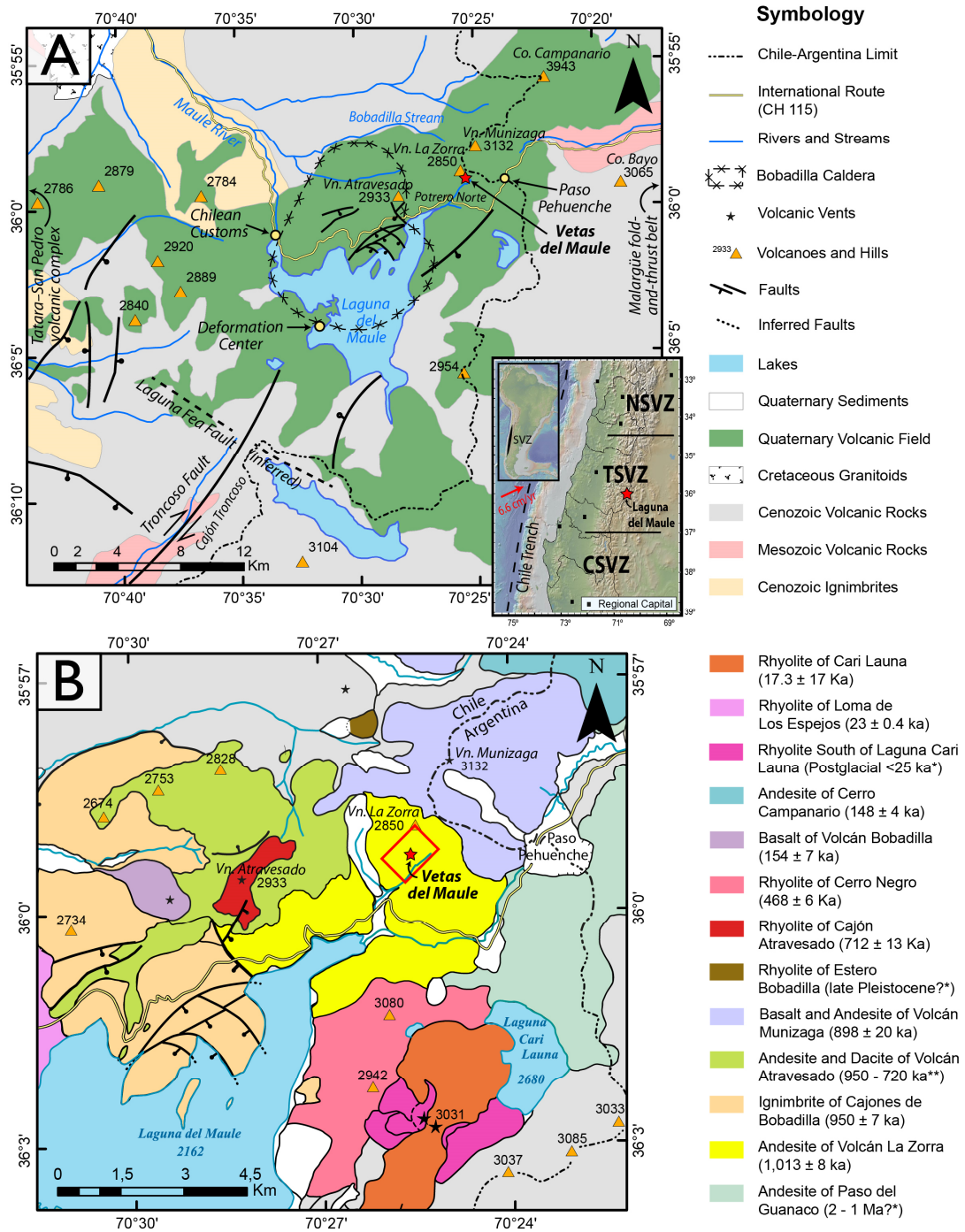


Figure 8. (A) Location and geological map of the LMVC. SVZ: Southern Volcanic Zone; NSVZ: Northern SVZ; TSVZ: Transitional SVZ; CSVZ: Central SVZ. (B) Main volcanic units of the NE area of the LMVC. Modified from Muñoz and Niemeyer (1984), Hildreth et al. (2010), Feigl et al. (2014) and Cardona et al. (2018). $^{40}\text{Ar}/^{39}\text{Ar}$ ages are from Hildreth et al. (2010). (*) Stratigraphic age. (**) K/Ar age.

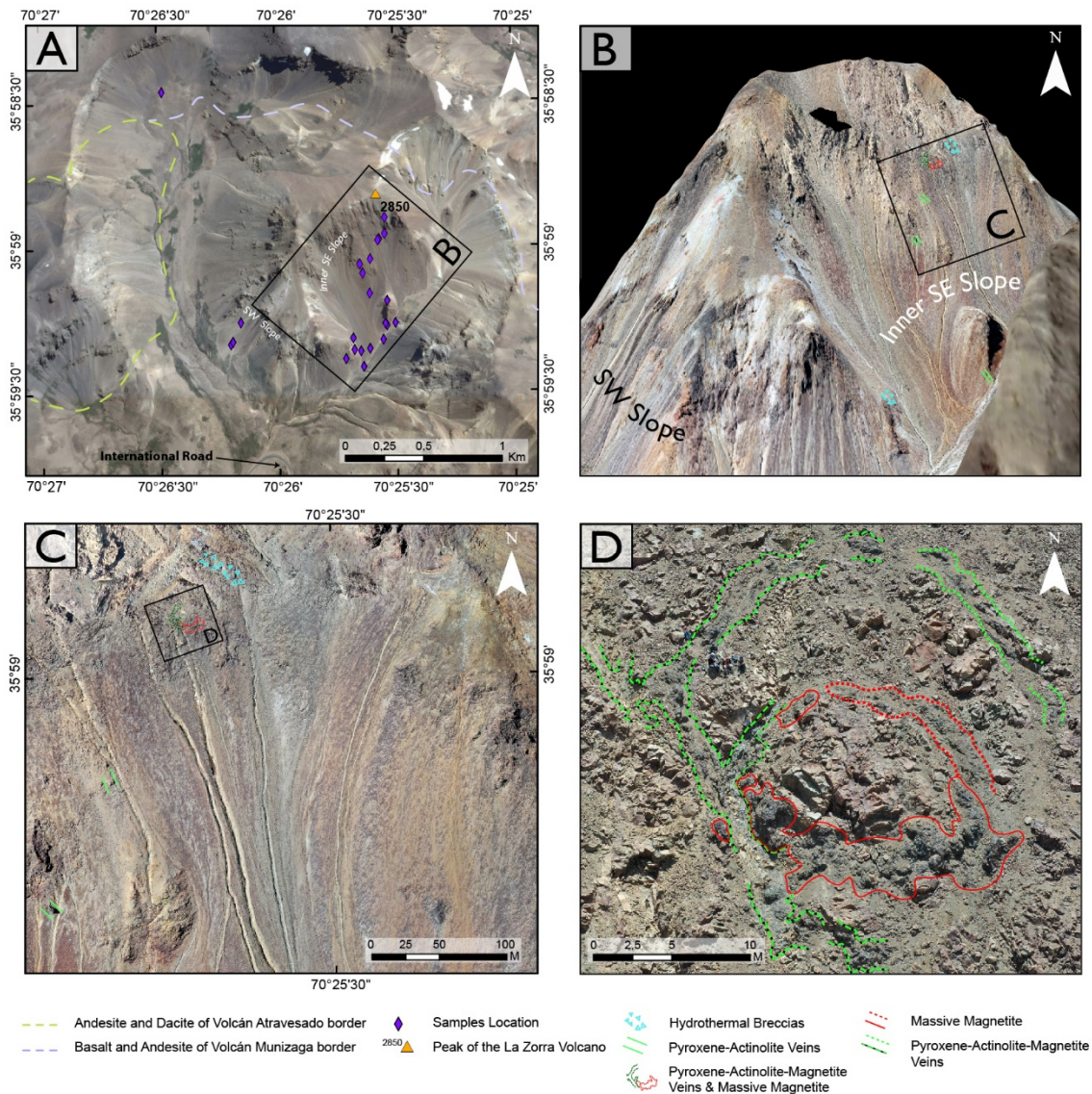


Figure 9. Location of the IOA-type mineralization within La Zorra volcano. (A) Satellite image of La Zorra volcano dissected by a steep alluvial valley and covered by nearby volcanic units. (B) Drone aerial image of the volcano showing the spatial relationship between the different mineralization styles. The vertical axis is exaggerated. (C) Aerial image of the easternmost section of the “inner” SE slope. (D) Drone image of the massive magnetite and pyroxene-actinolite-magnetite veins showing their close spatial relation.

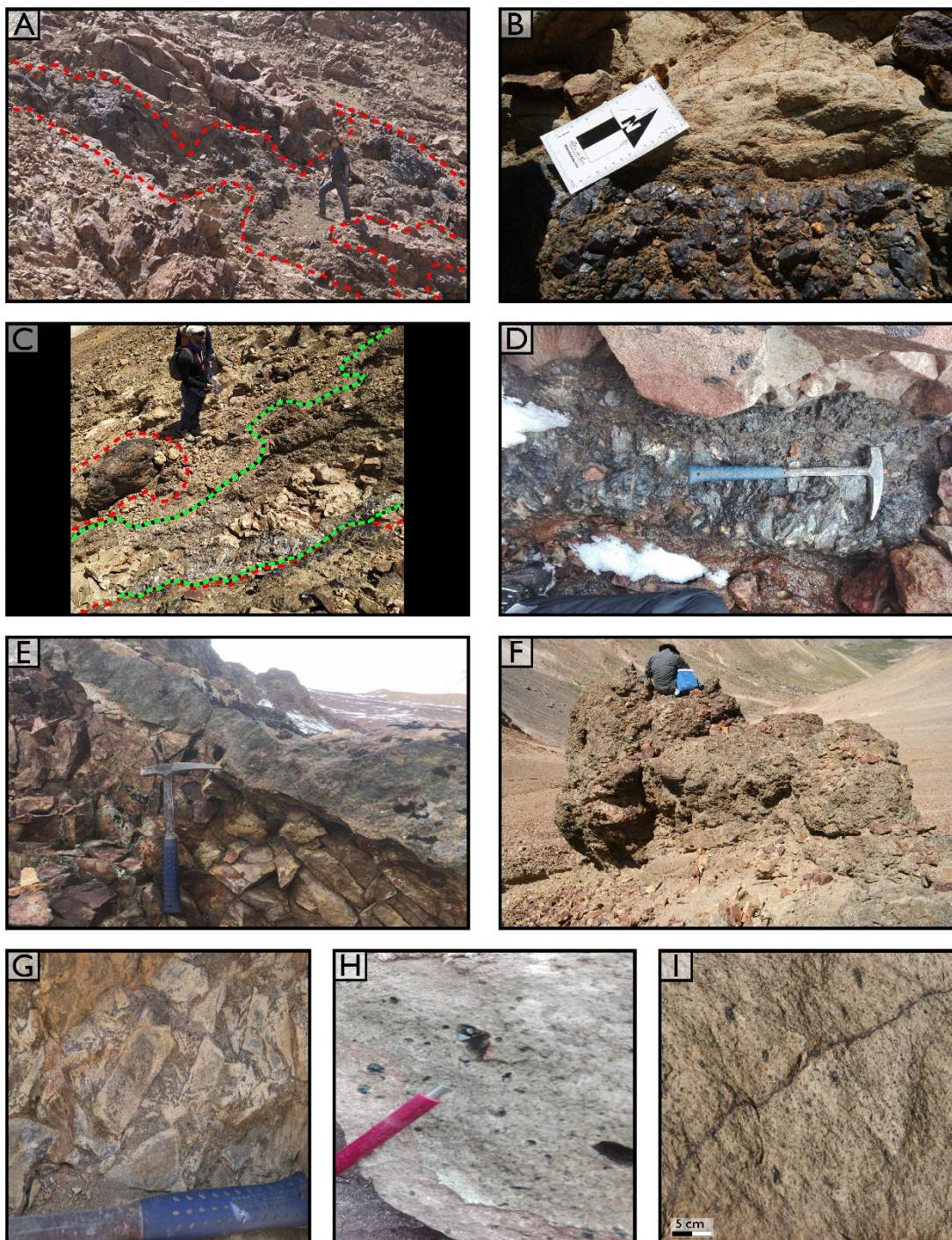


Figure 10. Field photographs showing the IOA-type mineralization styles. (A) Massive magnetite outcrop (red dashed line). (B) Sharp contact between massive magnetite and andesite host rock. (C) Massive magnetite (red dashed line) and pyroxene-actinolite-magnetite veins (black and green dashed line). (D) Thick pyroxene-actinolite-magnetite vein in andesite. (E) Pyroxene-actinolite vein located at the base of the SE slope. (F) Massive outcrop of pyroxene-actinolite. (G) Easternmost outcrop of hydrothermal breccias. (H) Disseminate magnetite within the andesite host rock. (I) Thin magnetite veinlets.

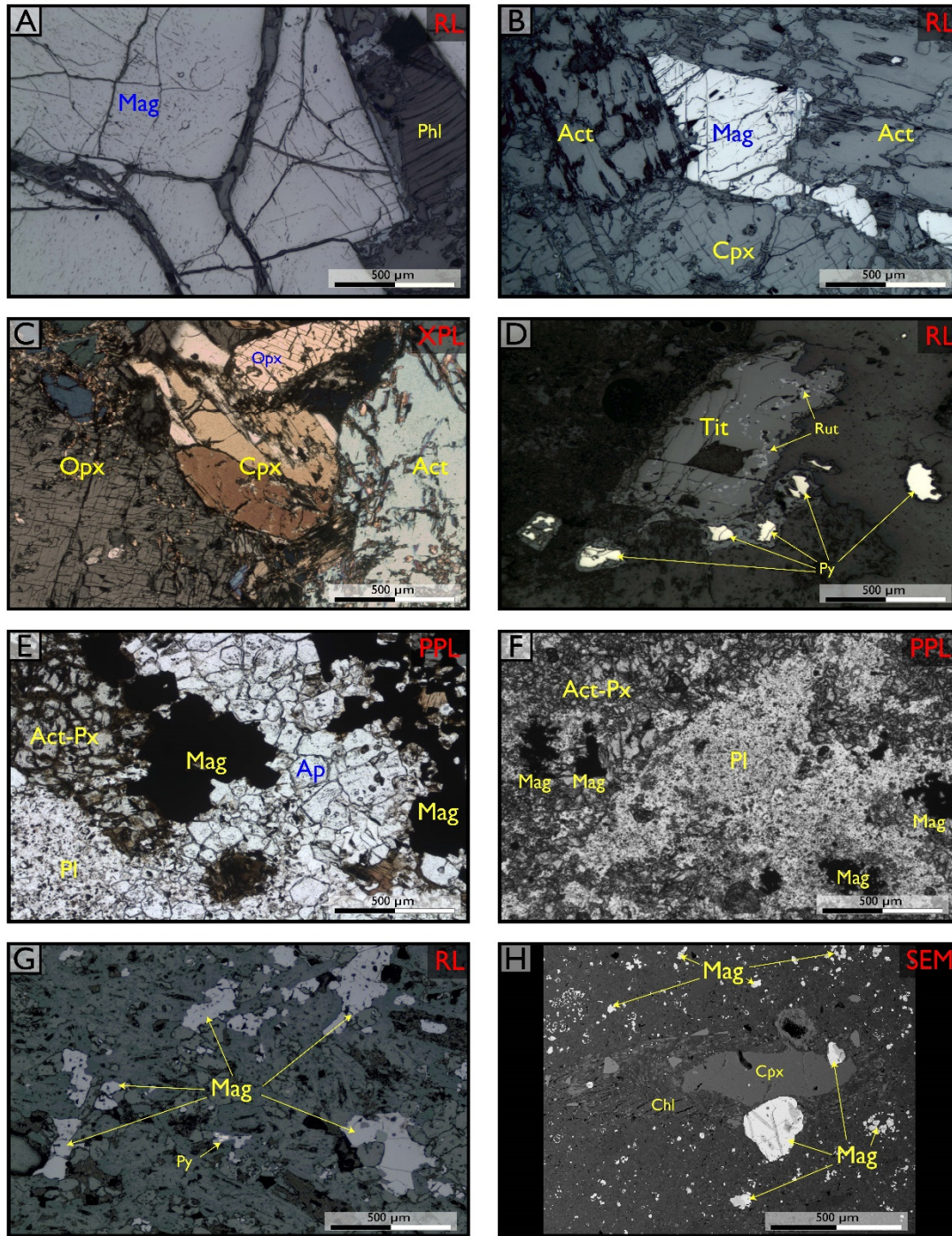


Figure 11. Photomicrographs of Vetas del Maule IOA-type mineralization. (A) Large magnetite crystal in contact with phlogopite. Massive magnetite sample MLZ-04-B. (B) Pyroxene, actinolite and magnetite assemblage. Pyroxene-actinolite-magnetite vein sample MLZ-09. (C) Coarse grain pyroxene and actinolite. Pyroxene-actinolite vein sample MLZ-24-A. (D) Subhedral titanite crystal with small rutile grains. Also observed are small pyrite grains. Pyroxene-actinolite vein sample MLZ-03-A. (E) Coarse-grained pyroxene, actinolite, chlorite, magnetite, apatite and plagioclase. Hydrothermal breccias sample MLZ-26. (F) Fine-grained pyroxene, actinolite, chlorite, magnetite

and plagioclase. Hydrothermal breccias sample MLZ-27. (G) Anhedral magnetite grains disseminated within the andesite groundmass. Disseminated magnetite sample MLZ-08. (H) Clinopyroxene altered to chlorite and abundant disseminated magnetite grains. Disseminated magnetite sample MLZ-12. Abbreviations: PPL: plane polarized light; XPL: crossed nicols; RL: reflected light; Act: actinolite; Ap: apatite; Chl: chlorite; Cpx: clinopyroxene (augite); Mag: magnetite; Opx: orthopyroxene (hypersthene); Phl: phlogopite; Pl: plagioclase (andesine-oligoclase in anhedral matrix); Px: pyroxene; Py: pyrite; Rut: rutile; Tit: titanite.

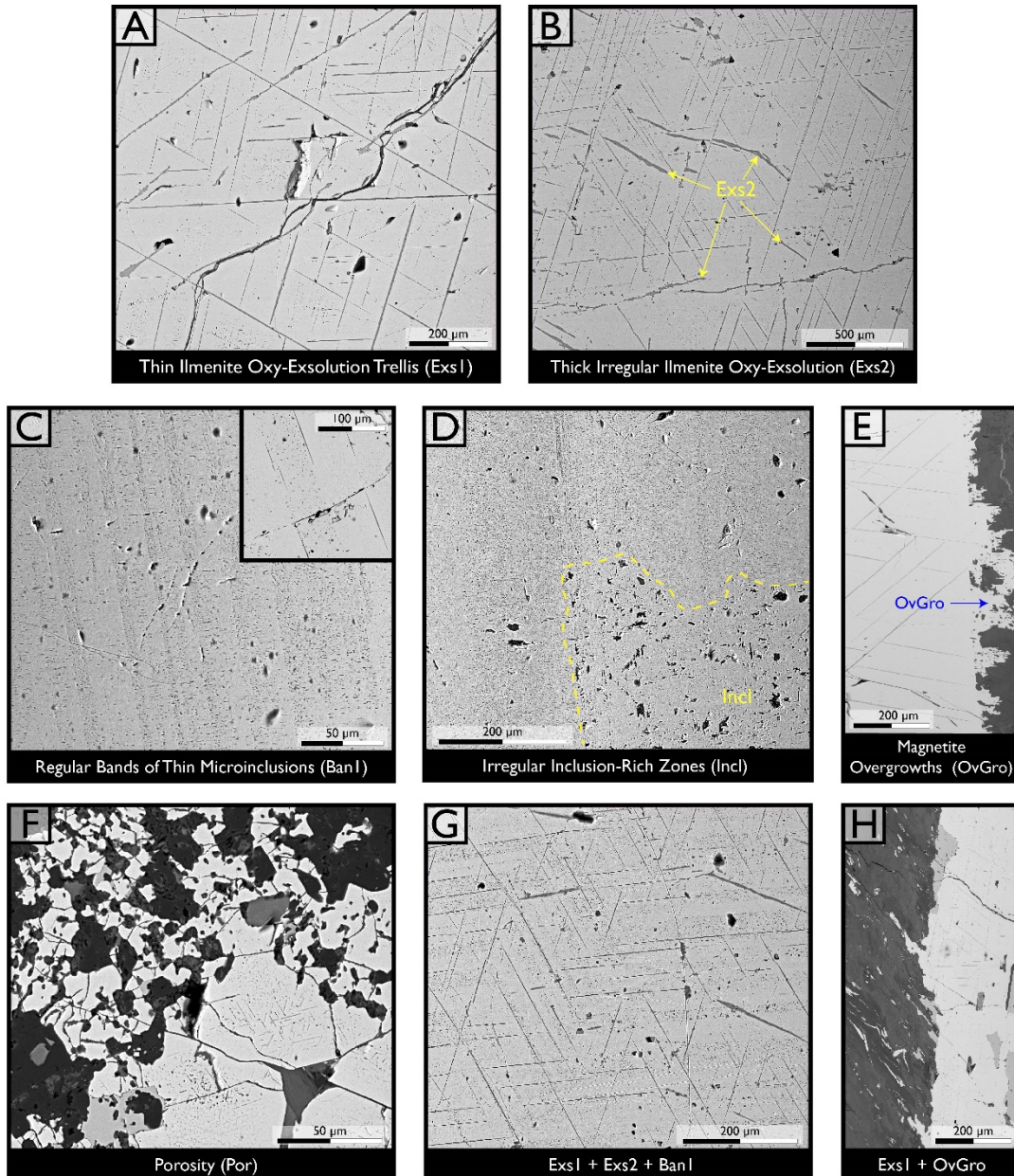


Figure 12. SEM images of magnetite textures. Inset in (C) shows thin ilmenite oxy-exsolutions aligned with the direction of the regular bands of thin microinclusions.

<i>Mineralization Style</i>	<i>Mineralogy</i>	<i>Magnetite Textures</i>	<i>Samples</i>
Massive Magnetite	Major: Mag Minor: Opx, Cpx, Ap, Biot, Zr, Rut, Ilm, Py, Th	Thin Ilmenite Oxy-Exsolution Trellis Regular Bands of Thin Microinclusions Irregular Inclusion-Rich Zones	MLM-09 * MLZ-04-B * MLZ-06-A MLZ-06-B *
Pyroxene-Actinolite-Magnetite Veins	Major: Mag, Opx, Cpx, Ap, Amph (Act) Minor: Chl, Amph (Cumm), Rut, Ilm	Thin Ilmenite Oxy-Exsolution Trellis Thick Irregular Ilmenite Oxy-Exsolution Regular Bands of Thin Microinclusions Irregular Inclusion-Rich Zones Overgrowths	MLM-01 * MLZ-09 * MLZ-28-A MLZ-28-C
Hydrothermal Breccias	Major: Mag, Opx, Cpx, Ap, Chl, Amph (Act) Minor: Cal, Qz, Rut, Ilm, Py, Tit	Thin Ilmenite Oxy-Exsolution Trellis Thick Irregular Ilmenite Oxy-Exsolution Regular Bands of Thin Microinclusions Porosity	MLM-02 * MLM-05 * MLZ-02 * MLZ-26 MLZ-27
Disseminated Magnetite	Major: Mag Host Rock Fundamental Mass: Major: Pl Minor: Cpx, Ap, Amph (Act), Chl, Cal, Qz, Th, Zr, Rut, Ilm, Py, Cpy, Tit	Thin Ilmenite Oxy-Exsolution Trellis Thick Irregular Ilmenite Oxy-Exsolution Porosity	MLM-06 * MLM-12 * MLM-07 MLM-13 MLZ-01 * MLZ-21 MLZ-06-A MLZ-24-B MLZ-07 MLZ-25-C MLZ-08 MLZ-28-B MLZ-11
Pyroxene-Actinolite Veins	Major: Opx, Cpx, Ap, Chl, Amph (Act) Minor: Cal, Qz, Feld-K, Th, Zr, Rut, Ilm, Mag, Py, Cpy, Tit	Porosity	MLM-03 * MLZ-03-B MLM-08 MLZ-22 MLZ-03-A MLZ-24-A

Figure 13. Paragenesis of the different mineralization styles and observed magnetite textures. Abbreviations: Act: actinolite; Amph: amphibole; Ap: apatite; Biot: biotite; Cal: calcite; Chl: chlorite; Cpx: clinopyroxene; Cumm: cummingtonite; K-Feld: potassium feldspar; Ilm: ilmenite; Mag: magnetite; Opx: orthopyroxene; Phl: phlogopite; Pl: plagioclase; Px: pyroxene; Py: pyrite; Cpy: chalcopyrite; Qz: quartz; Rut: rutile; Th: thorite; Tit: titanite; Zr: zircon. (*): Samples analyzed by using EMPA.

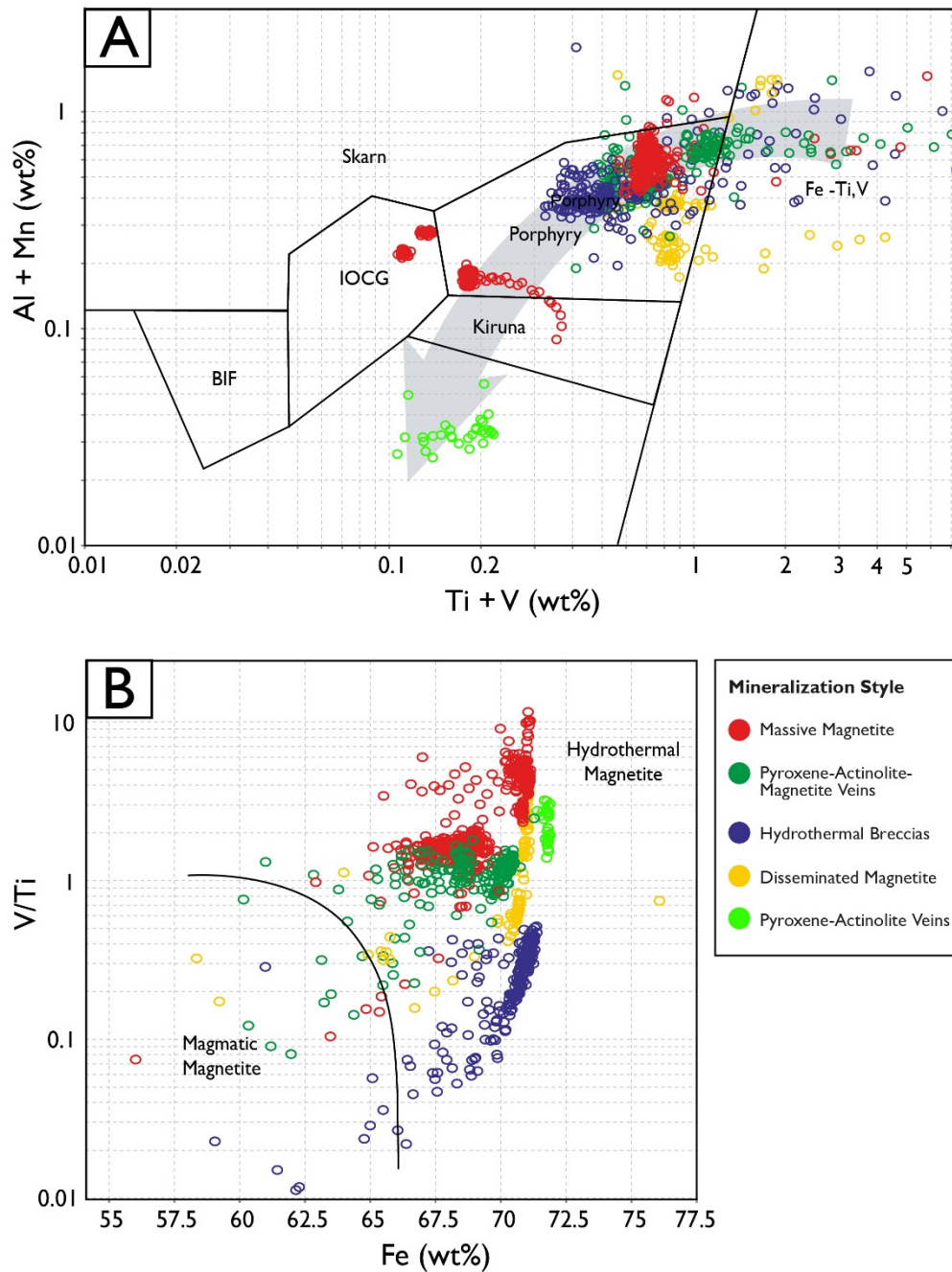


Figure 14. Bivariate plots of EMPA elemental concentrations in magnetite. (A) [Ti + V] vs [Al + Mn] diagram with deposit-type fields proposed by Nadoll et al. (2014). The inferred trace elements depletion trend in magnetite is represented by the grey arrow. (B) Fe vs V/Ti discriminant diagram with magmatic and hydrothermal fields proposed by Wen et al. (2017).

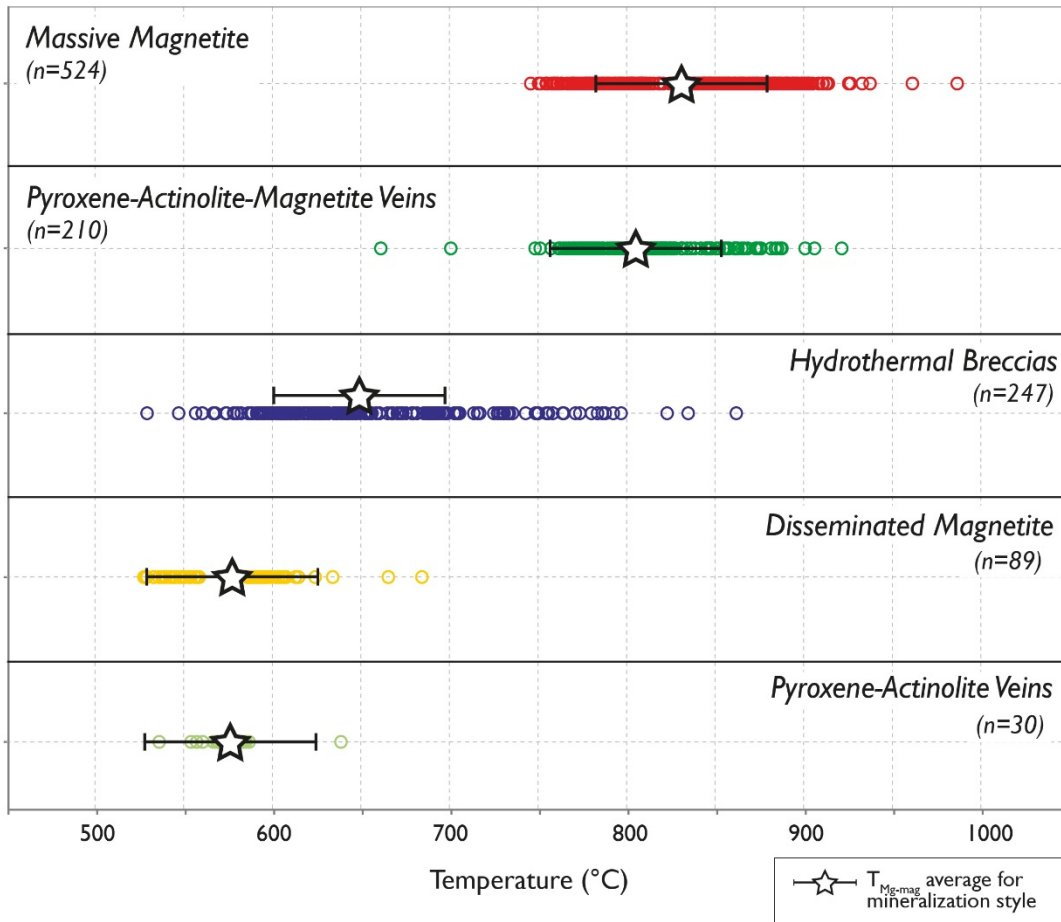


Figure 15. Crystallization temperatures determined by the Mg-in-magnetite geothermometer method proposed by Canil and Lacourse (2020).

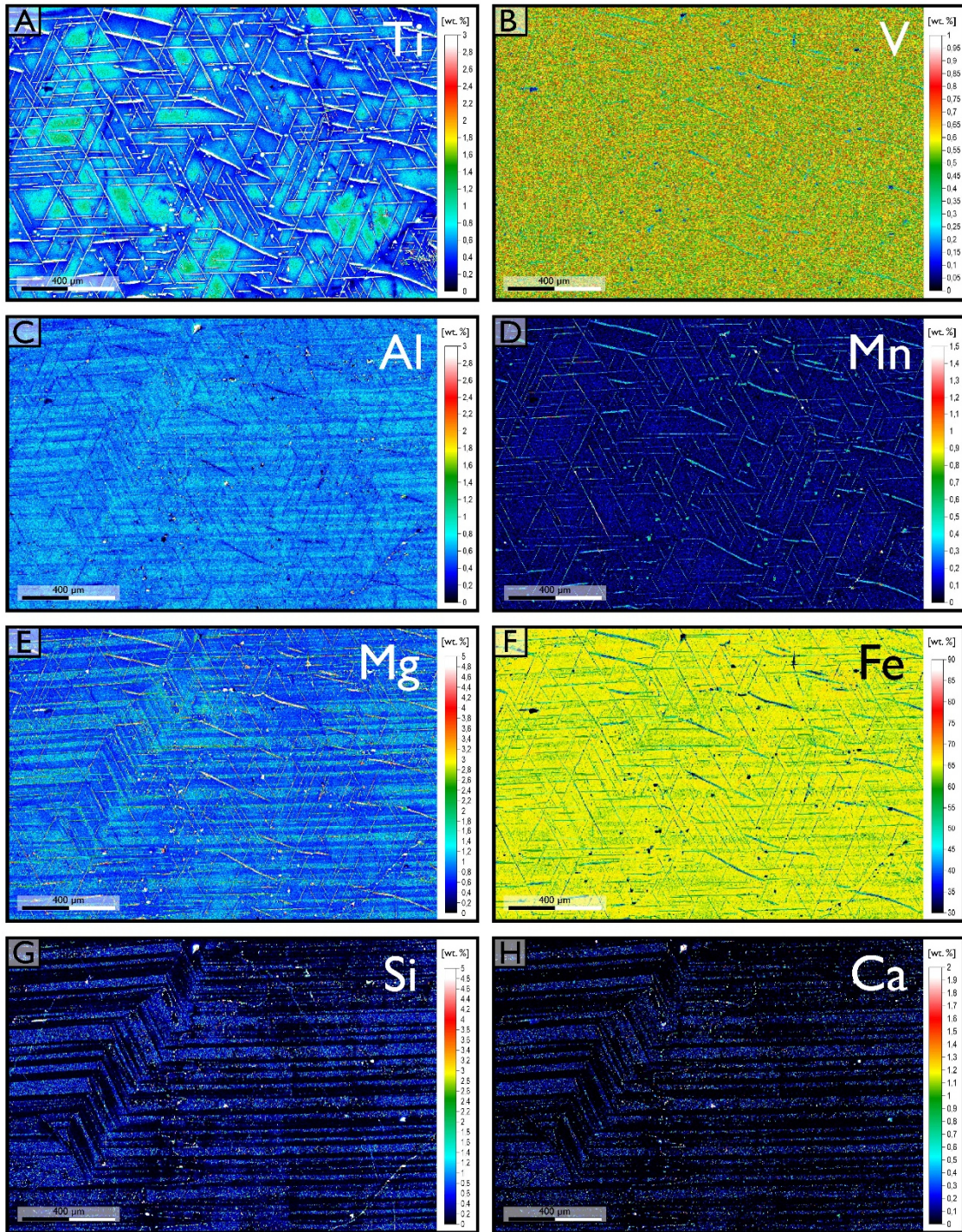


Figure 16. Quantitative WDS maps of selected elements in magnetite illustrating the complex elemental distribution associated with microtextures. Pyroxene-actinolite-magnetite vein sample MLZ-09, same as Figure 12G. The grain displays superimposed thin ilmenite oxy-exsolution trellis, thick irregular ilmenite oxy-exsolution and regular bands of thin microinclusions.

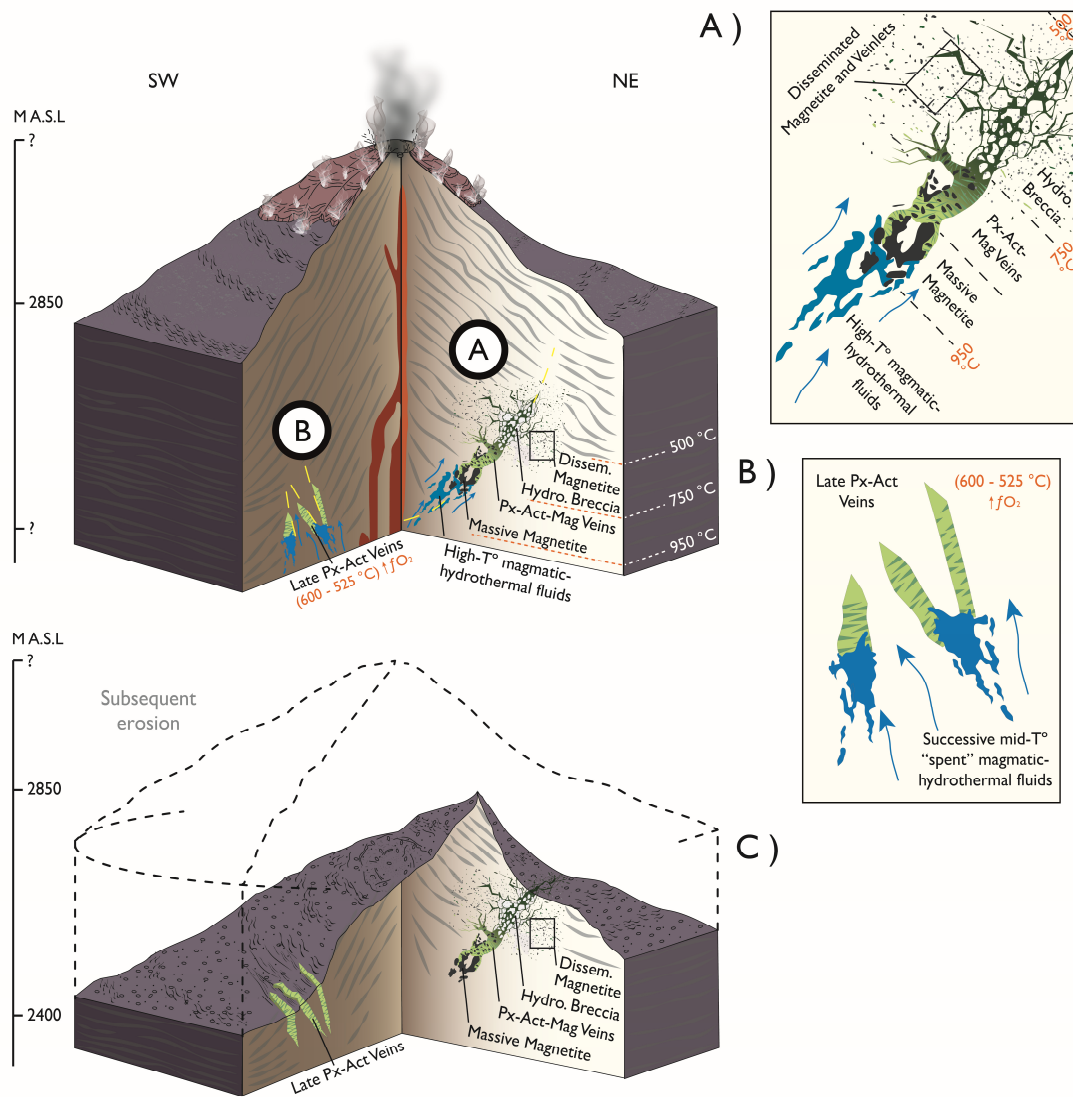


Figure 17. Schematic genetic model for the Vetás del Maule IOA-type mineralization hosted in andesites from La Zorra volcano. A) Progressive precipitation of magnetite following the sequence: massive magnetite, pyroxene-actinolite-magnetite veins, hydrothermal breccias and disseminated magnetite by magmatic-hydrothermal fluids circulating through deep faults. B) Subsequent formation of pyroxene-actinolite (\pm magnetite) veins in new zones of structural weakness, associated with low temperature and high fO_2 fluid(s) as evidenced by the magnetite geochemical signature. C) Late glacial erosion and isostatic rebound exposes the different mineralization styles. Model not to scale; the size of the mineralization styles has been greatly exaggerated for better visualization. See text for discussion.

3.9 References

- Andersen, N., Singer, B., Jicha, B., Fierstein, J., and Vazquez, J. (2013). The Development of a Restless Rhyolite Magma Chamber at Laguna del Maule, Chile. *AGU Fall Meeting Abstracts, San Francisco, California*, V51C-2676.
- Andersen, N., Singer, B., Jicha, B., Beard, B., Johnson, C., and Licciardi, J. (2017). Pleistocene to Holocene growth of a large upper crustal rhyolitic magma reservoir beneath the active Laguna del Maule volcanic field, central Chile. *Journal of Petrology*, 58, 85-114.
- Bain, W. M., Steele-MacInnis, M., Li, K., Li, L., Mazdab, F. K., and Marsh, E. E. (2020). A fundamental role of carbonate–sulfate melts in the formation of iron oxide–apatite deposits. *Nature Geoscience*, 13, 751–757.
- Bain, W. M., Steele-MacInnis, M., Tornos, F., Hanchar, J. M., Creaser, E. C., and Pietruszka, D. K. (2021). Evidence for iron-rich sulfate melt during magnetite(-apatite) mineralization at El Laco, Chile. *Geology*, 49, 1044–1048.
- Barton, M. D. (2014). Iron oxide (-Cu-Au-REE-P-Ag-U-Co) systems. In *Treatise on Geochemistry*, Elsevier, Amsterdam, vol. 13, pp. 515–541.
- Barton, M. D., and Johnson, D. A. (2004). Footprints of Fe-oxide (-Cu-Au) systems. *University of Western Australia Special Publication*, 33, 112-116.
- Borrok, D. M., Kelsner, S. E., Boer, R. H., and Essene, E. J. (1998). The Vergenoeg magnetite-fluorite deposit, South Africa; support for a hydrothermal model for massive iron oxide deposits. *Economic Geology*, 93, 564–586.
- Boutroy, E., Dare, S. S., Beaudoin, G., Barnes, S., and Lightfoot, P. (2014). Magnetite composition in Ni-Cu-PGE deposits worldwide: Application to mineral exploration. *Journal of Geochemical Exploration*, 145, 64-81.
- Buddington, A. F., and Lindsley, D. H. (1964). Iron-Titanium Oxide Minerals and Synthetic Equivalents. *Journal of Petrology*, 5, 310-357.
- Canil, D., and Lacourse, T. (2020). Geothermometry using minor and trace elements in igneous and hydrothermal magnetite. *Chemical Geology*, 541, 119576.
- Cardona, C., Tassara, A., Gil-Cruz, F., Lara, L., Morales, S., Kohler, P., and Franco, L. (2018). Crustal seismicity associated to rapid surface uplift at Laguna del Maule Volcanic Complex, Southern Volcanic Zone of the Andes. *Journal of Volcanology and Geothermal Research*, 353, 83-94.
- Cecchi, E., de Vries, B. W., and Lavest, J. M. (2004). Flank spreading and collapse of weak-cored volcanoes. *Bulletin of Volcanology*, 67, 72-91.
- Childress, T., Simon, A., Day, W. C., Lundstrom, C. C., and Bindeman, I. (2016). Iron and oxygen isotope signatures of the Pea Ridge and Pilot Knob magnetite-apatite deposits, southeast Missouri, USA. *Economic Geology*, 111, 2033-2044.

- Childress, T., Simon, A., Reich, M., Barra, F., Bilenker, L. D., La Cruz, N. L., Bindeman I. N., and Ovalle J. T. (2020). Triple Oxygen ($\delta^{18}\text{O}$, $\Delta^{17}\text{O}$), Hydrogen ($\delta^2\text{H}$), and Iron ($\delta^{56}\text{Fe}$) Stable Isotope Signatures Indicate a Silicate Magma Source and Magmatic-Hydrothermal Genesis for Magnetite Orebodies at El Laco, Chile. *Economic Geology*, 115, 1519-1536.
- Cordell, D., Unsworth, M. J., and Díaz, D. (2018). Imaging the Laguna del Maule Volcanic Field, central Chile using magnetotellurics: Evidence for crustal melt regions laterally-offset from surface vents and lava flows. *Earth and Planetary Science Letters*, 488, 168-180.
- Cox, S., Knackstedt, M., and Braun, J. (2001). Principles of structural control on permeability and fluid flow in hydrothermal systems. *SEG Reviews*, 14, 1-24.
- Corona-Esquivel, R., Levresse, G., Solé, J., Henriquez, F., and Pi, T. (2018). New age in the geological evolution of the Cerro de Mercado Iron Oxide Apatite deposit, Mexico: Implication in the Durango apatite standard (DAP) age variability. *Journal of South American Earth Sciences*, 88, 367-373.
- Dare, S. A., Barnes, S. J., and Beaudoin, G. (2015). Did the massive magnetite “lava flows” of El Laco (Chile) form by magmatic or hydrothermal processes? New constraints from magnetite composition by LA-ICP-MS. *Mineralium Deposita*, 50, 607-617.
- Day, W. C., Slack, J. F., Ayuso, R. A., and Seeger, C. M. (2016). Regional geologic and petrologic framework for iron oxide±apatite±rare earth element and iron oxide copper-gold deposits of the Mesoproterozoic St. Francois Mountains terrane, southeast Missouri, USA. *Economic Geology*, 111, 1825-1858.
- Deditius, A. P., Reich, M., Simon, A. C., Suvorova, A., Knipping, J., Roberts, M. P., and Saunders, M. (2018). Nanogeochemistry of hydrothermal magnetite. *Mineral Petrology*, 173, 46.
- Donovan, J. J., and Tingle, T. N. (1996). An improved mean atomic number background correction for quantitative microanalysis. *Microscopy and Microanalysis*, 2, 1-7.
- Dupuis, C., and Beaudoin, G. (2011). Discriminant diagrams for iron oxide trace element fingerprinting of mineral deposit types. *Mineralium Deposita*, 46, 319-335.
- Feigl, K. L., Le Mével, H., Tabrez Ali, S., Córdova, L., Andersen, N. L., DeMets, C., and Singer, B. S. (2014). Rapid uplift in Laguna del Maule volcanic field of the Andean Southern Volcanic zone. *Geophysical Journal International*, 196, 885-901.
- Fournier, T. J., Pritchard, M. E., and Riddick, S. N. (2010). Duration, magnitude, and frequency of subaerial volcano deformation events: New results from Latin America using InSAR and a global synthesis. *Geochemistry, Geophysics, Geosystems*, 11, Q01003.
- Heidarian, H., Lentz, D., Alirezaei, S., Peighambari, S., and Hall, D. (2016). Using the chemical analysis of magnetite to constrain various stages in the formation and genesis of the Kiruna-type Chadormalu magnetite-apatite deposit, Bafq district, Central Iran. *Mineralogy and Petrology*, 110, 927-942.

- Hildreth, W., and Moorbath, S. (1988). Crustal contributions to arc magmatism in the Andes of central Chile. *Contributions to Mineralogy and Petrology*, 98, 455-489.
- Hildreth, W., Godoy, E., Fierstein, J., and Singer, B. (2010). Laguna Del Maule Volcanic Field: Eruptive history of a Quaternary basalt-to-rhyolite distributed volcanic field on the Andean rangecrest in central Chile. *Boletín del Servicio Nacional de Geología y Minería*, 63, 1-145.
- Hitzman, M. W., Oreskes, N., and Einaudi, M. T. (1992). Geological characteristics and tectonic setting of proterozoic iron oxide (Cu, U, Au, REE) deposits. *Precambrian Research*, 58, 241-287.
- Hou, T., Charlier, B., Holtz, F., Veksler, I., Zhang, Z., Thomas, R., and Namur, O. (2018). Immiscible hydrous Fe–Ca–P melt and the origin of iron oxide-apatite ore deposits. *Nature Communications*, 9, 1-8.
- Hu, H., Lentz, D., Li, J., McCarron, T., Zhao, X., and Hall, D. (2015). Reequilibration processes in magnetite from iron skarn deposits. *Economic Geology*, 111, 1–8.
- Huang, X. W., and Beaudoin, G. (2019). Textures and Chemical Compositions of Magnetite from Iron Oxide Copper-Gold (IOCG) and Kiruna-Type Iron Oxide-Apatite (IOA) Deposits and Their Implications for Ore Genesis and Magnetite Classification Schemes. *Economic Geology*, 114, 953-979.
- Huang, X. W., and Beaudoin, G. (2021). Nano-inclusions in zoned magnetite from the Sossego IOCG deposit, Carajás, Brazil: Implication for mineral zoning and magnetite origin discrimination. *Ore Geology Reviews*, 139, 104453.
- Jonsson, E., Troll, V., Högdahl, K., Harris, C., Weis, F., Nilsson, K. P., and Skelton, A. (2013). Magmatic origin of giant ‘Kiruna-type’ apatite-iron-oxide ores in Central Sweden. *Scientific Reports*, 3, 1644.
- Knipping, J. L., Bilinker, L. D., Simon, A. C., Reich, M., Barra, F., Deditius, A. P., and Munizaga, R. (2015a). Giant Kiruna-type deposits form by efficient flotation of magmatic magnetite suspensions. *Geology*, 43, 591-594.
- Knipping, J. L., Bilinker, L. D., Simon, A. C., Reich, M., Barra, F., Deditius, A. P., and Munizaga, R. (2015b). Trace elements in magnetite from massive iron oxide-apatite deposits indicate a combined formation by igneous and magmatic-hydrothermal processes. *Geochimica et Cosmochimica Acta*, 171, 15-38.
- Kohn, M. J. (2017). Titanite petrochronology. *Reviews in Mineralogy and Geochemistry*, 83, 419-441.
- La Cruz, N. L., Ovalle, J. T., Simon, A. C., Konecke, B. A., Barra, F., Reich, M., Leisen, M., and Childress, T. M. (2020). The geochemistry of magnetite and apatite from the El Laco iron oxide-apatite deposit, Chile: Implications for ore genesis. *Economic Geology*, 115, 1461-1491.
- Le Mével, H., Gregg, P. M., and Feigl, K. L. (2016). Magma injection into a long-lived reservoir to explain geodetically measured uplift: application to the 2007–2014 un-

- rest episode at Laguna del Maule volcanic field, Chile. *Journal of Geophysical Research: Solid Earth*, *121*, 6092-6108.
- Lledo, H. L., and Jenkins, D. M. (2008). Experimental investigation of the upper thermal stability of Mg-rich actinolite; implications for Kiruna-type iron deposits. *Journal of Petrology*, *49*, 225-238.
- Mungall, J. E., Long, K., Brennan, J. M., Smythe, D., and Naslund, H. R. (2018). Immiscible shoshonitic and Fe-P-oxide melts preserved in unconsolidated tephra at El Laco volcano, Chile. *Geology*, *46*, 255-258.
- Nadoll, P., Angerer, T., Mauk, J. L., French, D., and Walshe, J. (2014). The chemistry of hydrothermal magnetite: A review. *Ore Geology Reviews*, *61*, 1-32.
- Naranjo, J. A., Henríquez, F., and Nyström, J. O. (2010). Subvolcanic contact metasomatism at El Laco volcanic complex, central Andes. *Andean Geology*, *37*, 110-120.
- Naslund, H. R., Henríquez, F., Nyström, J. O., Vivallo, W., and Dobbs, F. M. (2002). Magmatic iron ores and associated mineralization: examples from the Chilean high Andes and coastal Cordillera. In: *Hydrothermal Iron Oxide-Copper-Gold: A Global Perspective*, PGC Publishing, Adelaide, vol. 2, pp. 207-226.
- Novoa, C., Rémy, D., Gerbault, M., Baez, J., Tassara, A., Cordova, L., Cardona, C., Granger, M., Bonvalot, F., and Delgado, F. (2019). Viscoelastic relaxation: A mechanism to explain the decennial large surface displacements at the Laguna del Maule silicic volcanic complex. *Earth and Planetary Science Letters*, *521*, 46-59.
- Nyström, J. O., and Henríquez, F. (1994). Magmatic features of iron ores of the Kiruna type in Chile and Sweden; ore textures and magnetite geochemistry. *Economic Geology*, *89*, 820-839.
- Olivares, V., Cembrano, J., Arancibia, G., Reyes, N., Herrera, V., and Faulkner, D. (2010). Significado tectónico y migración de fluidos hidrotermales en una red de fallas y vetas de un Dúplex de rumbo: un ejemplo del Sistema de Falla de Atacama. *Andean Geology*, *37*, 473-497.
- Ovalle, J. T., La Cruz, N. L., Reich, M., Barra, F., Simon, A. C., Konecke, B. A., Rodríguez-Mustafa, M., Deditius, A., Childress, T. and Morata, D. (2018). Formation of massive iron deposits linked to explosive volcanic eruptions. *Scientific Reports*, *8*, 1-11.
- Palma, G., Barra, F., Reich, M., Valencia, V., Simon, A., Vervoort, J., and Romero, R. (2019). Halogens, trace element concentrations, and Sr-Nd isotopes in apatite from iron oxide-apatite (IOA) deposits in the Chilean iron belt: Evidence for magmatic and hydrothermal stages of mineralization. *Geochimica et Cosmochimica Acta*, *246*, 515-540.
- Palma, G., Barra, F., Reich, M., Simon, A., and Romero, R. (2020). A review of magnetite geochemistry of Chilean iron oxide-apatite (IOA) deposits and its implications for ore-forming processes. *Ore Geology Reviews*, *126*, 103748.

- Palma, G., Reich, M., Barra, F., Ovalle, J. T., Real, I., and Simon, A. (2021). Thermal Evolution of Andean Iron Oxide-Apatite (IOA) Deposits as Revealed by Magnetite Thermometry. *Scientific Reports*, *11*, 18424.
- Pardo-Casas, F., and Molnar, P. (1987). Relative motion of the Nazca (Farallon) and South American plates since Late Cretaceous time. *Tectonics*, *6*, 233-248.
- Parente, C. V., Vieira Veríssimo, C. U., Francisquini, N., Perez Xavier, R., Menez, J., de Oliveira, R., Araújo da Silva, C. D., and Saraiva dos Santos, T. J. (2019). Geology, petrography and mineral chemistry of iron oxide-apatite occurrences (IOA type), western sector of the neoproterozoic Santa Quitéria magmatic arc, Ceará northeast, Brazil. *Ore Geology Reviews*, *112*, 103024.
- Peters, S. T., Alibabae, N., Pack, A., McKibbin, S. J., Raeisi, D., Nayebi, N., Torab, F., Ireland, T., and Lehmann, B. (2019). Triple oxygen isotope variations in magnetite from iron-oxide deposits, central Iran, record magmatic fluid interaction with evaporite and carbonate host rocks. *Geology*, *48*, 211–215.
- Putnis, A. (2009). Mineral replacement reactions. *Reviews in Mineralogy and Geochemistry*, *70*, 87-124.
- Putnis, A. (2015). Transient porosity resulting from fluid–mineral interaction and its consequences. *Reviews in Mineralogy and Geochemistry*, *80*, 1-23.
- Rhodes, A. L., and Oreskes, N. (1999). Oxygen isotope composition of magnetite deposits at El Laco, Chile: Evidence of formation from isotopically heavy fluids. In *Geology and Ore Deposits of the Central Andes*, Society of Economic Geologists Special Publication, Chelsea, Michigan, vol. 7, pp. 333-351.
- Rodriguez-Mustafa, M. A., Simon, A. C., del Real, I., Thompson, J. F., Bilenker, L. D., Barra, F., Bindeman, I., and Cadwell, D. (2020). A Continuum from Iron Oxide Copper-Gold to Iron Oxide-Apatite Deposits: Evidence from Fe and O Stable Isotopes and Trace Element Chemistry of Magnetite. *Economic Geology*, *115*, 1443–1459.
- Rojas, P., Barra, F., Deditius, A., Reich, M., Simon, A., Roberts, M., and Rojo, M. (2018). New contributions to the understanding of Kiruna-type iron oxide-apatite deposits revealed by magnetite ore and gangue mineral geochemistry at the El Romeral deposit. *Ore Geology Reviews*, *93*, 413-435.
- Rojas, A. (2019). *Mineralogía de alteración e hidroquímica del sistema volcánico-hidrotermal Laguna del Maule: implicancias en el riesgo volcánico, alzamiento superficial y recurso geotérmico*. Undergraduate Honors Thesis, Facultad de Ciencias Físicas y Matemáticas, Universidad de Chile, Santiago, Chile, 127 pp.
- Romero, J. E., Polacci, M., Watt, S., Kitamura, S., Tormey, D., Sielfeld, G., Arzilli, F., La Spina, G., Franco, L., Burton, M., and Polanco, E. (2021). Volcanic lateral collapse processes in mafic arc edifices: A review of their driving processes, types and consequences. *Frontiers in Earth Science*, *9*, 325.

- Salazar, E., Barra, F., Reich, M., Simon, A., Leisen, M., Palma, G., and Rojo, M. (2020). Trace element geochemistry of magnetite from the Cerro Negro Norte iron oxide–apatite deposit, northern Chile. *Mineralium Deposita*, 55, 409-428.
- Sibson, R., Moore, J., and Rankin, A. (1975). Seismic pumping—a hydrothermal fluid transport mechanism. *Journal of the Geological Society*, 1316, 653-659.
- Sibson, R. (2001). Seismogenic framework for hydrothermal transport and ore deposition. *Reviews in Economic Geology*, 14, 25-50.
- Sillitoe, R., and Burrows, D. (2002). New field evidence bearing on the origin of the El Laco magnetite deposit, northern Chile. *Economic Geology*, 97, 1101-1109.
- Sillitoe, R. (2003). Iron oxide-copper-gold deposits: an Andean view. *Mineralium Deposita*, 38, 787-812.
- Simon, A. C., Pettke, T., Candela, P. A., Piccoli, P. M., and Heinrich, C. A. (2004). Magnetite solubility and iron transport in magmatic-hydrothermal environments. *Geochimica et Cosmochimica Acta*, 68, 4905-4914.
- Simon, A. C., Knipping, J., Reich, M., Barra, F., Deditius, A. P., Bilenker, L., and Childress, T. (2018). Kiruna-Type Iron Oxide- Apatite (IOA) and Iron Oxide Copper-Gold (IOCG) Deposits form by a combination of igneous and magmatic-hydrothermal processes: evidence from the Chilean Iron Belt. *Society of Economic Geology: Special Publications*, 21, 89-114.
- Singer, B., Andersen, N. L., Le Mével, H., Feigl, K. L., DeMets, C., Tikoff, B., Thurber, C. H., Jicha, B., Cardona, C., Córdova, L., Gil, F., Unsworth, M. J., Williams-Jones, G., Miller, C., Fierstein, J., Hildreth, W., and Vazquez, J. (2014). Dynamics of a large, restless, rhyolitic magma system at Laguna del Maule, southern Andes, Chile. *GSA Today*, 24, 4-10.
- Singer, B., Le Mével, H., Licciardi, M., Córdova, L., Tikoff, B., Garibaldi, N., Andersen, N., Diefenbach, A., and Feigl, K. (2018). Geomorphic expression of rapid Holocene silicic magma reservoir growth beneath Laguna del Maule, Chile. *Science Advances*, 4, eaat1513.
- Tan, W., Liu, P., He, H., Wang, C. Y., and Liang, X. (2016). Mineralogy and Origin of Exsolution in Ti-rich Magnetite from Different Magmatic Fe-ti Oxide-bearing Intrusions. *The Canadian Mineralogist*, 54, 539-553.
- Tornos, F., Velasco, F., and Hanchar, J. M. (2016). Iron-rich melts, magmatic magnetite, and superheated hydrothermal systems: The El Laco deposit, Chile. *Geology*, 44, 427-430.
- Troll, V. R., Weis, F. A., Jonsson, E., Andersson, U. B., Majidi, S. A., Högdahl, K., Harris, C., Millet, M. A., Saravanan Chinnasamy, S., Koojiman, E., and Nilsson, K. P. (2019). Global Fe–O isotope correlation reveals magmatic origin of Kiruna-type apatite-iron-oxide ores. *Nature Communications*, 10, 1-12.

- Velasco, F., Tornos, F., and Hanchar, J. M. (2016). Immiscible iron- and silica-rich melts and magnetite geochemistry at the El Laco volcano (northern Chile): Evidence for a magmatic origin for the magnetite deposits. *Ore Geology Reviews*, 79, 346-366.
- Wang, Y., Zhu, W., Huang, H., Bai, Z., Zhong, H., Yao, J., and Fan, H. (2020). Geochemistry of magnetite from the giant Paleoproterozoic Dahongshan Fe-Cu deposit, SW China: Constraints on nature of ore-forming fluids and depositional setting. *Ore Geology Reviews*, 118, 103361.
- Wen, G., Li, J. W., Hofstra, A. H., Koenig, A. E., Lowers, H. A., and Adams, D. (2017). Hydrothermal reequilibration of igneous magnetite in altered granitic plutons and its implications for magnetite classification schemes: Insights from the Handan-Xingtai iron district. North China Craton. *Geochimica et Cosmochimica Acta*, 213, 255–270.
- Wespestad, C. E., Thurber, C. H., Andersen, N. L., Singer, B. S., Cardona, C., Zeng, X., Bennington, N. L., Keranen, K., Peterson, D. E., Cordell, D., Unsworth, M., Miller, C., and Williams-Jones, G. (2019). Magma reservoir below Laguna del Maule volcanic field, Chile, imaged with surface-wave tomography. *Journal of Geophysical*, 124, 2858-2872.
- Westhues, A., Hanchar, J. M., LeMessurier, M. J., and Whitehouse, M. J. (2017a). Evidence for hydrothermal alteration and source regions for the Kiruna iron oxide-apatite ore (northern Sweden) from zircon Hf and O isotopes. *Geology*, 45, 571-574.
- Westhues, A., Hanchar, J. M., Voisey, C. R., Whitehouse, M. J., Rossman, G. R., and Wirth, R. (2017b). Tracing the fluid evolution of the Kiruna iron oxide apatite deposits using zircon, monazite, and whole rock trace elements and isotopic studies. *Chemical Geology*, 466, 303-322.
- Williams, P. J., Barton, M. D., Johnson, D. A., Fontboté, L., De Haller, A., Mark, G., and Marschik, R. (2005). Iron oxide copper-gold deposits: Geology, space-time distribution, and possible modes of origin. *Economic Geology, 100th Anniversary Volume*, 371-405.
- Xirouchakis, D., Lindsley, D. H., and Frost, B. R. (2001a). Ca-Mg-Fe olivine and pyroxenes, Fe-Mg-Ti oxides, and quartz: Part I. Theory. *American Mineralogist*, 86, 247-253.
- Xirouchakis, D., Lindsley, D. H., and Frost, B. R. (2001b). Assemblages with titanite (CaTiOSiO₄), Ca-Mg-Fe olivine and pyroxenes, Fe-Mg-Ti oxides, and quartz: Part II. Application. *American Mineralogist*, 86, 254-264.
- Yin, S., Wirth, R., Ma, C., and Xu, J. (2019). The role of mineral nanoparticles at a fluid-magnetite interface: Implications for trace-element uptake in hydrothermal systems. *American Mineralogist*, 104, 1180–1188.

CAPÍTULO 4

CONCLUSIONES

En este estudio se reporta la existencia de una nueva mineralización de tipo óxido de hierro-apatito (IOA) ubicada en los remanentes del volcán La Zorra (~1.0 Ma), ubicado en el Complejo Volcánico Laguna del Maule, en los Andes Centrales del Sur. La combinación de estudios de terreno que incluyeron mapeo de superficie, imágenes de dron, y observaciones petrográficas de detalle permitieron caracterizar la ocurrencia de cinco estilos de mineralización diferentes: i) cuerpos irregulares de magnetita masiva, (ii) vetas de piroxeno-actinolita-magnetita, (iii) brechas hidrotermales, (iv) magnetita diseminada y v) vetas de piroxeno-actinolita con escasa magnetita.

Estos estilos de mineralización presentan concentraciones de elementos trazas en magnetita, medidas mediante microsonda electrónica (EMPA), que configuran tendencias distintivas en diagramas de discriminación propuestos por autores anteriores. Las tendencias varían desde magnetita rica en Ti, V, Al y Mn asociada a condiciones magmático-hidrotermales, baja fO_2 y alta temperatura (ej. tipos i-ii), hacia magnetita progresivamente más empobrecida en Ti, V, Al y Mn asociada a condiciones típicamente hidrotermales, caracterizadas por mayor fO_2 y menor temperatura (ej. tipo v). La evolución composicional de la magnetita es coincidente con una tendencia de descenso de temperatura determinado mediante el geotermómetro empírico de Mg en magnetita. Estas temperaturas describen un enfriamiento continuo desde ~950 °C a ~500 °C para los estilos de mineralización descritos, desde (i), (ii), (iii), (iv) hacia (v), lo que es consistente con la evolución y enfriamiento de un fluido magmático-hidrotermal. Estas tendencias son análogas a aquellas reportadas para los depósitos tipo IOA de la Franja Ferrífera Chilena y el depósito de El Laco en el Altiplano del norte de Chile, recientemente documentadas por Palma et al. (2021).

La mineralización de Vetas del Maule registra además una amplia variedad de microtexturas de magnetita, las cuales también han sido reportadas en otros depósitos de tipo IOA, entre ellas, oxi-exsoluciones de ilmenita tipo trellis, bandas de microinclusiones, zonaciones oscilatorias, sobrecrecimientos, y microporosidad. Estas ocurren en un amplio rango de temperaturas y estilos mineralización y en ocasiones dispuestas en combinaciones

de dos o más texturas dentro del mismo grano, lo que revela una compleja evolución textural reflejo de condiciones fisicoquímicas fluctuantes.

Los datos obtenidos en esta investigación sugieren que la mineralización tipo IOA de Vetas del Maule se formó a partir de un fluido magmático-hidrotermal que se inyectó desde un reservorio hidrotermal en profundidad a través de fallas profundas en el volcán La Zorra. La magnetita masiva y vetas de piroxeno-actinolita-magnetita estarían asociadas a precipitación a mayores temperaturas ($\sim 950\text{--}750^\circ\text{C}$) mientras que las brechas hidrotermales y magnetita diseminada estarían relacionadas a temperaturas de formación intermedias ($\sim 750\text{--}550^\circ\text{C}$). En contraposición, las vetas de piroxeno-actinolita se habrían formado a partir de fluidos hidrotermales de menor temperatura ($\sim 600\text{--}525^\circ\text{C}$), posiblemente en una etapa más tardía. La inyección del(os) fluido(s) mineralizante(s) estaría directamente relacionada con la evolución magmático-hidrotermal del volcán La Zorra, y probablemente asociado a un reservorio de fluido hidrotermal en profundidad. La inyección de dicho fluido sería eventualmente desencadenada por procesos de sobrepresión en el reservorio, y/o fracturamiento y descompresión relacionados a procesos de pérdida de masa del edificio volcánico (ej. colapso de flanco).

Finalmente, y a modo de conclusión, es importante mencionar que los procesos que dieron origen a la mineralización de tipo IOA de Vetas del Maule probablemente son similares a aquellos reportados en depósitos IOA subvolcánicos/aéreos, y en particular al depósito de El Lago en los Andes del norte de Chile. Sin embargo, los resultados presentados en este estudio no permiten discriminar de manera precisa los procesos volcánico-hidrotermales involucrados, siendo éstos materia de estudio de futuras investigaciones. En consecuencia, los datos aquí reportados abren nuevas posibilidades para estudiar la génesis de los depósitos IOA, y los factores que controlan su mineralización. Más aún, el estudio de Vetas del Maule proporciona evidencia de que la mineralización IOA de tipo subvolcánico/aérea puede ser más común de lo que se piensa, brindando nuevas oportunidades para la investigación y exploración de este tipo de depósitos en arcos volcánicos modernos.

BIBLIOGRAFÍA

- Andersen, N., Singer, B., Jicha, B., Fierstein, J., and Vazquez, J. (2013). The Development of a Restless Rhyolite Magma Chamber at Laguna del Maule, Chile. *AGU Fall Meeting Abstracts, San Francisco, California*, V51C-2676.
- Andersen, N., Singer, B., Jicha, B., Beard, B., Johnson, C., and Licciardi, J. (2017). Pleistocene to Holocene growth of a large upper crustal rhyolitic magma reservoir beneath the active Laguna del Maule volcanic field, central Chile. *Journal of Petrology*, 58, 85-114.
- Arancibia, G., Cembrano, J., and Lavenu, A. (1999). Transpresión dextral y partición de la deformación en la Zona de Falla Liquiñe–Ofqui, Aysén, Chile (44-45°S). *Revista Geológica de Chile*, 26, 3-22.
- Astaburuaga, D. (2014). *Evolución estructural del límite mesozoico-cenoico de la cordillera principal entre 35°30' y 36°S, región del Maule, Chile*. Undergraduate Honors Thesis, Facultad de Ciencias Físicas y Matemáticas, Universidad de Chile, Santiago, Chile, 128 pp.
- Bain, W. M., Steele-MacInnis, M., Li, K., Li, L., Mazdab, F. K., and Marsh, E. E. (2020). A fundamental role of carbonate–sulfate melts in the formation of iron oxide–apatite deposits. *Nature Geoscience*, 13, 751–757.
- Bain, W. M., Steele-MacInnis, M., Tornos, F., Hanchar, J. M., Creaser, E. C., and Pietruszka, D. K. (2021). Evidence for iron-rich sulfate melt during magnetite(-apatite) mineralization at El Laco, Chile. *Geology*, 49, 1044–1048.
- Barton, M. D. (2014). Iron oxide (-Cu-Au-REE-P-Ag-U-Co) systems. In *Treatise on Geochemistry*, Elsevier, Amsterdam, vol. 13, pp. 515–541.
- Barton, M. D., and Johnson, D. A. (2004). Footprints of Fe-oxide (-Cu-Au) systems. *University of Western Australia Special Publication*, 33, 112-116.
- Cardona, C., Tassara, A., Gil-Cruz, F., Lara, L., Morales, S., Kohler, P., and Franco, L. (2018). Crustal seismicity associated to rapid surface uplift at Laguna del Maule Volcanic Complex, Southern Volcanic Zone of the Andes. *Journal of Volcanology and Geothermal Research*, 353, 83-94.
- Cembrano, J., Lavenu, A., Reynolds, P., Arancibia, G., López, G., and Sanhueza, A. (2002). Late Cenozoic transpressional ductile deformation north of the Nazca–South America–Antarctica triple junction. *Tectonophysics*, 354, 289-314.
- Charrier, R., Wyss, A., Flynn, J. J., Swisher III, C. C., Norell, M. A., Zapatta, F., McKenna, M., and Novacek, M. J. (1996). New evidence for Late Mesozoic-Early Cenozoic evolution of the Chilean Andes in the Upper Tinguiririca Valley (35°S), central Chile. *Journal of South American Earth Sciences*, 9, 393-422.

- Childress, T., Simon, A., Day, W. C., Lundstrom, C. C., and Bindeman, I. (2016). Iron and oxygen isotope signatures of the Pea Ridge and Pilot Knob magnetite-apatite deposits, southeast Missouri, USA. *Economic Geology*, *111*, 2033-2044.
- Cordell, D., Unsworth, M. J., and Díaz, D. (2018). Imaging the Laguna del Maule Volcanic Field, central Chile using magnetotellurics: Evidence for crustal melt regions laterally-offset from surface vents and lava flows. *Earth and Planetary Science Letters*, *488*, 168-180.
- Corona-Esquivel, R., Levresse, G., Solé, J., Henriquez, F., and Pi, T. (2018). New age in the geological evolution of the Cerro de Mercado Iron Oxide Apatite deposit, Mexico: Implication in the Durango apatite standard (DAP) age variability. *Journal of South American Earth Sciences*, *88*, 367-373.
- Dare, S. A., Barnes, S. J., and Beaudoin, G. (2015). Did the massive magnetite “lava flows” of El Laco (Chile) form by magmatic or hydrothermal processes? New constraints from magnetite composition by LA-ICP-MS. *Mineralium Deposita*, *50*, 607-617.
- Day, W. C., Slack, J. F., Ayuso, R. A., and Seeger, C. M. (2016). Regional geologic and petrologic framework for iron oxide±apatite±rare earth element and iron oxide copper-gold deposits of the Mesoproterozoic St. Francois Mountains terrane, southeast Missouri, USA. *Economic Geology*, *111*, 1825-1858.
- Drake, R. E. (1976). Chronology of Cenozoic igneous and tectonic events in the central Chilean Andes-latitudes 36°30' to 36°S. *Journal of Volcanology and Geothermal Research*, *1*, 265-284.
- Dupuis, C., and Beaudoin, G. (2011). Discriminant diagrams for iron oxide trace element fingerprinting of mineral deposit types. *Mineralium Deposita*, *46*, 319-335.
- Feigl, K. L., Le Mével, H., Tabrez Ali, S., Córdova, L., Andersen, N. L., DeMets, C., and Singer, B. S. (2014). Rapid uplift in Laguna del Maule volcanic field of the Andean Southern Volcanic zone. *Geophysical Journal International*, *196*, 885-901.
- Flynn, J. J., Wyss, A. R., and Charrier, R. (2007). South America’s missing mammals. *Scientific American*, *296*, 68-75.
- Flynn, J. J., Wyss, A. R., Croft, D. A., and Charrier, R. (2003). The Tinguiririca Fauna, Chile: biochronology, paleoecology, biogeography, and a new earliest Oligocene South American Land Mammal Age. *Palaeogeography, Palaeoclimatology, Palaeoecology*, *195*, 229-259.
- Folguera, A., and Ramos, V. (2001). Distribución de la deformación en los Andes australes (33-46° S). *Revista de la Asociación Geológica Argentina, Serie D: Publicación Especial*, *5*, 13-18.
- Fournier, T. J., Pritchard, M. E., and Riddick, S. N. (2010). Duration, magnitude, and frequency of subaerial volcano deformation events: New results from Latin America

- using InSAR and a global synthesis. *Geochemistry, Geophysics, Geosystems*, *11*, Q01003.
- González, F. O., and Vergara, M. (1962). Reconocimiento geológico de la Cordillera de los Andes entre los paralelos 35° y 38° latitud sur. *Publicaciones de la Universidad de Chile, Instituto de Geología*, *24*, 1-121.
- Heidarian, H., Lentz, D., Alirezaei, S., Peighambari, S., and Hall, D. (2016). Using the chemical analysis of magnetite to constrain various stages in the formation and genesis of the Kiruna-type Chadormalu magnetite-apatite deposit, Bafq district, Central Iran. *Mineralogy and Petrology*, *110*, 927-942.
- Hildreth, W., and Moorbath, S. (1988). Crustal contributions to arc magmatism in the Andes of central Chile. *Contributions to Mineralogy and Petrology*, *98*, 455-489.
- Hildreth, W. (2004). Volcanological perspectives on Long Valley, Mammoth Mountain, and Mono Craters: several contiguous but discrete systems. *Journal of Volcanology and Geothermal Research*, *136*, 169-198.
- Hildreth, W., Godoy, E., Fierstein, J., and Singer, B. (2010). Laguna Del Maule Volcanic Field: Eruptive history of a Quaternary basalt-to-rhyolite distributed volcanic field on the Andean rangecrest in central Chile. *Boletín del Servicio Nacional de Geología y Minería*, *63*, 1-145.
- Hitzman, M. W., Oreskes, N., and Einaudi, M. T. (1992). Geological characteristics and tectonic setting of proterozoic iron oxide (Cu, U, Au, REE) deposits. *Precambrian Research*, *58*, 241-287.
- Hou, T., Charlier, B., Holtz, F., Veksler, I., Zhang, Z., Thomas, R., and Namur, O. (2018). Immiscible hydrous Fe–Ca–P melt and the origin of iron oxide-apatite ore deposits. *Nature Communications*, *9*, 1-8.
- Huang, X. W., and Beaudoin, G. (2019). Textures and Chemical Compositions of Magnetite from Iron Oxide Copper-Gold (IOCG) and Kiruna-Type Iron Oxide-Apatite (IOA) Deposits and Their Implications for Ore Genesis and Magnetite Classification Schemes. *Economic Geology*, *114*, 953-979.
- Jonsson, E., Troll, V., Högdahl, K., Harris, C., Weis, F., Nilsson, K. P., and Skelton, A. (2013). Magmatic origin of giant ‘Kiruna-type’ apatite-iron-oxide ores in Central Sweden. *Scientific Reports*, *3*, 1644.
- Knipping, J. L., Bilenker, L. D., Simon, A. C., Reich, M., Barra, F., Deditius, A. P., and Munizaga, R. (2015a). Giant Kiruna-type deposits form by efficient flotation of magmatic magnetite suspensions. *Geology*, *43*, 591-594.
- Knipping, J. L., Bilenker, L. D., Simon, A. C., Reich, M., Barra, F., Deditius, A. P., and Munizaga, R. (2015b). Trace elements in magnetite from massive iron oxide-apatite

- deposits indicate a combined formation by igneous and magmatic-hydrothermal processes. *Geochimica et Cosmochimica Acta*, 171, 15-38.
- Lavenu, A., and Cembrano, J. (1999). Compressional-and transpressional-stress pattern for Pliocene and quaternary brittle deformation in fore arc and intra-arc zones (Andes of central and southern Chile). *Journal of Structural Geology*, 21, 1669-1691.
- Le Mével, H., Gregg, P. M., and Feigl, K. L. (2016). Magma injection into a long-lived reservoir to explain geodetically measured uplift: application to the 2007–2014 unrest episode at Laguna del Maule volcanic field, Chile. *Journal of Geophysical Research: Solid Earth*, 121, 6092-6108.
- Melnick, D., Rosenau, M., Folguera, A., and Echtler, H. (2006). Neogene tectonic evolution of the Neuquén Andes western flank (37–39° S). *Geological Society of America, Special Paper*, 407, 73-95.
- Menard, J. (1990). Ore deposit genesis in the Chilean iron belt (Atacama area, Chile). *International Symposium on Andean Geodynamics, Grenoble*, 313-317.
- Miller, C. A., Le Mével, H., Currenti, G., Williams-Jones, G., and Tikoff, B. (2017a). 4D gravity changes at the Laguna del Maule volcanic field: magma induced stress changes facilitate mass addition. *Journal of Geophysical Research*, 122, 3179-3196.
- Mungall, J. E., Long, K., Brenan, J. M., Smythe, D., and Naslund, H. R. (2018). Immiscible shoshonitic and Fe-P-oxide melts preserved in unconsolidated tephra at El Laco volcano, Chile. *Geology*, 46, 255-258.
- Muñoz, J., and Niemeyer, H. (1984). *Hoja Laguna del Maule: Regiones del Maule y del BioBio*. Carta geológica de Chile 1: 250.000, Servicio Nacional de Geología y Minería.
- Nadoll, P., Angerer, T., Mauk, J. L., French, D., and Walshe, J. (2014). The chemistry of hydrothermal magnetite: A review. *Ore Geology Reviews*, 61, 1-32.
- Naranjo, J. A., Henríquez, F., and Nyström, J. O. (2010). Subvolcanic contact metasomatism at El Laco volcanic complex, central Andes. *Andean Geology*, 37, 110-120.
- Naslund, H. R., Henríquez, F., Nyström, J. O., Vivallo, W., and Dobbs, F. M. (2002). Magmatic iron ores and associated mineralization: examples from the Chilean high Andes and coastal Cordillera. In: *Hydrothermal Iron Oxide-Copper-Gold: A Global Perspective*, PGC Publishing, Adelaide, vol. 2, pp. 207-226.
- Nelson, S. T., Davidson, J. P., Heizler, M. T., and Kowallis, B. J. (1999). Tertiary tectonic history of the southern Andes: The subvolcanic sequence to the Tatara–San Pedro volcanic complex, lat 36°S. *Geological Society of America Bulletin*, 111, 1387-1404.
- Novoa, C., Rémy, D., Gerbault, M., Baez, J., Tassara, A., Cordova, L., Cardona, C., Granger, M., Bonvalot, F., and Delgado, F. (2019). Viscoelastic relaxation: A mechanism to

- explain the decennial large surface displacements at the Laguna del Maule silicic volcanic complex. *Earth and Planetary Science Letters*, 521, 46-59.
- Nyström, J. O., and Henriquez, F. (1994). Magmatic features of iron ores of the Kiruna type in Chile and Sweden; ore textures and magnetite geochemistry. *Economic geology*, 89, 820-839.
- Ovalle, J. T., La Cruz, N. L., Reich, M., Barra, F., Simon, A. C., Konecke, B. A., Rodriguez-Mustafa, M., Deditius, A., Childress, T. and Morata, D. (2018). Formation of massive iron deposits linked to explosive volcanic eruptions. *Scientific Reports*, 8, 1-11.
- Oyarzún, J., and Frutos, J. (1984). Tectonic and petrological frame of the Cretaceous iron deposits of north Chile. *Mining Geology*, 34, 21-31.
- Palma, G., Barra, F., Reich, M., Simon, A., and Romero, R. (2020). A review of magnetite geochemistry of Chilean iron oxide-apatite (IOA) deposits and its implications for ore-forming processes. *Ore Geology Reviews*, 126, 103748.
- Palma, G., Reich, M., Barra, F., Ovalle, J. T., Real, I., and Simon, A. (2021). Thermal Evolution of Andean Iron Oxide-Apatite (IOA) Deposits as Revealed by Magnetite Thermometry. *Scientific Reports*, 11, 18424.
- Pardo-Casas, F., and Molnar, P. (1987). Relative motion of the Nazca (Farallon) and South American plates since Late Cretaceous time. *Tectonics*, 6, 233-248.
- Peters, S. T., Alibabaei, N., Pack, A., McKibbin, S. J., Raeisi, D., Nayebi, N., Torab, F., Ireland, T., and Lehmann, B. (2019). Triple oxygen isotope variations in magnetite from iron-oxide deposits, central Iran, record magmatic fluid interaction with evaporite and carbonate host rocks. *Geology*, 48, 211–215.
- Pichon, R. (1981). *Contribution à l'étude de la ceinture de fer du Chili. Les gisements de Bandurrias (Province d'Atacama) et Los Colorados Norte (Province de Huasco)*. Doctoral Honors Thesis, Université de Paris, Paris, France, 326 pp.
- Pose, F. (2007). *Geología de la región de las nacientes del Río Barrancas, Provincia de Neuquén*. Undergraduate Honors Thesis, Facultad de Ciencias Exactas y Naturales, Universidad de Buenos Aires, Buenos Aires, Argentina, 135 pp.
- Reyes-Wagner, V., Díaz, D., Cordell, D., and Unsworth, M. (2017). Regional electrical structure of the Andean subduction zone in central Chile (35°–36°S) using magnetotellurics. *Earth Planets Space*, 69, 1-9.
- Rhodes, A. L., and Oreskes, N. (1999). Oxygen isotope composition of magnetite deposits at El Laco, Chile: Evidence of formation from isotopically heavy fluids. In *Geology and Ore Deposits of the Central Andes*, Society of Economic Geologists Special Publication, Chelsea, Michigan, vol. 7, pp. 333-351.
- Ruiz, C., Aguirre, L., Corvalán, J., Klohn, C., Klohn, E., and Levi, B. (1965). *Geología y yacimientos metalíferos de Chile*, Instituto de Investigaciones Geológicas, Santiago.

- Siebert, L., Simkin, T., and Kimberly, P. (2011). *Volcanoes of the World*, University of California Press and Smithsonian Institution, London.
- Sillitoe, R., and Burrows, D. (2002). New field evidence bearing on the origin of the El Laco magnetite deposit, northern Chile. *Economic Geology*, *97*, 1101-1109.
- Sillitoe, R. (2003). Iron oxide-copper-gold deposits: an Andean view. *Mineralium Deposita*, *38*, 787-812.
- Simon, A. C., Knipping, J., Reich, M., Barra, F., Deditius, A. P., Bilenker, L., and Childress, T. (2018). Kiruna-Type Iron Oxide- Apatite (IOA) and Iron Oxide Copper-Gold (IOCG) Deposits form by a combination of igneous and magmatic-hydrothermal processes: evidence from the Chilean Iron Belt. *Society of Economic Geology: Special Publications*, *21*, 89-114.
- Singer, B., Andersen, N., Le Mével, H., Feigl, K., DeMets, C., Tikoff, B., Thurber, C. H., Jicha, B., Cardona, C., Córdova, L., Gil, F., Unsworth, M. J., Williams-Jones, G., Miller, C., Fierstein, J., Hildreth, W., and Vazquez, J. (2014). Dynamics of a large, restless, rhyolitic magma system at Laguna del Maule, southern Andes, Chile. *GSA today*, *24*, 4-10.
- Singer, B., Le Mével, H., Licciardi, M., Córdova, L., Tikoff, B., Garibaldi, N., Andersen, N., Diefenbach, A., and Feigl, K. (2018). Geomorphic expression of rapid Holocene silicic magma reservoir growth beneath Laguna del Maule, Chile. *Science Advances*, *4*, eaat1513.
- Tornos, F., Velasco, F., and Hanchar, J. M. (2016). Iron-rich melts, magmatic magnetite, and superheated hydrothermal systems: The El Laco deposit, Chile. *Geology*, *44*, 427-430.
- Velasco, F., Tornos, F., and Hanchar, J. M. (2016). Immiscible iron- and silica-rich melts and magnetite geochemistry at the El Laco volcano (northern Chile): Evidence for a magmatic origin for the magnetite deposits. *Ore Geology Reviews*, *79*, 346-366.
- Westhues, A., Hanchar, J. M., LeMessurier, M. J., and Whitehouse, M. J. (2017a). Evidence for hydrothermal alteration and source regions for the Kiruna iron oxide-apatite ore (northern Sweden) from zircon Hf and O isotopes. *Geology*, *45*, 571-574.
- Westhues, A., Hanchar, J. M., Voisey, C. R., Whitehouse, M. J., Rossman, G. R., and Wirth, R. (2017b). Tracing the fluid evolution of the Kiruna iron oxide apatite deposits using zircon, monazite, and whole rock trace elements and isotopic studies. *Chemical Geology*, *466*, 303-322.
- Williams, P. J., Barton, M. D., Johnson, D. A., Fontboté, L., De Haller, A., Mark, G., and Marschik, R. (2005). Iron oxide copper-gold deposits: Geology, space-time distribution, and possible modes of origin. *Economic Geology, 100th Anniversary Volume*, 371-405.

ANEXO: MATERIAL SUPLEMENTARIO PARA EL CAPÍTULO 3
ORIGEN DE LA MINERALIZACIÓN DE HIERRO DEL COMPLEJO VOLCÁNICO
LAGUNA DEL MAULE, CHILE: ¿UN NUEVO EJEMPLO DE DEPÓSITO TIPO ÓXIDO DE
HIERRO-APATITO EN LOS ANDES?

Este archivo incluye:

Tabla Suplementaria 1: Resumen de las condiciones de los análisis EMPA.

Tabla Suplementaria 2: Análisis EMPA realizados en magnetita.

Tabla Suplementaria 3: Análisis EMPA realizados en silicatos.

Tabla Suplementaria 4: Temperaturas de cristalización de magnetita calculadas mediante el geotermómetro de Mg en magnetita propuesto por Canil y Lacourse (2020).

Tabla Suplementaria 5: Resumen estadístico de los análisis EMPA realizados en magnetita.

Tabla Suplementaria 1: Resumen de las condiciones de los análisis EMPA.

Electron Microprobe Analyses - Analytical Conditions

Oxygen calculated by stoichiometry.

*Background corrections for all elements made using the Mean Atomic Number (MAN) Method of Donovan and Tingle (1996)

Donovan, J.J., and Tingle, T.N. (1996) An Improved Mean Atomic Number Correction for Quantitative Microanalysis. *Journal of Microscopy*, v. 2, 1, pp. 1-7.

**Off-peak backgrounds measured for 50% of peak counting time

Fe-Ti Oxides

Instrument	Intensity Correction	Accelerating Voltage (kV)	Beam Current (nA)	Beam Size (µm)
JEOL JXA8530F, CMCA/U. Western Australia	Self-calibrated correction for Si, Na, K, Ni, Mn	20	40 - 50	Fully focused; point mode

Element-Line	Peak Counting Time (s)**	Analyzing Crystal	Calibration Standard	MDL [wt.%]
Si Kα	60	TAP	Quartz - GP40 Amelia Albite	0.006
Al Kα	60	TAP	Corundum - GP40 Synthetic Corundum	0.006
Na Kα	30	TAP	Jadeite - GP40 Amelia Albite	0.029
Mg Kα	60	TAP	Periclase - GP40 Periclase	0.011
Ti Kα	60	PETJ	Rutile - GP40 Ti Metal	0.003
Ca Kα	60	PETJ	Wollastonite - GP40 Wollastonite (Willsboro)	0.003
K Kα	30	PETJ	Orthoclase - GP40 Alkali Feldspar	0.005
Fe Kα	20	LiF	Magnetite - GP40 Fe Metal	0.010
Cr Kα	60	LiF	Cr2O3 - GP40 Cr Metal	0.003
Ni Kα	60	LiF	Ni - GP40 Ni Metal	0.008
V Kα	60	LiF	V - GP40 V Metal	0.004
Mn Kα	60	LiF	Mn - GP40 Mn Metal	0.004
Zn Kα	60	LiF	Zn - GP40 Zn Metal	0.012
Cu Kα	60	LiF	Cu - GP40 Cu Metal	0.008

Silicates

Instrument	Intensity Correction	Accelerating Voltage (kV)	Beam Current (nA)	Beam Size (µm)
JEOL JXA8530F, CMCA/U. Western Australia	Self-calibrated correction for Si, Na, K, Ni, Mn	15	20	Fully focused; point mode or defocused 5 microns

Element	Peak Counting Time (s)*	Analyzing Crystal	Calibration Standard	MDL [wt.%]
Si Kα	20	TAP	GP40 Alkali Feldspar	0.005
Al Kα	20	TAP	GP40 Synthetic Corundum	0.005
Na Kα	20	TAP	GP40 Amelia Albite	0.010
Mg Kα	20	TAP	GP40 Periclase	0.004
Ti Kα	60	LiF	GP40 Ti Metal	0.012
Ca Kα	20	PETJ	GP40 Wollastonite (Willsboro)	0.004
K Kα	20	PETJ	GP40 Alkali Feldspar	0.004
Fe Kα	20	LiF	GP40 Fe Metal	0.011
Cr Kα	60	LiF	GP40 Cr Metal	0.010
Ni Kα	60	LiF	GP40 Ni Metal	0.016
V Kα	60	LiF	GP40 V Metal	0.011
Mn Kα	60	LiF	GP40 Mn Metal	0.011
Zn Kα	60	LiF	GP40 Zn Metal	0.020
Cu Kα	60	LiF	GP40 Cu Metal	0.020
P Kα	60	PETJ	GP40 Gallium Phosphide	0.005
S Kα	60	PET	SP00100 Syn. ZnS (Sphalerite)	0.004

ID	Transect	Sample	Mineralization Style	Texture	Si	Al	Na	Mg	Ti	Ca	K	Fe	Co	Ni	V	Mn	Zn	Cu	P	S	O	Total
					[wt. %]	[wt. %]	[wt. %]	[wt. %]	[wt. %]	[wt. %]	[wt. %]	[wt. %]	[wt. %]	[wt. %]	[wt. %]	[wt. %]	[wt. %]	[wt. %]	[wt. %]	[wt. %]	[wt. %]	
1301	T4B	MLZ-09	Act-Px-Mag Veins	Exs1 + Exs2 + Ban1	0.41	0.55	0.30	1.36	1.82	0.14	0.01	64.23	b.d	No Data	0.55	0.10	b.d	b.d	No Data	No Data	28.06	97.54
1302	T4B	MLZ-09	Act-Px-Mag Veins	Exs1 + Exs2 + Ban1	1.29	0.67	0.48	1.40	0.53	0.53	0.02	63.79	b.d	No Data	0.54	0.08	b.d	b.d	No Data	No Data	28.38	97.73
1303	T4B	MLZ-09	Act-Px-Mag Veins	Exs1 + Exs2 + Ban1	0.11	0.56	0.29	0.94	0.57	0.01	b.d	66.79	b.d	No Data	0.57	0.09	b.d	b.d	No Data	No Data	27.54	97.49
1304	T4B	MLZ-09	Act-Px-Mag Veins	Exs1 + Exs2 + Ban1	0.10	0.53	0.14	0.89	0.53	0.01	0.01	66.64	b.d	No Data	0.56	0.07	b.d	b.d	No Data	No Data	27.33	96.82
1305	T4B	MLZ-09	Act-Px-Mag Veins	Exs1 + Exs2 + Ban1	0.13	0.46	0.41	1.90	5.48	0.01	b.d	59.52	b.d	No Data	0.50	0.21	b.d	b.d	No Data	No Data	28.64	97.27
1306	T4B	MLZ-09	Act-Px-Mag Veins	Exs1 + Exs2 + Ban1	0.11	0.53	0.34	0.85	0.42	0.01	b.d	66.61	b.d	No Data	0.56	0.08	b.d	b.d	No Data	No Data	27.28	96.80
1307	T4B	MLZ-09	Act-Px-Mag Veins	Exs1 + Exs2 + Ban1	0.11	0.61	0.36	0.89	0.46	0.01	b.d	67.04	b.d	No Data	0.57	0.08	b.d	b.d	No Data	No Data	27.59	97.73
1308	T4B	MLZ-09	Act-Px-Mag Veins	Exs1 + Exs2 + Ban1	0.10	0.55	0.40	0.83	0.47	0.01	b.d	66.65	b.d	No Data	0.56	0.08	b.d	b.d	No Data	No Data	27.37	97.05
1309	T4B	MLZ-09	Act-Px-Mag Veins	Exs1 + Exs2 + Ban1	0.10	0.58	0.32	0.89	0.44	0.01	b.d	66.82	b.d	No Data	0.57	0.08	b.d	b.d	No Data	No Data	27.44	97.27
1310	T4B	MLZ-09	Act-Px-Mag Veins	Exs1 + Exs2 + Ban1	0.11	0.52	0.43	1.36	2.55	0.01	0.00	64.26	b.d	No Data	0.56	0.13	b.d	b.d	No Data	No Data	28.19	98.13
1311	T4B	MLZ-09	Act-Px-Mag Veins	Exs1 + Exs2 + Ban1	0.10	0.52	0.24	0.84	0.45	0.02	b.d	66.89	b.d	No Data	0.58	0.08	b.d	b.d	No Data	No Data	27.36	97.08
1312	T4B	MLZ-09	Act-Px-Mag Veins	Exs1 + Exs2 + Ban1	0.12	0.59	0.35	0.92	0.57	0.02	b.d	66.66	b.d	No Data	0.55	0.08	b.d	b.d	No Data	No Data	27.52	97.39
1313	T4B	MLZ-09	Act-Px-Mag Veins	Exs1 + Exs2 + Ban1	0.11	0.52	0.48	0.94	0.59	0.02	b.d	67.80	b.d	No Data	0.56	0.07	b.d	b.d	No Data	No Data	27.96	99.06
1314	T4B	MLZ-09	Act-Px-Mag Veins	Exs1 + Exs2 + Ban1	0.11	0.44	0.24	0.85	2.35	0.01	b.d	65.49	b.d	No Data	0.53	0.12	b.d	b.d	No Data	No Data	28.04	98.19
1315	T4B	MLZ-09	Act-Px-Mag Veins	Exs1 + Exs2 + Ban1	0.13	0.52	0.37	1.23	6.23	0.01	b.d	59.27	b.d	No Data	0.50	0.24	b.d	b.d	No Data	No Data	27.14	95.65
1724	130r	MLZ-12	Disseminated		5.79	3.36	1.23	0.10	0.68	0.05	1.20	58.25	b.d	No Data	0.12	0.03	b.d	b.d	No Data	No Data	27.55	98.36
1652	19	MLZ-01	Disseminated	Exs1 + Exs2	0.03	0.29	0.09	0.13	0.42	b.d	b.d	76.08	0.01	No Data	0.31	0.02	b.d	b.d	No Data	No Data	22.63	96.05

Tabla Suplementaria 4: Temperaturas de cristalización de magnetita calculadas mediante el geotermómetro de Mg en magnetita propuesto por Canil y Lacourse (2020).

ID	Transect	Sample	Mineralization Style	Texture	Mg	T°mean
					[wt. %] Norm.	
901	T1	MLZ-04-B	Massive Mag	Ban1	1.25	864.74
902	T1	MLZ-04-B	Massive Mag	Ban1	1.16	852.30
903	T1	MLZ-04-B	Massive Mag	Ban1	1.25	864.52
904	T1	MLZ-04-B	Massive Mag	Ban1	1.28	868.42
905	T1	MLZ-04-B	Massive Mag	Ban1	1.39	881.56
906	T1	MLZ-04-B	Massive Mag	Ban1	1.13	847.72
907	T1	MLZ-04-B	Massive Mag	Ban1	1.37	878.88
908	T1	MLZ-04-B	Massive Mag	Ban1	1.19	856.26
909	T1	MLZ-04-B	Massive Mag	Ban1	1.25	864.09
910	T1	MLZ-04-B	Massive Mag	Ban1	1.26	865.37
911	T1	MLZ-04-B	Massive Mag	Ban1	1.15	850.34
912	T1	MLZ-04-B	Massive Mag	Ban1	1.19	856.65
913	T1	MLZ-04-B	Massive Mag	Ban1	1.25	864.22
914	T1	MLZ-04-B	Massive Mag	Ban1	1.26	865.37
915	T1	MLZ-04-B	Massive Mag	Ban1	1.26	865.06
916	T1	MLZ-04-B	Massive Mag	Ban1	1.19	855.54
917	T1	MLZ-04-B	Massive Mag	Ban1	1.24	863.60
918	T1	MLZ-04-B	Massive Mag	Ban1	1.40	882.28
919	T1	MLZ-04-B	Massive Mag	Ban1	1.15	850.95
920	T1	MLZ-04-B	Massive Mag	Ban1	1.45	888.17
921	T1	MLZ-04-B	Massive Mag	Ban1	1.56	901.35
922	T1	MLZ-04-B	Massive Mag	Ban1	1.45	890.01
923	T1	MLZ-04-B	Massive Mag	Ban1	1.66	912.01
924	T1	MLZ-04-B	Massive Mag	Ban1	1.42	885.45
925	T1	MLZ-04-B	Massive Mag	Ban1	1.33	873.99
926	T1	MLZ-04-B	Massive Mag	Ban1	1.42	885.30
927	T1	MLZ-04-B	Massive Mag	Ban1	1.39	881.34
928	T1	MLZ-04-B	Massive Mag	Ban1	1.26	865.88
929	T1	MLZ-04-B	Massive Mag	Ban1	1.26	866.59
930	T1	MLZ-04-B	Massive Mag	Ban1	1.25	864.56
931	T1	MLZ-04-B	Massive Mag	Ban1	1.42	885.57
932	T1	MLZ-04-B	Massive Mag	Ban1	1.51	895.09
933	T1	MLZ-04-B	Massive Mag	Ban1	1.36	877.73
935	T1	MLZ-04-B	Massive Mag	Ban1	1.49	894.06
936	T1	MLZ-04-B	Massive Mag	Ban1	1.31	871.77
937	T1	MLZ-04-B	Massive Mag	Ban1	1.24	862.93
938	T1	MLZ-04-B	Massive Mag	Ban1	1.42	885.05
939	T1	MLZ-04-B	Massive Mag	Ban1	1.32	872.34
940	T1	MLZ-04-B	Massive Mag	Ban1	1.43	887.43
941	T1A	MLZ-04-B	Massive Mag	Ban1	1.78	924.26
942	T1A	MLZ-04-B	Massive Mag	Ban1	1.37	879.51
943	T1A	MLZ-04-B	Massive Mag	Ban1	1.43	886.16
944	T1A	MLZ-04-B	Massive Mag	Ban1	1.27	866.72

ID	Transect	Sample	Mineralization Style	Texture	Mg [wt. %]	T°mean
945	T1A	MLZ-04-B	Massive Mag	Banl	1.54	899.37
946	T1A	MLZ-04-B	Massive Mag	Banl	1.28	868.14
947	T1A	MLZ-04-B	Massive Mag	Banl	1.20	858.32
948	T1A	MLZ-04-B	Massive Mag	Banl	1.04	835.60
949	T1A	MLZ-04-B	Massive Mag	Banl	1.03	833.99
950	T1A	MLZ-04-B	Massive Mag	Banl	1.06	837.81
951	T1A	MLZ-04-B	Massive Mag	Banl	1.02	833.08
952	T1A	MLZ-04-B	Massive Mag	Banl	1.05	836.50
953	T1A	MLZ-04-B	Massive Mag	Banl	1.03	833.56
954	T1A	MLZ-04-B	Massive Mag	Banl	1.02	832.17
955	T1A	MLZ-04-B	Massive Mag	Banl	1.05	836.16
956	T1A	MLZ-04-B	Massive Mag	Banl	1.03	834.42
957	T1A	MLZ-04-B	Massive Mag	Banl	1.06	837.67
958	T1A	MLZ-04-B	Massive Mag	Banl	1.02	832.80
959	T1A	MLZ-04-B	Massive Mag	Banl	1.02	832.07
960	T1A	MLZ-04-B	Massive Mag	Banl	1.20	857.54
961	T1A	MLZ-04-B	Massive Mag	Banl	1.23	860.32
962	T1A	MLZ-04-B	Massive Mag	Banl	1.01	830.33
963	T1A	MLZ-04-B	Massive Mag	Banl	1.32	873.57
964	T1A	MLZ-04-B	Massive Mag	Banl	1.38	879.45
965	T1A	MLZ-04-B	Massive Mag	Banl	1.27	866.48
966	T1A	MLZ-04-B	Massive Mag	Banl	1.39	881.60
967	T1A	MLZ-04-B	Massive Mag	Banl	1.46	890.17
968	T1A	MLZ-04-B	Massive Mag	Banl	1.33	874.01
969	T1A	MLZ-04-B	Massive Mag	Banl	1.41	883.62
970	T1A	MLZ-04-B	Massive Mag	Banl	1.21	858.51
971	T1A	MLZ-04-B	Massive Mag	Banl	1.11	845.17
972	T1A	MLZ-04-B	Massive Mag	Banl	1.36	878.19
973	T1A	MLZ-04-B	Massive Mag	Banl	1.23	861.50
974	T1A	MLZ-04-B	Massive Mag	Banl	1.17	853.33
975	T1A	MLZ-04-B	Massive Mag	Banl	1.26	864.72
976	T1A	MLZ-04-B	Massive Mag	Banl	1.11	844.80
977	T1A	MLZ-04-B	Massive Mag	Banl	1.11	845.20
978	T1A	MLZ-04-B	Massive Mag	Banl	1.30	870.36
979	T1A	MLZ-04-B	Massive Mag	Banl	1.25	863.41
980	T1A	MLZ-04-B	Massive Mag	Banl	1.09	842.88
981	T1B	MLZ-04-B	Massive Mag		1.17	854.27
982	T1B	MLZ-04-B	Massive Mag		1.02	833.12
983	T1B	MLZ-04-B	Massive Mag		1.00	830.35
984	T1B	MLZ-04-B	Massive Mag		1.34	875.99
985	T1B	MLZ-04-B	Massive Mag		1.15	851.59
986	T1B	MLZ-04-B	Massive Mag		0.98	826.86
987	T1B	MLZ-04-B	Massive Mag		0.96	823.30
988	T1B	MLZ-04-B	Massive Mag		0.97	824.58
989	T1B	MLZ-04-B	Massive Mag		1.22	860.18
990	T1B	MLZ-04-B	Massive Mag		0.97	824.47
991	T2A	MLZ-04-B	Massive Mag	Incl	1.15	850.49
992	T2A	MLZ-04-B	Massive Mag	Incl	1.16	852.20
993	T2A	MLZ-04-B	Massive Mag	Incl	1.14	848.42

ID	Transect	Sample	Mineralization Style	Texture	Mg [wt. %]	T°mean
994	T2A	MLZ-04-B	Massive Mag	Incl	1.12	845.96
995	T2A	MLZ-04-B	Massive Mag	Incl	1.10	843.14
996	T2A	MLZ-04-B	Massive Mag	Incl	1.10	844.58
997	T2A	MLZ-04-B	Massive Mag	Incl	1.14	848.77
998	T2A	MLZ-04-B	Massive Mag	Incl	1.14	848.52
999	T2A	MLZ-04-B	Massive Mag	Incl	1.18	855.19
1000	T2A	MLZ-04-B	Massive Mag	Incl	1.25	863.23
1001	T2A	MLZ-04-B	Massive Mag	Incl	1.23	862.27
1002	T2A	MLZ-04-B	Massive Mag	Incl	1.38	880.24
1003	T2A	MLZ-04-B	Massive Mag	Incl	1.34	875.44
1004	T2A	MLZ-04-B	Massive Mag	Incl	1.52	896.71
1005	T2A	MLZ-04-B	Massive Mag	Incl	1.52	897.07
1006	T2A	MLZ-04-B	Massive Mag	Incl	1.25	863.61
1007	T2A	MLZ-04-B	Massive Mag	Incl	2.45	985.53
1008	T2A	MLZ-04-B	Massive Mag	Incl	1.24	862.48
1009	T2A	MLZ-04-B	Massive Mag	Incl	1.40	880.51
1010	T2A	MLZ-04-B	Massive Mag	Incl	1.07	839.79
1011	T2A	MLZ-04-B	Massive Mag	Incl	1.36	877.30
1012	T2A	MLZ-04-B	Massive Mag	Incl	1.32	872.17
1013	T2A	MLZ-04-B	Massive Mag	Incl	1.24	861.85
1014	T2A	MLZ-04-B	Massive Mag	Incl	1.02	832.32
1015	T2A	MLZ-04-B	Massive Mag	Incl	1.12	846.36
1016	T2A	MLZ-04-B	Massive Mag	Incl	1.20	857.69
1017	T2A	MLZ-04-B	Massive Mag	Incl	1.19	856.16
1018	T2A	MLZ-04-B	Massive Mag	Incl	1.37	879.63
1019	T2A	MLZ-04-B	Massive Mag	Incl	1.89	936.35
1020	T2A	MLZ-04-B	Massive Mag	Incl	1.07	840.06
1021	T2A	MLZ-04-B	Massive Mag	Incl	1.18	854.08
1022	T2A	MLZ-04-B	Massive Mag	Incl	1.10	843.96
1023	T2A	MLZ-04-B	Massive Mag	Incl	1.09	842.56
1024	T2A	MLZ-04-B	Massive Mag	Incl	1.25	863.39
1025	T2A	MLZ-04-B	Massive Mag	Incl	1.48	893.88
1026	T2A	MLZ-04-B	Massive Mag	Incl	1.06	837.35
1027	T2A	MLZ-04-B	Massive Mag	Incl	1.22	860.06
1028	T2A	MLZ-04-B	Massive Mag	Incl	1.21	857.88
1029	T2A	MLZ-04-B	Massive Mag	Incl	1.17	853.76
1030	T2A	MLZ-04-B	Massive Mag	Incl	0.61	761.66
1031	T2A	MLZ-04-B	Massive Mag	Incl	1.20	857.07
1032	T2A	MLZ-04-B	Massive Mag	Incl	1.21	858.94
1033	T2A	MLZ-04-B	Massive Mag	Incl	1.22	859.93
1034	T2A	MLZ-04-B	Massive Mag	Incl	1.18	854.78
1035	T2A	MLZ-04-B	Massive Mag	Incl	1.54	897.39
1036	T2A	MLZ-04-B	Massive Mag	Incl	1.21	859.10
1037	T2A	MLZ-04-B	Massive Mag	Incl	1.27	865.46
1038	T2A	MLZ-04-B	Massive Mag	Incl	1.40	881.66
1039	T2A	MLZ-04-B	Massive Mag	Incl	1.22	859.62
1040	T2A	MLZ-04-B	Massive Mag	Incl	1.30	870.29
1041	T2B	MLZ-04-B	Massive Mag		1.14	848.30
1042	T2B	MLZ-04-B	Massive Mag		1.26	864.78

ID	Transect	Sample	Mineralization Style	Texture	Mg [wt. %]	T°mean
1043	T2B	MLZ-04-B	Massive Mag		0.59	758.06
1044	T2B	MLZ-04-B	Massive Mag		1.44	886.11
1045	T2B	MLZ-04-B	Massive Mag		1.21	858.01
1046	T2B	MLZ-04-B	Massive Mag		1.43	884.16
1047	T2B	MLZ-04-B	Massive Mag		1.14	848.79
1048	T2B	MLZ-04-B	Massive Mag		1.27	865.97
1049	T2B	MLZ-04-B	Massive Mag		1.23	861.37
1050	T2B	MLZ-04-B	Massive Mag		1.34	874.26
1051	T2B	MLZ-04-B	Massive Mag		1.43	885.40
1052	T2B	MLZ-04-B	Massive Mag		1.50	894.31
1053	T2B	MLZ-04-B	Massive Mag		1.49	892.91
1054	T2B	MLZ-04-B	Massive Mag		1.47	890.64
1055	T2B	MLZ-04-B	Massive Mag		1.31	870.96
1056	T2B	MLZ-04-B	Massive Mag		1.55	897.97
1057	T2B	MLZ-04-B	Massive Mag		1.28	866.91
1058	T2B	MLZ-04-B	Massive Mag		1.21	858.28
1059	T2B	MLZ-04-B	Massive Mag		1.47	889.78
1060	T2B	MLZ-04-B	Massive Mag		1.14	849.25
1061	T2B	MLZ-04-B	Massive Mag		1.19	856.33
1062	T2B	MLZ-04-B	Massive Mag		1.43	885.08
1063	T2B	MLZ-04-B	Massive Mag		1.27	866.01
1064	T2B	MLZ-04-B	Massive Mag		1.31	871.88
1065	T2B	MLZ-04-B	Massive Mag		1.36	877.52
1066	T2B	MLZ-04-B	Massive Mag		1.31	870.61
1067	T2B	MLZ-04-B	Massive Mag		1.32	872.41
1068	T2B	MLZ-04-B	Massive Mag		1.27	865.70
1069	T2B	MLZ-04-B	Massive Mag		1.47	890.38
1070	T2B	MLZ-04-B	Massive Mag		1.48	891.51
1071	T2B	MLZ-04-B	Massive Mag		1.44	886.04
1072	T2B	MLZ-04-B	Massive Mag		1.22	859.40
1073	T2B	MLZ-04-B	Massive Mag		1.36	876.99
1074	T2B	MLZ-04-B	Massive Mag		1.24	862.83
1075	T2B	MLZ-04-B	Massive Mag		1.10	843.21
1076	T2B	MLZ-04-B	Massive Mag		1.45	889.47
1077	T2B	MLZ-04-B	Massive Mag		1.62	909.49
1078	T2B	MLZ-04-B	Massive Mag		1.09	842.32
1079	T2B	MLZ-04-B	Massive Mag		1.42	884.67
1080	T2B	MLZ-04-B	Massive Mag		1.45	888.78
1081	T2B	MLZ-04-B	Massive Mag		1.58	903.77
1082	T2B	MLZ-04-B	Massive Mag		1.55	900.33
1083	T2B	MLZ-04-B	Massive Mag		1.44	888.48
1084	T2B	MLZ-04-B	Massive Mag		1.46	890.02
1085	T2B	MLZ-04-B	Massive Mag		1.20	857.50
1086	T2B	MLZ-04-B	Massive Mag		1.40	883.20
1087	T2B	MLZ-04-B	Massive Mag		1.30	870.11
1088	T2B	MLZ-04-B	Massive Mag		1.67	912.84
1089	T2B	MLZ-04-B	Massive Mag		1.17	854.19
1090	T2B	MLZ-04-B	Massive Mag		1.30	870.56
1091	T3A	MLZ-04-B	Massive Mag	Ban1	1.57	901.10

ID	Transect	Sample	Mineralization Style	Texture	Mg [wt. %]	T°mean
1092	T3A	MLZ-04-B	Massive Mag	Ban1	1.80	925.29
1093	T3A	MLZ-04-B	Massive Mag	Ban1	1.17	852.73
1094	T3A	MLZ-04-B	Massive Mag	Ban1	1.29	868.58
1095	T3A	MLZ-04-B	Massive Mag	Ban1	1.32	871.77
1096	T3A	MLZ-04-B	Massive Mag	Ban1	1.16	851.60
1097	T3A	MLZ-04-B	Massive Mag	Ban1	1.13	847.73
1098	T3A	MLZ-04-B	Massive Mag	Ban1	1.21	858.00
1099	T3A	MLZ-04-B	Massive Mag	Ban1	1.68	911.80
1100	T3A	MLZ-04-B	Massive Mag	Ban1	1.35	875.59
1101	T3A	MLZ-04-B	Massive Mag	Ban1	1.20	856.09
1102	T3A	MLZ-04-B	Massive Mag	Ban1	1.41	882.83
1103	T3A	MLZ-04-B	Massive Mag	Ban1	1.40	882.31
1104	T3A	MLZ-04-B	Massive Mag	Ban1	1.46	889.75
1105	T3A	MLZ-04-B	Massive Mag	Ban1	1.61	907.38
1106	T3A	MLZ-04-B	Massive Mag	Ban1	1.58	902.55
1108	T3A	MLZ-04-B	Massive Mag	Ban1	1.25	863.31
1109	T3A	MLZ-04-B	Massive Mag	Ban1	0.52	744.78
1110	T3A	MLZ-04-B	Massive Mag	Ban1	1.49	893.21
1111	T3A	MLZ-04-B	Massive Mag	Ban1	1.55	899.01
1112	T3A	MLZ-04-B	Massive Mag	Ban1	1.32	872.54
1113	T3A	MLZ-04-B	Massive Mag	Ban1	1.30	869.99
1114	T3A	MLZ-04-B	Massive Mag	Ban1	1.32	872.30
1115	T3A	MLZ-04-B	Massive Mag	Ban1	1.44	885.39
1116	T3A	MLZ-04-B	Massive Mag	Ban1	1.32	871.96
1117	T3A	MLZ-04-B	Massive Mag	Ban1	1.40	881.82
1118	T3A	MLZ-04-B	Massive Mag	Ban1	1.22	859.73
1119	T3A	MLZ-04-B	Massive Mag	Ban1	1.26	865.11
1120	T3A	MLZ-04-B	Massive Mag	Ban1	1.50	893.03
1121	T3A	MLZ-04-B	Massive Mag	Ban1	1.38	879.69
1122	T3A	MLZ-04-B	Massive Mag	Ban1	1.56	899.12
1123	T3A	MLZ-04-B	Massive Mag	Ban1	1.20	856.88
1124	T3A	MLZ-04-B	Massive Mag	Ban1	1.09	841.86
1125	T3A	MLZ-04-B	Massive Mag	Ban1	1.17	853.35
1126	T3A	MLZ-04-B	Massive Mag	Ban1	1.09	842.11
1127	T3A	MLZ-04-B	Massive Mag	Ban1	1.54	898.05
1128	T3A	MLZ-04-B	Massive Mag	Ban1	1.32	872.47
1129	T3A	MLZ-04-B	Massive Mag	Ban1	1.49	892.67
1131	T3A	MLZ-04-B	Massive Mag	Ban1	1.19	855.19
1132	T3A	MLZ-04-B	Massive Mag	Ban1	1.57	901.31
1134	T3A	MLZ-04-B	Massive Mag	Ban1	1.38	878.92
1135	T3A	MLZ-04-B	Massive Mag	Ban1	1.32	872.70
1136	T3A	MLZ-04-B	Massive Mag	Ban1	2.20	960.22
1137	T3A	MLZ-04-B	Massive Mag	Ban1	1.52	895.27
1138	T3A	MLZ-04-B	Massive Mag	Ban1	1.37	878.88
1139	T3A	MLZ-04-B	Massive Mag	Ban1	1.14	848.95
1140	T3A	MLZ-04-B	Massive Mag	Ban1	1.29	868.61
1141	T3B	MLZ-04-B	Massive Mag	Incl	1.16	851.27
1142	T3B	MLZ-04-B	Massive Mag	Incl	1.12	846.37
1143	T3B	MLZ-04-B	Massive Mag	Incl	1.13	846.83

ID	Transect	Sample	Mineralization Style	Texture	Mg [wt. %]	T°mean
1144	T3B	MLZ-04-B	Massive Mag	Incl	1.10	844.18
1145	T3B	MLZ-04-B	Massive Mag	Incl	1.11	844.72
1146	T3B	MLZ-04-B	Massive Mag	Incl	1.10	843.41
1147	T3B	MLZ-04-B	Massive Mag	Incl	1.07	838.96
1148	T3B	MLZ-04-B	Massive Mag	Incl	1.43	884.95
1149	T3B	MLZ-04-B	Massive Mag	Incl	1.24	862.43
1150	T3B	MLZ-04-B	Massive Mag	Incl	1.12	846.55
1151	T3B	MLZ-04-B	Massive Mag	Incl	1.66	909.87
1152	T3B	MLZ-04-B	Massive Mag	Incl	1.15	850.68
1153	T3B	MLZ-04-B	Massive Mag	Incl	1.23	860.46
1154	T3B	MLZ-04-B	Massive Mag	Incl	1.16	850.96
1155	T3B	MLZ-04-B	Massive Mag	Incl	1.16	852.53
1156	T3B	MLZ-04-B	Massive Mag	Incl	1.22	860.20
1157	T3B	MLZ-04-B	Massive Mag	Incl	1.29	867.97
1158	T3B	MLZ-04-B	Massive Mag	Incl	1.26	864.30
1159	T3B	MLZ-04-B	Massive Mag	Incl	1.18	854.07
1160	T3B	MLZ-04-B	Massive Mag	Incl	1.14	848.54
1161	T3B	MLZ-04-B	Massive Mag	Incl	1.09	841.51
1162	T3B	MLZ-04-B	Massive Mag	Incl	1.07	839.71
1163	T3B	MLZ-04-B	Massive Mag	Incl	1.04	834.65
1164	T3B	MLZ-04-B	Massive Mag	Incl	1.06	838.52
1165	T3B	MLZ-04-B	Massive Mag	Incl	1.10	843.91
1166	T3B	MLZ-04-B	Massive Mag	Incl	1.11	844.50
1167	T3B	MLZ-04-B	Massive Mag	Incl	1.17	853.08
1168	T3B	MLZ-04-B	Massive Mag	Incl	1.11	844.48
1169	T3B	MLZ-04-B	Massive Mag	Incl	1.11	844.50
1170	T3B	MLZ-04-B	Massive Mag	Incl	1.12	846.32
1171	T3B	MLZ-04-B	Massive Mag	Incl	1.09	842.82
1172	T3B	MLZ-04-B	Massive Mag	Incl	1.14	848.13
1173	T3B	MLZ-04-B	Massive Mag	Incl	1.80	924.35
1174	T3B	MLZ-04-B	Massive Mag	Incl	1.20	856.49
1175	T3B	MLZ-04-B	Massive Mag	Incl	1.19	856.30
1176	T3B	MLZ-04-B	Massive Mag	Incl	1.03	837.14
1177	T3B	MLZ-04-B	Massive Mag	Incl	1.22	859.39
1178	T3B	MLZ-04-B	Massive Mag	Incl	1.11	845.26
1179	T3B	MLZ-04-B	Massive Mag	Incl	1.12	845.60
1180	T3B	MLZ-04-B	Massive Mag	Incl	1.15	850.24
1182	T3	MLZ-06-B	Massive Mag	Exs1 + Ban1	0.77	793.83
1184	T3	MLZ-06-B	Massive Mag	Exs1 + Ban1	0.81	801.76
1186	T3	MLZ-06-B	Massive Mag	Exs1 + Ban1	0.86	810.08
1187	T3	MLZ-06-B	Massive Mag	Exs1 + Ban1	0.84	807.12
1188	T3	MLZ-06-B	Massive Mag	Exs1 + Ban1	0.77	793.64
1190	T3	MLZ-06-B	Massive Mag	Exs1 + Ban1	0.78	795.55
1191	T3	MLZ-06-B	Massive Mag	Exs1 + Ban1	0.74	788.41
1192	T3	MLZ-06-B	Massive Mag	Exs1 + Ban1	0.75	789.69
1193	T3	MLZ-06-B	Massive Mag	Exs1 + Ban1	0.77	794.73
1194	T3	MLZ-06-B	Massive Mag	Exs1 + Ban1	0.76	792.43
1196	T3	MLZ-06-B	Massive Mag	Exs1 + Ban1	0.72	785.27
1197	T3	MLZ-06-B	Massive Mag	Exs1 + Ban1	0.77	793.43

ID	Transect	Sample	Mineralization Style	Texture	Mg [wt. %]	T°mean
1199	T3	MLZ-06-B	Massive Mag	Exs1 + Ban1	0.68	776.67
1200	T3	MLZ-06-B	Massive Mag	Exs1 + Ban1	0.67	775.73
1201	T3	MLZ-06-B	Massive Mag	Exs1 + Ban1	0.68	778.32
1202	T3	MLZ-06-B	Massive Mag	Exs1 + Ban1	0.69	779.97
1203	T3	MLZ-06-B	Massive Mag	Exs1 + Ban1	0.69	779.83
1205	T3	MLZ-06-B	Massive Mag	Exs1 + Ban1	0.64	768.65
1206	T3	MLZ-06-B	Massive Mag	Exs1 + Ban1	0.64	768.52
1208	T3	MLZ-06-B	Massive Mag	Exs1 + Ban1	0.75	790.58
1209	T3	MLZ-06-B	Massive Mag	Exs1 + Ban1	1.09	845.09
1210	T3	MLZ-06-B	Massive Mag	Exs1 + Ban1	0.77	794.75
1211	T3	MLZ-06-B	Massive Mag	Exs1 + Ban1	0.57	753.66
1212	T3	MLZ-06-B	Massive Mag	Exs1 + Ban1	0.59	759.52
1213	T3	MLZ-06-B	Massive Mag	Exs1 + Ban1	0.59	758.10
1214	T3	MLZ-06-B	Massive Mag	Exs1 + Ban1	0.73	788.29
1215	T3	MLZ-06-B	Massive Mag	Exs1 + Ban1	0.63	768.22
1216	T3	MLZ-06-B	Massive Mag	Exs1 + Ban1	0.57	753.58
1217	T3	MLZ-06-B	Massive Mag	Exs1 + Ban1	0.55	750.18
1218	T3	MLZ-06-B	Massive Mag	Exs1 + Ban1	0.62	765.34
1219	T3	MLZ-06-B	Massive Mag	Exs1 + Ban1	0.55	749.19
1220	T3	MLZ-06-B	Massive Mag	Exs1 + Ban1	0.55	750.42
T14-321	T14	MLM-09	Massive Mag	Ban1	0.58	753.91
T14-322	T14	MLM-09	Massive Mag	Ban1	0.59	756.64
T14-323	T14	MLM-09	Massive Mag	Ban1	0.58	753.95
T14-324	T14	MLM-09	Massive Mag	Ban1	0.58	753.57
T14-325	T14	MLM-09	Massive Mag	Ban1	0.60	757.49
T14-326	T14	MLM-09	Massive Mag	Ban1	0.62	762.28
T14-327	T14	MLM-09	Massive Mag	Ban1	0.84	803.76
T14-328	T14	MLM-09	Massive Mag	Ban1	0.61	760.19
T14-329	T14	MLM-09	Massive Mag	Ban1	0.61	759.37
T14-330	T14	MLM-09	Massive Mag	Ban1	0.81	799.01
T14-331	T14	MLM-09	Massive Mag	Ban1	0.64	766.93
T14-333	T14	MLM-09	Massive Mag	Ban1	0.81	798.41
T14-334	T14	MLM-09	Massive Mag	Ban1	0.66	769.43
T14-335	T14	MLM-09	Massive Mag	Ban1	0.74	785.96
T14-336	T14	MLM-09	Massive Mag	Ban1	0.68	773.86
T14-337	T14	MLM-09	Massive Mag	Ban1	0.74	784.64
T14-338	T14	MLM-09	Massive Mag	Ban1	0.67	771.49
T14-340	T14	MLM-09	Massive Mag	Ban1	0.77	791.54
T14-341	T14	MLM-09	Massive Mag	Ban1	0.81	797.22
T14-342	T14	MLM-09	Massive Mag	Ban1	0.82	800.26
T14-343	T14	MLM-09	Massive Mag	Ban1	0.80	795.15
T14-344	T14	MLM-09	Massive Mag	Ban1	0.71	780.92
T14-345	T14	MLM-09	Massive Mag	Ban1	0.69	775.19
T14-346	T14	MLM-09	Massive Mag	Ban1	0.65	768.37
T14-347	T14	MLM-09	Massive Mag	Ban1	0.83	801.44
T14-348	T14	MLM-09	Massive Mag	Ban1	0.71	781.22
T14-349	T14	MLM-09	Massive Mag	Ban1	0.67	771.13
T14-350	T14	MLM-09	Massive Mag	Ban1	0.71	779.55
T14-351	T14	MLM-09	Massive Mag	Ban1	0.65	768.74

ID	Transect	Sample	Mineralization Style	Texture	Mg [wt. %]	T°mean
T14-353	T14	MLM-09	Massive Mag	Ban1	0.68	774.74
T14-354	T14	MLM-09	Massive Mag	Ban1	0.69	775.41
T14-355	T14	MLM-09	Massive Mag	Ban1	0.66	770.48
T14-356	T14	MLM-09	Massive Mag	Ban1	0.67	770.99
T14-357	T14	MLM-09	Massive Mag	Ban1	0.66	769.77
T14-358	T14	MLM-09	Massive Mag	Ban1	0.72	782.23
T14-359	T14	MLM-09	Massive Mag	Ban1	0.91	814.00
T14-360	T14	MLM-09	Massive Mag	Ban1	0.83	800.61
T14-361	T14	MLM-09	Massive Mag	Ban1	0.67	771.47
T14-362	T14	MLM-09	Massive Mag	Ban1	0.83	801.17
T14-363	T14	MLM-09	Massive Mag	Ban1	0.76	788.59
T14-364	T14	MLM-09	Massive Mag	Ban1	0.86	805.19
T14-365	T14	MLM-09	Massive Mag	Ban1	0.90	811.92
T14-366	T14	MLM-09	Massive Mag	Ban1	0.68	773.52
T14-367	T14	MLM-09	Massive Mag	Ban1	0.67	772.31
T14-368	T14	MLM-09	Massive Mag	Ban1	0.78	792.58
T14-369	T14	MLM-09	Massive Mag	Ban1	0.67	771.51
T14-370	T14	MLM-09	Massive Mag	Ban1	0.67	772.18
T14-371	T14	MLM-09	Massive Mag	Ban1	0.68	773.37
T14-372	T14	MLM-09	Massive Mag	Ban1	0.68	774.56
T14-374	T14	MLM-09	Massive Mag	Ban1	0.72	780.80
T14-375	T14	MLM-09	Massive Mag	Ban1	0.68	774.42
T14-376	T14	MLM-09	Massive Mag	Ban1	0.69	775.39
T14-377	T14	MLM-09	Massive Mag	Ban1	0.68	773.71
T14-378	T14	MLM-09	Massive Mag	Ban1	0.71	779.48
T14-379	T14	MLM-09	Massive Mag	Ban1	0.71	780.27
T14-380	T14	MLM-09	Massive Mag	Ban1	0.68	773.40
T14-381	T14	MLM-09	Massive Mag	Ban1	0.68	773.14
T14-382	T14	MLM-09	Massive Mag	Ban1	0.87	808.25
T14-383	T14	MLM-09	Massive Mag	Ban1	0.68	774.33
T14-384	T14	MLM-09	Massive Mag	Ban1	0.69	775.10
T14-385	T14	MLM-09	Massive Mag	Ban1	0.69	775.94
T14-386	T14	MLM-09	Massive Mag	Ban1	0.79	794.55
T14-387	T14	MLM-09	Massive Mag	Ban1	0.70	777.31
T14-388	T14	MLM-09	Massive Mag	Ban1	0.80	796.08
T14-389	T14	MLM-09	Massive Mag	Ban1	0.69	775.80
T14-390	T14	MLM-09	Massive Mag	Ban1	0.69	775.97
T14-391	T14	MLM-09	Massive Mag	Ban1	0.68	774.44
T14-392	T14	MLM-09	Massive Mag	Ban1	0.69	776.25
T14-394	T14	MLM-09	Massive Mag	Ban1	0.68	774.49
T14-395	T14	MLM-09	Massive Mag	Ban1	0.68	774.54
T14-396	T14	MLM-09	Massive Mag	Ban1	0.70	776.86
T14-398	T14	MLM-09	Massive Mag	Ban1	0.69	776.26
T14-399	T14	MLM-09	Massive Mag	Ban1	0.69	776.34
T14-400	T14	MLM-09	Massive Mag	Ban1	0.71	779.06
T14-401	T14	MLM-09	Massive Mag	Ban1	0.70	777.95
T14-402	T14	MLM-09	Massive Mag	Ban1	0.70	777.59
T14-403	T14	MLM-09	Massive Mag	Ban1	0.82	799.16
T14-404	T14	MLM-09	Massive Mag	Ban1	0.75	786.36

ID	Transect	Sample	Mineralization Style	Texture	Mg [wt. %]	T°mean
T14-405	T14	MLM-09	Massive Mag	Ban1	0.70	777.09
T14-406	T14	MLM-09	Massive Mag	Ban1	0.69	775.82
T14-407	T14	MLM-09	Massive Mag	Ban1	0.70	776.86
T14-408	T14	MLM-09	Massive Mag	Ban1	0.76	788.66
T14-409	T14	MLM-09	Massive Mag	Ban1	0.71	780.25
T14-410	T14	MLM-09	Massive Mag	Ban1	0.70	777.62
T14-412	T14	MLM-09	Massive Mag	Ban1	0.71	779.15
T14-413	T14	MLM-09	Massive Mag	Ban1	0.72	781.60
T14-414	T14	MLM-09	Massive Mag	Ban1	0.76	788.23
T14-415	T14	MLM-09	Massive Mag	Ban1	0.70	776.73
T14-416	T14	MLM-09	Massive Mag	Ban1	0.98	824.95
T14-417	T14	MLM-09	Massive Mag	Ban1	0.70	778.02
T14-418	T14	MLM-09	Massive Mag	Ban1	0.73	783.82
T14-419	T14	MLM-09	Massive Mag	Ban1	0.70	777.10
T14-420	T14	MLM-09	Massive Mag	Ban1	0.72	781.42
T15-421	T15	MLM-09	Massive Mag	Ban1	0.72	782.33
T15-422	T15	MLM-09	Massive Mag	Ban1	1.49	888.92
T15-423	T15	MLM-09	Massive Mag	Ban1	0.69	776.60
T15-424	T15	MLM-09	Massive Mag	Ban1	0.88	809.87
T15-425	T15	MLM-09	Massive Mag	Ban1	0.70	778.28
T15-426	T15	MLM-09	Massive Mag	Ban1	0.71	779.39
T15-427	T15	MLM-09	Massive Mag	Ban1	0.75	787.43
T15-428	T15	MLM-09	Massive Mag	Ban1	0.72	780.76
T15-429	T15	MLM-09	Massive Mag	Ban1	0.72	780.59
T15-430	T15	MLM-09	Massive Mag	Ban1	0.71	779.13
T15-431	T15	MLM-09	Massive Mag	Ban1	0.71	779.82
T15-432	T15	MLM-09	Massive Mag	Ban1	0.71	779.14
T15-433	T15	MLM-09	Massive Mag	Ban1	0.72	780.54
T15-434	T15	MLM-09	Massive Mag	Ban1	0.87	807.65
T15-435	T15	MLM-09	Massive Mag	Ban1	0.71	779.09
T15-436	T15	MLM-09	Massive Mag	Ban1	0.71	780.35
T15-437	T15	MLM-09	Massive Mag	Ban1	0.71	779.72
T15-438	T15	MLM-09	Massive Mag	Ban1	0.72	781.94
T15-439	T15	MLM-09	Massive Mag	Ban1	0.81	796.95
T15-440	T15	MLM-09	Massive Mag	Ban1	0.71	779.56
T15-441	T15	MLM-09	Massive Mag	Ban1	0.85	803.75
T15-442	T15	MLM-09	Massive Mag	Ban1	0.71	780.39
T15-443	T15	MLM-09	Massive Mag	Ban1	0.76	788.57
T15-444	T15	MLM-09	Massive Mag	Ban1	0.71	779.77
T15-445	T15	MLM-09	Massive Mag	Ban1	0.83	800.36
T15-446	T15	MLM-09	Massive Mag	Ban1	0.71	780.42
T15-447	T15	MLM-09	Massive Mag	Ban1	0.95	819.61
T15-448	T15	MLM-09	Massive Mag	Ban1	0.76	787.94
T15-449	T15	MLM-09	Massive Mag	Ban1	0.70	777.51
T15-451	T15	MLM-09	Massive Mag	Ban1	0.70	777.91
T15-452	T15	MLM-09	Massive Mag	Ban1	0.70	777.67
T15-453	T15	MLM-09	Massive Mag	Ban1	0.71	779.75
T15-455	T15	MLM-09	Massive Mag	Ban1	0.72	781.35
T15-456	T15	MLM-09	Massive Mag	Ban1	0.70	778.39

ID	Transect	Sample	Mineralization Style	Texture	Mg [wt. %]	T°mean
T15-458	T15	MLM-09	Massive Mag	Ban1	0.89	809.98
T15-459	T15	MLM-09	Massive Mag	Ban1	0.71	778.71
T15-460	T15	MLM-09	Massive Mag	Ban1	0.70	778.59
T15-461	T15	MLM-09	Massive Mag	Ban1	0.72	781.43
T15-462	T15	MLM-09	Massive Mag	Ban1	0.71	780.02
T15-463	T15	MLM-09	Massive Mag	Ban1	0.74	785.86
T15-464	T15	MLM-09	Massive Mag	Ban1	0.72	780.98
T15-465	T15	MLM-09	Massive Mag	Ban1	0.73	782.47
T15-466	T15	MLM-09	Massive Mag	Ban1	0.72	781.07
T15-467	T15	MLM-09	Massive Mag	Ban1	0.73	783.03
T15-468	T15	MLM-09	Massive Mag	Ban1	0.71	779.40
T15-469	T15	MLM-09	Massive Mag	Ban1	0.71	779.00
T15-470	T15	MLM-09	Massive Mag	Ban1	0.72	781.69
T16-471	T16	MLM-09	Massive Mag	Ban1	0.86	805.06
T16-472	T16	MLM-09	Massive Mag	Ban1	0.84	802.71
T16-473	T16	MLM-09	Massive Mag	Ban1	0.85	803.69
T16-474	T16	MLM-09	Massive Mag	Ban1	0.85	803.59
T16-475	T16	MLM-09	Massive Mag	Ban1	0.87	806.98
T16-476	T16	MLM-09	Massive Mag	Ban1	0.85	803.75
T16-477	T16	MLM-09	Massive Mag	Ban1	0.85	803.29
T16-478	T16	MLM-09	Massive Mag	Ban1	0.85	803.66
T16-479	T16	MLM-09	Massive Mag	Ban1	0.86	805.09
T16-480	T16	MLM-09	Massive Mag	Ban1	0.86	805.21
T16-481	T16	MLM-09	Massive Mag	Ban1	0.86	804.82
T16-482	T16	MLM-09	Massive Mag	Ban1	0.85	803.15
T16-483	T16	MLM-09	Massive Mag	Ban1	0.85	804.04
T16-484	T16	MLM-09	Massive Mag	Ban1	0.85	803.74
T16-485	T16	MLM-09	Massive Mag	Ban1	0.85	803.55
T16-486	T16	MLM-09	Massive Mag	Ban1	0.84	801.48
T16-487	T16	MLM-09	Massive Mag	Ban1	0.85	803.85
T16-488	T16	MLM-09	Massive Mag	Ban1	0.93	817.18
T16-489	T16	MLM-09	Massive Mag	Ban1	0.88	808.48
T16-490	T16	MLM-09	Massive Mag	Ban1	0.85	803.68
T16-491	T16	MLM-09	Massive Mag	Ban1	0.84	802.67
T16-492	T16	MLM-09	Massive Mag	Ban1	0.86	804.81
T16-493	T16	MLM-09	Massive Mag	Ban1	0.88	809.33
T16-494	T16	MLM-09	Massive Mag	Ban1	0.88	809.25
T16-495	T16	MLM-09	Massive Mag	Ban1	0.87	806.36
T16-496	T16	MLM-09	Massive Mag	Ban1	0.87	807.42
T16-497	T16	MLM-09	Massive Mag	Ban1	0.85	804.12
T16-498	T16	MLM-09	Massive Mag	Ban1	0.85	803.85
T16-500	T16	MLM-09	Massive Mag	Ban1	0.90	811.71
T16-501	T16	MLM-09	Massive Mag	Ban1	0.85	803.21
T16-502	T16	MLM-09	Massive Mag	Ban1	0.84	802.76
T16-503	T16	MLM-09	Massive Mag	Ban1	0.85	803.75
T16-504	T16	MLM-09	Massive Mag	Ban1	0.87	807.19
T16-505	T16	MLM-09	Massive Mag	Ban1	0.89	810.02
T16-506	T16	MLM-09	Massive Mag	Ban1	0.87	806.42
T16-507	T16	MLM-09	Massive Mag	Ban1	0.88	808.27

ID	Transect	Sample	Mineralization Style	Texture	Mg [wt. %]	T°mean
T16-509	T16	MLM-09	Massive Mag	Ban1	0.85	803.84
T16-510	T16	MLM-09	Massive Mag	Ban1	0.86	804.95
T17-511	T17	MLM-09	Massive Mag	Ban1	1.11	842.77
T17-512	T17	MLM-09	Massive Mag	Ban1	0.82	798.07
T17-513	T17	MLM-09	Massive Mag	Ban1	0.90	812.36
T17-514	T17	MLM-09	Massive Mag	Ban1	0.87	807.30
T17-515	T17	MLM-09	Massive Mag	Ban1	1.05	834.17
T17-516	T17	MLM-09	Massive Mag	Ban1	0.88	809.43
T17-517	T17	MLM-09	Massive Mag	Ban1	1.02	830.00
T17-518	T17	MLM-09	Massive Mag	Ban1	0.84	801.71
T17-519	T17	MLM-09	Massive Mag	Ban1	1.10	841.19
T17-520	T17	MLM-09	Massive Mag	Ban1	1.93	931.93
T17-521	T17	MLM-09	Massive Mag	Ban1	0.87	807.49
T17-524	T17	MLM-09	Massive Mag	Ban1	0.82	798.55
T17-525	T17	MLM-09	Massive Mag	Ban1	0.81	797.63
T17-526	T17	MLM-09	Massive Mag	Ban1	0.84	802.66
T17-527	T17	MLM-09	Massive Mag	Ban1	0.83	800.40
T17-528	T17	MLM-09	Massive Mag	Ban1	0.83	800.27
T17-529	T17	MLM-09	Massive Mag	Ban1	0.82	799.38
T17-530	T17	MLM-09	Massive Mag	Ban1	0.82	799.37
T17-531	T17	MLM-09	Massive Mag	Ban1	0.82	798.59
T17-532	T17	MLM-09	Massive Mag	Ban1	0.82	799.30
T17-533	T17	MLM-09	Massive Mag	Ban1	0.82	798.58
T17-534	T17	MLM-09	Massive Mag	Ban1	0.82	798.29
T17-535	T17	MLM-09	Massive Mag	Ban1	0.84	801.72
T17-536	T17	MLM-09	Massive Mag	Ban1	0.83	801.04
T17-537	T17	MLM-09	Massive Mag	Ban1	0.81	796.61
T17-538	T17	MLM-09	Massive Mag	Ban1	0.93	817.17
T17-539	T17	MLM-09	Massive Mag	Ban1	0.82	799.16
T17-540	T17	MLM-09	Massive Mag	Ban1	0.88	808.44
T17-541	T17	MLM-09	Massive Mag	Ban1	0.84	801.92
T17-542	T17	MLM-09	Massive Mag	Ban1	0.88	808.51
T17-543	T17	MLM-09	Massive Mag	Ban1	0.84	802.84
T17-544	T17	MLM-09	Massive Mag	Ban1	0.86	805.81
T17-545	T17	MLM-09	Massive Mag	Ban1	1.14	846.06
T17-546	T17	MLM-09	Massive Mag	Ban1	0.83	800.55
T17-547	T17	MLM-09	Massive Mag	Ban1	1.02	829.61
T17-548	T17	MLM-09	Massive Mag	Ban1	0.94	817.84
T17-549	T17	MLM-09	Massive Mag	Ban1	0.87	806.51
T17-550	T17	MLM-09	Massive Mag	Ban1	0.87	807.54
1221	T4	MLZ-09	Act-Px-Mag Veins	Exs1 + Exs2 + Ban1	1.06	840.82
1222	T4	MLZ-09	Act-Px-Mag Veins	Exs1 + Exs2 + Ban1	1.17	856.37
1223	T4	MLZ-09	Act-Px-Mag Veins	Exs1 + Exs2 + Ban1	1.21	861.83
1224	T4	MLZ-09	Act-Px-Mag Veins	Exs1 + Exs2 + Ban1	1.26	867.33
1225	T4	MLZ-09	Act-Px-Mag Veins	Exs1 + Exs2 + Ban1	1.40	885.93
1226	T4	MLZ-09	Act-Px-Mag Veins	Exs1 + Exs2 + Ban1	1.21	861.52
1227	T4	MLZ-09	Act-Px-Mag Veins	Exs1 + Exs2 + Ban1	1.20	859.81
1228	T4	MLZ-09	Act-Px-Mag Veins	Exs1 + Exs2 + Ban1	1.31	873.96
1230	T4	MLZ-09	Act-Px-Mag Veins	Exs1 + Exs2 + Ban1	1.56	905.00

ID	Transect	Sample	Mineralization Style	Texture	Mg [wt. %]	T°mean
1231	T4	MLZ-09	Act-Px-Mag Veins	Exs1 + Exs2 + Ban1	1.20	859.62
1232	T4	MLZ-09	Act-Px-Mag Veins	Exs1 + Exs2 + Ban1	1.31	874.81
1233	T4	MLZ-09	Act-Px-Mag Veins	Exs1 + Exs2 + Ban1	1.24	865.35
1234	T4	MLZ-09	Act-Px-Mag Veins	Exs1 + Exs2 + Ban1	1.16	856.80
1237	T4	MLZ-09	Act-Px-Mag Veins	Exs1 + Exs2 + Ban1	1.53	899.68
1238	T4	MLZ-09	Act-Px-Mag Veins	Exs1 + Exs2 + Ban1	0.93	820.62
1239	T4	MLZ-09	Act-Px-Mag Veins	Exs1 + Exs2 + Ban1	0.99	830.70
1240	T4	MLZ-09	Act-Px-Mag Veins	Exs1 + Exs2 + Ban1	1.38	882.79
1242	T4	MLZ-09	Act-Px-Mag Veins	Exs1 + Exs2 + Ban1	1.23	863.94
1243	T4	MLZ-09	Act-Px-Mag Veins	Exs1 + Exs2 + Ban1	1.37	884.13
1245	T4	MLZ-09	Act-Px-Mag Veins	Exs1 + Exs2 + Ban1	0.94	822.27
1246	T4	MLZ-09	Act-Px-Mag Veins	Exs1 + Exs2 + Ban1	1.27	871.83
1247	T4	MLZ-09	Act-Px-Mag Veins	Exs1 + Exs2 + Ban1	0.99	829.94
1248	T4	MLZ-09	Act-Px-Mag Veins	Exs1 + Exs2 + Ban1	0.96	825.43
1249	T4	MLZ-09	Act-Px-Mag Veins	Exs1 + Exs2 + Ban1	0.89	814.93
1251	T4	MLZ-09	Act-Px-Mag Veins	Exs1 + Exs2 + Ban1	1.21	860.80
1252	T4	MLZ-09	Act-Px-Mag Veins	Exs1 + Exs2 + Ban1	1.29	871.69
1253	T4	MLZ-09	Act-Px-Mag Veins	Exs1 + Exs2 + Ban1	1.11	846.86
1254	T4	MLZ-09	Act-Px-Mag Veins	Exs1 + Exs2 + Ban1	1.12	849.55
1255	T4	MLZ-09	Act-Px-Mag Veins	Exs1 + Exs2 + Ban1	0.94	822.86
1256	T4	MLZ-09	Act-Px-Mag Veins	Exs1 + Exs2 + Ban1	1.16	856.58
1258	T4	MLZ-09	Act-Px-Mag Veins	Exs1 + Exs2 + Ban1	0.84	806.16
1259	T4	MLZ-09	Act-Px-Mag Veins	Exs1 + Exs2 + Ban1	0.93	820.32
1260	T4	MLZ-09	Act-Px-Mag Veins	Exs1 + Exs2 + Ban1	0.93	819.99
1261	T4	MLZ-09	Act-Px-Mag Veins	Exs1 + Exs2 + Ban1	1.08	843.48
1262	T4	MLZ-09	Act-Px-Mag Veins	Exs1 + Exs2 + Ban1	1.04	837.37
1263	T4	MLZ-09	Act-Px-Mag Veins	Exs1 + Exs2 + Ban1	1.41	886.62
1264	T4	MLZ-09	Act-Px-Mag Veins	Exs1 + Exs2 + Ban1	1.01	833.04
1267	T4	MLZ-09	Act-Px-Mag Veins	Exs1 + Exs2 + Ban1	0.90	816.85
1268	T4	MLZ-09	Act-Px-Mag Veins	Exs1 + Exs2 + Ban1	0.93	820.86
1269	T4	MLZ-09	Act-Px-Mag Veins	Exs1 + Exs2 + Ban1	1.07	844.33
1270	T4	MLZ-09	Act-Px-Mag Veins	Exs1 + Exs2 + Ban1	1.10	845.59
1286	T4B	MLZ-09	Act-Px-Mag Veins	Exs1 + Exs2 + Ban1	0.99	830.35
1287	T4B	MLZ-09	Act-Px-Mag Veins	Exs1 + Exs2 + Ban1	1.30	872.58
1288	T4B	MLZ-09	Act-Px-Mag Veins	Exs1 + Exs2 + Ban1	1.37	880.36
1291	T4B	MLZ-09	Act-Px-Mag Veins	Exs1 + Exs2 + Ban1	0.93	821.18
1292	T4B	MLZ-09	Act-Px-Mag Veins	Exs1 + Exs2 + Ban1	1.41	886.06
1294	T4B	MLZ-09	Act-Px-Mag Veins	Exs1 + Exs2 + Ban1	0.90	816.41
1295	T4B	MLZ-09	Act-Px-Mag Veins	Exs1 + Exs2 + Ban1	0.94	822.33
1296	T4B	MLZ-09	Act-Px-Mag Veins	Exs1 + Exs2 + Ban1	0.88	812.80
1297	T4B	MLZ-09	Act-Px-Mag Veins	Exs1 + Exs2 + Ban1	0.94	823.40
1298	T4B	MLZ-09	Act-Px-Mag Veins	Exs1 + Exs2 + Ban1	0.88	811.92
1299	T4B	MLZ-09	Act-Px-Mag Veins	Exs1 + Exs2 + Ban1	0.88	812.91
1300	T4B	MLZ-09	Act-Px-Mag Veins	Exs1 + Exs2 + Ban1	0.97	826.59
1303	T4B	MLZ-09	Act-Px-Mag Veins	Exs1 + Exs2 + Ban1	0.97	825.98
1304	T4B	MLZ-09	Act-Px-Mag Veins	Exs1 + Exs2 + Ban1	0.92	818.87
1306	T4B	MLZ-09	Act-Px-Mag Veins	Exs1 + Exs2 + Ban1	0.88	812.36
1307	T4B	MLZ-09	Act-Px-Mag Veins	Exs1 + Exs2 + Ban1	0.91	818.23
1308	T4B	MLZ-09	Act-Px-Mag Veins	Exs1 + Exs2 + Ban1	0.86	809.32

ID	Transect	Sample	Mineralization Style	Texture	Mg [wt. %]	T°mean
1309	T4B	MLZ-09	Act-Px-Mag Veins	Exs1 + Exs2 + Ban1	0.91	818.00
1310	T4B	MLZ-09	Act-Px-Mag Veins	Exs1 + Exs2 + Ban1	1.39	886.24
1311	T4B	MLZ-09	Act-Px-Mag Veins	Exs1 + Exs2 + Ban1	0.87	810.63
1312	T4B	MLZ-09	Act-Px-Mag Veins	Exs1 + Exs2 + Ban1	0.94	823.03
1313	T4B	MLZ-09	Act-Px-Mag Veins	Exs1 + Exs2 + Ban1	0.95	823.78
T18-551	T18	MLM-01	Act-Px-Mag Veins	Ban1	0.97	825.29
T18-552	T18	MLM-01	Act-Px-Mag Veins	Ban1	0.85	806.02
T18-553	T18	MLM-01	Act-Px-Mag Veins	Ban1	0.72	782.95
T18-554	T18	MLM-01	Act-Px-Mag Veins	Ban1	0.93	818.13
T18-555	T18	MLM-01	Act-Px-Mag Veins	Ban1	0.70	778.25
T18-556	T18	MLM-01	Act-Px-Mag Veins	Ban1	0.61	761.45
T18-557	T18	MLM-01	Act-Px-Mag Veins	Ban1	0.71	781.37
T18-558	T18	MLM-01	Act-Px-Mag Veins	Ban1	0.71	780.66
T18-559	T18	MLM-01	Act-Px-Mag Veins	Ban1	0.67	773.67
T18-560	T18	MLM-01	Act-Px-Mag Veins	Ban1	0.73	785.65
T18-561	T18	MLM-01	Act-Px-Mag Veins	Ban1	0.69	778.01
T18-562	T18	MLM-01	Act-Px-Mag Veins	Ban1	0.68	775.65
T18-563	T18	MLM-01	Act-Px-Mag Veins	Ban1	0.56	750.09
T18-564	T18	MLM-01	Act-Px-Mag Veins	Ban1	0.37	699.69
T18-565	T18	MLM-01	Act-Px-Mag Veins	Ban1	0.63	766.06
T18-566	T18	MLM-01	Act-Px-Mag Veins	Ban1	0.25	660.19
T18-567	T18	MLM-01	Act-Px-Mag Veins	Ban1	0.54	747.25
T18-568	T18	MLM-01	Act-Px-Mag Veins	Ban1	0.84	805.24
T18-569	T18	MLM-01	Act-Px-Mag Veins	Ban1	0.66	771.79
T18-570	T18	MLM-01	Act-Px-Mag Veins	Ban1	0.70	778.46
T18-571	T18	MLM-01	Act-Px-Mag Veins	Ban1	0.70	780.14
T18-572	T18	MLM-01	Act-Px-Mag Veins	Ban1	0.71	781.42
T18-573	T18	MLM-01	Act-Px-Mag Veins	Ban1	0.66	771.92
T18-574	T18	MLM-01	Act-Px-Mag Veins	Ban1	0.69	777.76
T18-575	T18	MLM-01	Act-Px-Mag Veins	Ban1	0.75	789.52
T18-576	T18	MLM-01	Act-Px-Mag Veins	Ban1	1.16	853.62
T18-577	T18	MLM-01	Act-Px-Mag Veins	Ban1	0.65	768.52
T18-578	T18	MLM-01	Act-Px-Mag Veins	Ban1	0.72	781.84
T18-579	T18	MLM-01	Act-Px-Mag Veins	Ban1	0.67	773.15
T18-580	T18	MLM-01	Act-Px-Mag Veins	Ban1	0.67	773.78
T18-581	T18	MLM-01	Act-Px-Mag Veins	Ban1	0.67	774.08
T18-582	T18	MLM-01	Act-Px-Mag Veins	Ban1	0.65	769.95
T18-583	T18	MLM-01	Act-Px-Mag Veins	Ban1	0.70	778.68
T18-584	T18	MLM-01	Act-Px-Mag Veins	Ban1	0.79	794.76
T18-585	T18	MLM-01	Act-Px-Mag Veins	Ban1	0.69	777.55
T18-586	T18	MLM-01	Act-Px-Mag Veins	Ban1	0.73	785.46
T18-587	T18	MLM-01	Act-Px-Mag Veins	Ban1	0.70	779.01
T18-588	T18	MLM-01	Act-Px-Mag Veins	Ban1	0.66	771.81
T18-589	T18	MLM-01	Act-Px-Mag Veins	Ban1	0.67	773.90
T18-590	T18	MLM-01	Act-Px-Mag Veins	Ban1	0.66	772.07
T18-591	T18	MLM-01	Act-Px-Mag Veins	Ban1	0.71	781.76
T18-592	T18	MLM-01	Act-Px-Mag Veins	Ban1	0.76	791.03
T18-593	T18	MLM-01	Act-Px-Mag Veins	Ban1	0.69	776.33
T18-594	T18	MLM-01	Act-Px-Mag Veins	Ban1	0.73	784.81

ID	Transect	Sample	Mineralization Style	Texture	Mg [wt. %]	T°mean
T18-595	T18	MLM-01	Act-Px-Mag Veins	Ban1	0.70	779.02
T18-596	T18	MLM-01	Act-Px-Mag Veins	Ban1	0.69	777.81
T18-597	T18	MLM-01	Act-Px-Mag Veins	Ban1	1.04	835.07
T18-598	T18	MLM-01	Act-Px-Mag Veins	Ban1	0.70	778.61
T18-599	T18	MLM-01	Act-Px-Mag Veins	Ban1	0.72	782.35
T18-600	T18	MLM-01	Act-Px-Mag Veins	Ban1	0.70	778.35
T19-601	T19	MLM-01	Act-Px-Mag Veins	Ban1 + Incl	0.72	783.30
T19-602	T19	MLM-01	Act-Px-Mag Veins	Ban1 + Incl	0.70	779.36
T19-603	T19	MLM-01	Act-Px-Mag Veins	Ban1 + Incl	0.80	797.17
T19-604	T19	MLM-01	Act-Px-Mag Veins	Ban1 + Incl	0.74	785.93
T19-605	T19	MLM-01	Act-Px-Mag Veins	Ban1 + Incl	0.70	779.34
T19-606	T19	MLM-01	Act-Px-Mag Veins	Ban1 + Incl	0.79	796.07
T19-607	T19	MLM-01	Act-Px-Mag Veins	Ban1 + Incl	0.90	815.05
T19-608	T19	MLM-01	Act-Px-Mag Veins	Ban1 + Incl	0.68	776.08
T19-609	T19	MLM-01	Act-Px-Mag Veins	Ban1 + Incl	0.78	794.37
T19-610	T19	MLM-01	Act-Px-Mag Veins	Ban1 + Incl	0.85	805.71
T19-611	T19	MLM-01	Act-Px-Mag Veins	Ban1 + Incl	0.71	780.28
T19-612	T19	MLM-01	Act-Px-Mag Veins	Ban1 + Incl	1.11	846.67
T19-613	T19	MLM-01	Act-Px-Mag Veins	Ban1 + Incl	0.90	815.13
T19-614	T19	MLM-01	Act-Px-Mag Veins	Ban1 + Incl	0.80	797.24
T19-616	T19	MLM-01	Act-Px-Mag Veins	Ban1 + Incl	0.67	772.98
T19-617	T19	MLM-01	Act-Px-Mag Veins	Ban1 + Incl	0.95	820.84
T19-618	T19	MLM-01	Act-Px-Mag Veins	Ban1 + Incl	0.96	824.29
T19-619	T19	MLM-01	Act-Px-Mag Veins	Ban1 + Incl	0.77	791.45
T19-620	T19	MLM-01	Act-Px-Mag Veins	Ban1 + Incl	0.66	771.05
T19-621	T19	MLM-01	Act-Px-Mag Veins	Ban1 + Incl	0.86	807.42
T19-622	T19	MLM-01	Act-Px-Mag Veins	Ban1 + Incl	0.81	799.44
T19-623	T19	MLM-01	Act-Px-Mag Veins	Ban1 + Incl	0.72	783.45
T19-624	T19	MLM-01	Act-Px-Mag Veins	Ban1 + Incl	0.68	775.27
T19-625	T19	MLM-01	Act-Px-Mag Veins	Ban1 + Incl	0.89	813.07
T19-628	T19	MLM-01	Act-Px-Mag Veins	Ban1 + Incl	0.70	780.29
T19-629	T19	MLM-01	Act-Px-Mag Veins	Ban1 + Incl	0.91	815.91
T19-630	T19	MLM-01	Act-Px-Mag Veins	Ban1 + Incl	0.63	764.73
T19-632	T19	MLM-01	Act-Px-Mag Veins	Ban1 + Incl	0.69	776.65
T19-633	T19	MLM-01	Act-Px-Mag Veins	Ban1 + Incl	0.95	823.97
T19-634	T19	MLM-01	Act-Px-Mag Veins	Ban1 + Incl	0.62	763.38
T19-636	T19	MLM-01	Act-Px-Mag Veins	Ban1 + Incl	0.58	756.19
T19-637	T19	MLM-01	Act-Px-Mag Veins	Ban1 + Incl	0.61	760.90
T19-639	T19	MLM-01	Act-Px-Mag Veins	Ban1 + Incl	0.66	772.60
T19-640	T19	MLM-01	Act-Px-Mag Veins	Ban1 + Incl	0.61	760.55
T19-641	T19	MLM-01	Act-Px-Mag Veins	Ban1 + Incl	0.65	768.98
T19-642	T19	MLM-01	Act-Px-Mag Veins	Ban1 + Incl	0.63	766.42
T19-643	T19	MLM-01	Act-Px-Mag Veins	Ban1 + Incl	0.64	768.11
T19-644	T19	MLM-01	Act-Px-Mag Veins	Ban1 + Incl	0.65	769.32
T19-645	T19	MLM-01	Act-Px-Mag Veins	Ban1 + Incl	0.64	767.95
T19-646	T19	MLM-01	Act-Px-Mag Veins	Ban1 + Incl	0.70	779.30
T19-647	T19	MLM-01	Act-Px-Mag Veins	Ban1 + Incl	0.69	776.86
T19-649	T19	MLM-01	Act-Px-Mag Veins	Ban1 + Incl	0.78	794.28
T19-652	T19	MLM-01	Act-Px-Mag Veins	Ban1 + Incl	0.67	774.16

ID	Transect	Sample	Mineralization Style	Texture	Mg [wt. %]	T°mean
T19-653	T19	MLM-01	Act-Px-Mag Veins	Ban1 + Incl	0.69	778.00
T19-654	T19	MLM-01	Act-Px-Mag Veins	Ban1 + Incl	0.72	782.57
T19-655	T19	MLM-01	Act-Px-Mag Veins	Ban1 + Incl	0.66	771.77
T19-656	T19	MLM-01	Act-Px-Mag Veins	Ban1 + Incl	0.69	777.88
T19-657	T19	MLM-01	Act-Px-Mag Veins	Ban1 + Incl	0.65	769.96
T19-659	T19	MLM-01	Act-Px-Mag Veins	Ban1 + Incl	0.68	774.75
T19-660	T19	MLM-01	Act-Px-Mag Veins	Ban1 + Incl	0.67	773.55
T20-661	T20	MLM-01	Act-Px-Mag Veins	Ban1	1.22	860.45
T20-662	T20	MLM-01	Act-Px-Mag Veins	Ban1	0.81	799.62
T20-664	T20	MLM-01	Act-Px-Mag Veins	Ban1	0.83	803.52
T20-665	T20	MLM-01	Act-Px-Mag Veins	Ban1	0.99	829.80
T20-666	T20	MLM-01	Act-Px-Mag Veins	Ban1	0.94	819.78
T20-667	T20	MLM-01	Act-Px-Mag Veins	Ban1	0.82	801.26
T20-669	T20	MLM-01	Act-Px-Mag Veins	Ban1	0.83	802.35
T20-670	T20	MLM-01	Act-Px-Mag Veins	Ban1	0.88	810.78
T20-671	T20	MLM-01	Act-Px-Mag Veins	Ban1	0.78	793.47
T20-672	T20	MLM-01	Act-Px-Mag Veins	Ban1	0.75	788.19
T20-673	T20	MLM-01	Act-Px-Mag Veins	Ban1	0.81	799.70
T20-674	T20	MLM-01	Act-Px-Mag Veins	Ban1	1.70	920.34
T20-675	T20	MLM-01	Act-Px-Mag Veins	Ban1	1.11	845.85
T20-676	T20	MLM-01	Act-Px-Mag Veins	Ban1	0.84	804.82
T20-677	T20	MLM-01	Act-Px-Mag Veins	Ban1	1.17	854.99
T20-678	T20	MLM-01	Act-Px-Mag Veins	Ban1	0.79	795.61
T20-679	T20	MLM-01	Act-Px-Mag Veins	Ban1	0.78	793.35
T20-680	T20	MLM-01	Act-Px-Mag Veins	Ban1	1.09	844.00
T20-681	T20	MLM-01	Act-Px-Mag Veins	Ban1	1.15	851.21
T20-682	T20	MLM-01	Act-Px-Mag Veins	Ban1	1.16	854.63
T20-683	T20	MLM-01	Act-Px-Mag Veins	Ban1	0.90	813.90
T20-684	T20	MLM-01	Act-Px-Mag Veins	Ban1	0.81	798.62
T20-685	T20	MLM-01	Act-Px-Mag Veins	Ban1	0.82	800.16
T20-686	T20	MLM-01	Act-Px-Mag Veins	Ban1	0.82	800.61
T20-687	T20	MLM-01	Act-Px-Mag Veins	Ban1	0.80	797.69
T20-688	T20	MLM-01	Act-Px-Mag Veins	Ban1	0.85	805.24
T20-690	T20	MLM-01	Act-Px-Mag Veins	Ban1	0.82	802.28
T20-691	T20	MLM-01	Act-Px-Mag Veins	Ban1	0.91	815.30
T20-692	T20	MLM-01	Act-Px-Mag Veins	Ban1	0.76	791.28
T20-693	T20	MLM-01	Act-Px-Mag Veins	Ban1	0.70	779.62
T20-694	T20	MLM-01	Act-Px-Mag Veins	Ban1	0.77	792.41
T20-695	T20	MLM-01	Act-Px-Mag Veins	Ban1	0.96	823.84
T20-696	T20	MLM-01	Act-Px-Mag Veins	Ban1	0.80	797.17
T20-697	T20	MLM-01	Act-Px-Mag Veins	Ban1	0.79	796.19
T20-698	T20	MLM-01	Act-Px-Mag Veins	Ban1	0.82	801.33
T20-699	T20	MLM-01	Act-Px-Mag Veins	Ban1	0.80	796.56
T20-700	T20	MLM-01	Act-Px-Mag Veins	Ban1	0.80	797.32
T20-701	T20	MLM-01	Act-Px-Mag Veins	Ban1	0.81	798.20
T20-702	T20	MLM-01	Act-Px-Mag Veins	Ban1	0.80	796.86
T20-703	T20	MLM-01	Act-Px-Mag Veins	Ban1	0.78	794.38
T20-704	T20	MLM-01	Act-Px-Mag Veins	Ban1	0.80	797.55
T20-705	T20	MLM-01	Act-Px-Mag Veins	Ban1	0.82	801.14

ID	Transect	Sample	Mineralization Style	Texture	Mg [wt. %]	T°mean
T20-706	T20	MLM-01	Act-Px-Mag Veins	Ban1	0.81	798.48
T20-707	T20	MLM-01	Act-Px-Mag Veins	Ban1	0.81	799.00
T20-708	T20	MLM-01	Act-Px-Mag Veins	Ban1	0.83	802.73
T20-709	T20	MLM-01	Act-Px-Mag Veins	Ban1	0.83	802.99
T20-710	T20	MLM-01	Act-Px-Mag Veins	Ban1	0.82	801.33
T12-251	T12	MLM-02	Hydro Breccia	Exs1 + Por	0.15	606.91
T12-252	T12	MLM-02	Hydro Breccia	Exs1 + Por	0.16	612.92
T12-253	T12	MLM-02	Hydro Breccia	Exs1 + Por	0.18	623.08
T12-254	T12	MLM-02	Hydro Breccia	Exs1 + Por	0.17	622.96
T12-255	T12	MLM-02	Hydro Breccia	Exs1 + Por	0.17	618.62
T12-256	T12	MLM-02	Hydro Breccia	Exs1 + Por	0.15	608.59
T12-257	T12	MLM-02	Hydro Breccia	Exs1 + Por	0.14	604.57
T12-258	T12	MLM-02	Hydro Breccia	Exs1 + Por	0.37	701.97
T12-259	T12	MLM-02	Hydro Breccia	Exs1 + Por	0.18	624.48
T12-260	T12	MLM-02	Hydro Breccia	Exs1 + Por	0.17	622.06
T12-261	T12	MLM-02	Hydro Breccia	Exs1 + Por	0.15	610.11
T12-262	T12	MLM-02	Hydro Breccia	Exs1 + Por	0.16	613.14
T12-263	T12	MLM-02	Hydro Breccia	Exs1 + Por	0.55	763.44
T12-264	T12	MLM-02	Hydro Breccia	Exs1 + Por	0.15	610.46
T12-265	T12	MLM-02	Hydro Breccia	Exs1 + Por	0.12	592.99
T12-266	T12	MLM-02	Hydro Breccia	Exs1 + Por	0.14	603.78
T12-267	T12	MLM-02	Hydro Breccia	Exs1 + Por	0.13	596.88
T12-268	T12	MLM-02	Hydro Breccia	Exs1 + Por	0.14	601.75
T12-269	T12	MLM-02	Hydro Breccia	Exs1 + Por	0.12	590.60
T12-270	T12	MLM-02	Hydro Breccia	Exs1 + Por	0.10	573.23
T12-271	T12	MLM-02	Hydro Breccia	Exs1 + Por	0.14	603.61
T12-272	T12	MLM-02	Hydro Breccia	Exs1 + Por	0.20	635.30
T12-273	T12	MLM-02	Hydro Breccia	Exs1 + Por	0.13	591.92
T12-274	T12	MLM-02	Hydro Breccia	Exs1 + Por	0.13	595.19
T12-275	T12	MLM-02	Hydro Breccia	Exs1 + Por	0.11	577.43
T12-276	T12	MLM-02	Hydro Breccia	Exs1 + Por	0.11	579.23
T12-277	T12	MLM-02	Hydro Breccia	Exs1 + Por	0.25	666.49
T12-278	T12	MLM-02	Hydro Breccia	Exs1 + Por	0.11	577.06
T12-279	T12	MLM-02	Hydro Breccia	Exs1 + Por	0.11	581.34
T12-280	T12	MLM-02	Hydro Breccia	Exs1 + Por	0.12	587.66
T12-281	T12	MLM-02	Hydro Breccia	Exs1 + Por	0.12	585.23
T12-282	T12	MLM-02	Hydro Breccia	Exs1 + Por	0.11	577.49
T12-283	T12	MLM-02	Hydro Breccia	Exs1 + Por	0.10	572.60
T12-284	T12	MLM-02	Hydro Breccia	Exs1 + Por	0.09	559.31
T12-285	T12	MLM-02	Hydro Breccia	Exs1 + Por	0.09	565.64
T12-286	T12	MLM-02	Hydro Breccia	Exs1 + Por	0.51	753.59
T12-287	T12	MLM-02	Hydro Breccia	Exs1 + Por	0.07	546.05
T12-288	T12	MLM-02	Hydro Breccia	Exs1 + Por	0.09	559.50
T12-290	T12	MLM-02	Hydro Breccia	Exs1 + Por	0.06	528.23
T13-291	T13	MLM-02	Hydro Breccia	Exs1 + Por	0.14	603.78
T13-292	T13	MLM-02	Hydro Breccia	Exs1 + Por	0.15	609.08
T13-293	T13	MLM-02	Hydro Breccia	Exs1 + Por	0.16	613.21
T13-294	T13	MLM-02	Hydro Breccia	Exs1 + Por	0.16	613.18
T13-295	T13	MLM-02	Hydro Breccia	Exs1 + Por	0.20	638.06

ID	Transect	Sample	Mineralization Style	Texture	Mg [wt. %]	T°mean
T13-296	T13	MLM-02	Hydro Breccia	Exs1 + Por	0.15	605.70
T13-297	T13	MLM-02	Hydro Breccia	Exs1 + Por	0.12	590.03
T13-298	T13	MLM-02	Hydro Breccia	Exs1 + Por	0.14	603.52
T13-299	T13	MLM-02	Hydro Breccia	Exs1 + Por	0.15	605.27
T13-300	T13	MLM-02	Hydro Breccia	Exs1 + Por	0.15	605.95
T13-301	T13	MLM-02	Hydro Breccia	Exs1 + Por	0.16	612.63
T13-302	T13	MLM-02	Hydro Breccia	Exs1 + Por	0.15	609.55
T13-303	T13	MLM-02	Hydro Breccia	Exs1 + Por	0.15	607.63
T13-304	T13	MLM-02	Hydro Breccia	Exs1 + Por	0.15	607.53
T13-305	T13	MLM-02	Hydro Breccia	Exs1 + Por	0.15	606.66
T13-306	T13	MLM-02	Hydro Breccia	Exs1 + Por	0.16	611.66
T13-307	T13	MLM-02	Hydro Breccia	Exs1 + Por	0.15	606.51
T13-308	T13	MLM-02	Hydro Breccia	Exs1 + Por	0.15	606.62
T13-309	T13	MLM-02	Hydro Breccia	Exs1 + Por	0.14	604.99
T13-310	T13	MLM-02	Hydro Breccia	Exs1 + Por	0.15	608.30
T13-311	T13	MLM-02	Hydro Breccia	Exs1 + Por	0.14	601.29
T13-312	T13	MLM-02	Hydro Breccia	Exs1 + Por	0.14	602.51
T13-313	T13	MLM-02	Hydro Breccia	Exs1 + Por	0.13	593.74
T13-314	T13	MLM-02	Hydro Breccia	Exs1 + Por	0.14	602.93
T13-315	T13	MLM-02	Hydro Breccia	Exs1 + Por	0.14	605.20
T13-316	T13	MLM-02	Hydro Breccia	Exs1 + Por	0.14	602.69
T13-317	T13	MLM-02	Hydro Breccia	Exs1 + Por	0.15	605.41
T13-318	T13	MLM-02	Hydro Breccia	Exs1 + Por	0.14	604.15
T13-319	T13	MLM-02	Hydro Breccia	Exs1 + Por	0.14	601.33
T13-320	T13	MLM-02	Hydro Breccia	Exs1 + Por	0.14	602.06
T21-711	T21	MLM-05	Hydro Breccia	Exs1 + Ban1	0.34	693.32
T21-713	T21	MLM-05	Hydro Breccia	Exs1 + Ban1	0.28	670.70
T21-714	T21	MLM-05	Hydro Breccia	Exs1 + Ban1	0.32	684.39
T21-715	T21	MLM-05	Hydro Breccia	Exs1 + Ban1	0.25	657.60
T21-716	T21	MLM-05	Hydro Breccia	Exs1 + Ban1	0.32	686.79
T21-717	T21	MLM-05	Hydro Breccia	Exs1 + Ban1	0.37	703.15
T21-718	T21	MLM-05	Hydro Breccia	Exs1 + Ban1	0.37	701.65
T21-719	T21	MLM-05	Hydro Breccia	Exs1 + Ban1	0.34	691.92
T21-720	T21	MLM-05	Hydro Breccia	Exs1 + Ban1	0.34	691.75
T21-721	T21	MLM-05	Hydro Breccia	Exs1 + Ban1	0.31	680.68
T21-722	T21	MLM-05	Hydro Breccia	Exs1 + Ban1	0.64	772.50
T21-723	T21	MLM-05	Hydro Breccia	Exs1 + Ban1	0.33	687.52
T21-724	T21	MLM-05	Hydro Breccia	Exs1 + Ban1	0.34	693.36
T21-725	T21	MLM-05	Hydro Breccia	Exs1 + Ban1	0.34	690.82
T21-726	T21	MLM-05	Hydro Breccia	Exs1 + Ban1	0.28	671.90
T21-727	T21	MLM-05	Hydro Breccia	Exs1 + Ban1	0.35	696.15
T21-728	T21	MLM-05	Hydro Breccia	Exs1 + Ban1	0.33	688.92
T21-729	T21	MLM-05	Hydro Breccia	Exs1 + Ban1	0.33	688.09
T21-730	T21	MLM-05	Hydro Breccia	Exs1 + Ban1	0.45	726.02
T21-731	T21	MLM-05	Hydro Breccia	Exs1 + Ban1	0.35	694.94
T21-732	T21	MLM-05	Hydro Breccia	Exs1 + Ban1	0.34	691.93
T21-733	T21	MLM-05	Hydro Breccia	Exs1 + Ban1	0.75	791.38
T21-734	T21	MLM-05	Hydro Breccia	Exs1 + Ban1	0.38	703.74
T21-735	T21	MLM-05	Hydro Breccia	Exs1 + Ban1	0.52	741.93

ID	Transect	Sample	Mineralization Style	Texture	Mg [wt. %]	T°mean
T21-736	T21	MLM-05	Hydro Breccia	Exs1 + Ban1	0.34	691.98
T21-738	T21	MLM-05	Hydro Breccia	Exs1 + Ban1	0.33	686.83
T21-739	T21	MLM-05	Hydro Breccia	Exs1 + Ban1	0.34	691.21
T21-740	T21	MLM-05	Hydro Breccia	Exs1 + Ban1	0.34	691.58
T21-741	T21	MLM-05	Hydro Breccia	Exs1 + Ban1	0.33	689.19
T21-742	T21	MLM-05	Hydro Breccia	Exs1 + Ban1	0.33	689.84
T21-743	T21	MLM-05	Hydro Breccia	Exs1 + Ban1	0.75	795.83
T21-744	T21	MLM-05	Hydro Breccia	Exs1 + Ban1	0.35	696.34
T21-745	T21	MLM-05	Hydro Breccia	Exs1 + Ban1	0.41	712.64
T21-746	T21	MLM-05	Hydro Breccia	Exs1 + Ban1	0.36	697.36
T21-749	T21	MLM-05	Hydro Breccia	Exs1 + Ban1	0.46	728.89
T21-750	T21	MLM-05	Hydro Breccia	Exs1 + Ban1	0.56	754.81
T21-751	T21	MLM-05	Hydro Breccia	Exs1 + Ban1	0.34	690.72
T21-752	T21	MLM-05	Hydro Breccia	Exs1 + Ban1	0.34	691.56
T21-753	T21	MLM-05	Hydro Breccia	Exs1 + Ban1	0.92	821.80
T21-754	T21	MLM-05	Hydro Breccia	Exs1 + Ban1	0.12	586.74
T21-755	T21	MLM-05	Hydro Breccia	Exs1 + Ban1	1.01	833.68
T21-756	T21	MLM-05	Hydro Breccia	Exs1 + Ban1	0.54	748.34
T21-757	T21	MLM-05	Hydro Breccia	Exs1 + Ban1	0.46	729.41
T21-758	T21	MLM-05	Hydro Breccia	Exs1 + Ban1	0.47	732.78
T21-759	T21	MLM-05	Hydro Breccia	Exs1 + Ban1	0.44	723.93
T21-760	T21	MLM-05	Hydro Breccia	Exs1 + Ban1	0.67	782.53
T21-761	T21	MLM-05	Hydro Breccia	Exs1 + Ban1	0.41	714.77
T21-762	T21	MLM-05	Hydro Breccia	Exs1 + Ban1	0.45	726.21
T21-763	T21	MLM-05	Hydro Breccia	Exs1 + Ban1	0.54	749.14
T21-764	T21	MLM-05	Hydro Breccia	Exs1 + Ban1	0.57	757.24
T21-766	T21	MLM-05	Hydro Breccia	Exs1 + Ban1	0.72	786.88
T21-767	T21	MLM-05	Hydro Breccia	Exs1 + Ban1	0.48	734.54
T21-768	T21	MLM-05	Hydro Breccia	Exs1 + Ban1	0.68	779.05
T21-769	T21	MLM-05	Hydro Breccia	Exs1 + Ban1	0.41	716.02
T21-770	T21	MLM-05	Hydro Breccia	Exs1 + Ban1	0.53	747.50
T21-771	T21	MLM-05	Hydro Breccia	Exs1 + Ban1	0.47	729.86
T21-772	T21	MLM-05	Hydro Breccia	Exs1 + Ban1	0.69	785.20
T21-773	T21	MLM-05	Hydro Breccia	Exs1 + Ban1	0.33	687.64
T21-774	T21	MLM-05	Hydro Breccia	Exs1 + Ban1	0.38	704.68
T21-776	T21	MLM-05	Hydro Breccia	Exs1 + Ban1	1.19	860.84
T21-778	T21	MLM-05	Hydro Breccia	Exs1 + Ban1	0.32	685.85
T21-779	T21	MLM-05	Hydro Breccia	Exs1 + Ban1	0.30	677.61
T21-780	T21	MLM-05	Hydro Breccia	Exs1 + Ban1	0.29	674.44
T22-781	T22	MLM-05	Hydro Breccia	Exs1 + Por	0.22	645.01
T22-782	T22	MLM-05	Hydro Breccia	Exs1 + Por	0.22	646.38
T22-783	T22	MLM-05	Hydro Breccia	Exs1 + Por	0.24	654.58
T22-784	T22	MLM-05	Hydro Breccia	Exs1 + Por	0.22	646.55
T22-785	T22	MLM-05	Hydro Breccia	Exs1 + Por	0.21	641.27
T22-786	T22	MLM-05	Hydro Breccia	Exs1 + Por	0.21	642.63
T22-787	T22	MLM-05	Hydro Breccia	Exs1 + Por	0.21	639.53
T22-788	T22	MLM-05	Hydro Breccia	Exs1 + Por	0.22	646.56
T22-789	T22	MLM-05	Hydro Breccia	Exs1 + Por	0.23	651.01
T22-790	T22	MLM-05	Hydro Breccia	Exs1 + Por	0.22	644.98

ID	Transect	Sample	Mineralization Style	Texture	Mg [wt. %]	T°mean
T22-791	T22	MLM-05	Hydro Breccia	Exs1 + Por	0.22	644.96
T22-792	T22	MLM-05	Hydro Breccia	Exs1 + Por	0.20	635.22
T22-793	T22	MLM-05	Hydro Breccia	Exs1 + Por	0.26	663.96
T22-794	T22	MLM-05	Hydro Breccia	Exs1 + Por	0.23	648.57
T22-795	T22	MLM-05	Hydro Breccia	Exs1 + Por	0.23	652.72
T22-796	T22	MLM-05	Hydro Breccia	Exs1 + Por	0.22	644.02
T22-797	T22	MLM-05	Hydro Breccia	Exs1 + Por	0.20	635.64
T22-798	T22	MLM-05	Hydro Breccia	Exs1 + Por	0.25	659.47
T22-799	T22	MLM-05	Hydro Breccia	Exs1 + Por	0.21	642.43
T22-800	T22	MLM-05	Hydro Breccia	Exs1 + Por	0.22	644.43
T22-801	T22	MLM-05	Hydro Breccia	Exs1 + Por	0.23	651.44
T22-802	T22	MLM-05	Hydro Breccia	Exs1 + Por	0.22	643.81
T22-803	T22	MLM-05	Hydro Breccia	Exs1 + Por	0.22	645.97
T22-804	T22	MLM-05	Hydro Breccia	Exs1 + Por	0.24	653.11
T22-805	T22	MLM-05	Hydro Breccia	Exs1 + Por	0.20	635.79
T22-807	T22	MLM-05	Hydro Breccia	Exs1 + Por	0.21	641.72
T22-808	T22	MLM-05	Hydro Breccia	Exs1 + Por	0.20	637.41
T22-809	T22	MLM-05	Hydro Breccia	Exs1 + Por	0.33	690.40
T22-810	T22	MLM-05	Hydro Breccia	Exs1 + Por	0.22	645.79
T22-811	T22	MLM-05	Hydro Breccia	Exs1 + Por	0.20	637.48
T22-812	T22	MLM-05	Hydro Breccia	Exs1 + Por	0.20	634.78
T22-813	T22	MLM-05	Hydro Breccia	Exs1 + Por	0.21	642.05
T22-814	T22	MLM-05	Hydro Breccia	Exs1 + Por	0.19	630.76
T22-815	T22	MLM-05	Hydro Breccia	Exs1 + Por	0.21	640.89
T22-816	T22	MLM-05	Hydro Breccia	Exs1 + Por	0.23	651.08
T22-817	T22	MLM-05	Hydro Breccia	Exs1 + Por	0.24	653.94
T22-818	T22	MLM-05	Hydro Breccia	Exs1 + Por	0.20	635.64
T22-820	T22	MLM-05	Hydro Breccia	Exs1 + Por	0.18	624.98
T22-821	T22	MLM-05	Hydro Breccia	Exs1 + Por	0.19	630.28
T22-822	T22	MLM-05	Hydro Breccia	Exs1 + Por	0.27	669.49
T22-823	T22	MLM-05	Hydro Breccia	Exs1 + Por	0.17	619.44
T22-824	T22	MLM-05	Hydro Breccia	Exs1 + Por	0.18	628.00
T22-825	T22	MLM-05	Hydro Breccia	Exs1 + Por	0.18	627.60
T22-826	T22	MLM-05	Hydro Breccia	Exs1 + Por	0.17	622.82
T22-827	T22	MLM-05	Hydro Breccia	Exs1 + Por	0.18	624.07
T22-828	T22	MLM-05	Hydro Breccia	Exs1 + Por	0.17	619.46
T22-829	T22	MLM-05	Hydro Breccia	Exs1 + Por	0.17	619.24
T22-830	T22	MLM-05	Hydro Breccia	Exs1 + Por	0.16	611.88
T22-831	T22	MLM-05	Hydro Breccia	Exs1 + Por	0.18	625.27
T22-832	T22	MLM-05	Hydro Breccia	Exs1 + Por	0.15	606.73
T22-833	T22	MLM-05	Hydro Breccia	Exs1 + Por	0.15	609.31
T22-834	T22	MLM-05	Hydro Breccia	Exs1 + Por	0.14	603.72
T22-835	T22	MLM-05	Hydro Breccia	Exs1 + Por	0.13	597.04
T22-836	T22	MLM-05	Hydro Breccia	Exs1 + Por	0.14	599.30
T22-837	T22	MLM-05	Hydro Breccia	Exs1 + Por	0.12	591.14
T22-838	T22	MLM-05	Hydro Breccia	Exs1 + Por	0.26	666.08
T22-839	T22	MLM-05	Hydro Breccia	Exs1 + Por	0.09	566.79
T22-840	T22	MLM-05	Hydro Breccia	Exs1 + Por	0.08	555.64
T23-841	T23	MLM-05	Hydro Breccia	Exs1 + Ban1	0.12	590.19

ID	Transect	Sample	Mineralization Style	Texture	Mg [wt. %]	T°mean
T23-842	T23	MLM-05	Hydro Breccia	Exs1 + Ban1	0.13	593.96
T23-843	T23	MLM-05	Hydro Breccia	Exs1 + Ban1	0.15	610.58
T23-844	T23	MLM-05	Hydro Breccia	Exs1 + Ban1	0.13	598.53
T23-845	T23	MLM-05	Hydro Breccia	Exs1 + Ban1	0.16	613.09
T23-846	T23	MLM-05	Hydro Breccia	Exs1 + Ban1	0.17	623.17
T23-847	T23	MLM-05	Hydro Breccia	Exs1 + Ban1	0.24	655.20
T23-848	T23	MLM-05	Hydro Breccia	Exs1 + Ban1	0.20	639.25
T23-849	T23	MLM-05	Hydro Breccia	Exs1 + Ban1	0.16	617.04
T23-850	T23	MLM-05	Hydro Breccia	Exs1 + Ban1	0.28	671.83
T23-851	T23	MLM-05	Hydro Breccia	Exs1 + Ban1	0.47	731.67
T23-852	T23	MLM-05	Hydro Breccia	Exs1 + Ban1	0.16	614.50
T23-853	T23	MLM-05	Hydro Breccia	Exs1 + Ban1	0.17	622.37
T23-854	T23	MLM-05	Hydro Breccia	Exs1 + Ban1	0.17	621.75
T23-855	T23	MLM-05	Hydro Breccia	Exs1 + Ban1	0.15	608.77
T23-856	T23	MLM-05	Hydro Breccia	Exs1 + Ban1	0.15	609.95
T23-857	T23	MLM-05	Hydro Breccia	Exs1 + Ban1	0.63	770.00
T23-858	T23	MLM-05	Hydro Breccia	Exs1 + Ban1	0.18	628.12
T23-859	T23	MLM-05	Hydro Breccia	Exs1 + Ban1	0.18	625.99
T23-860	T23	MLM-05	Hydro Breccia	Exs1 + Ban1	0.19	630.79
T23-861	T23	MLM-05	Hydro Breccia	Exs1 + Ban1	0.21	644.93
T23-862	T23	MLM-05	Hydro Breccia	Exs1 + Ban1	0.21	642.42
T23-863	T23	MLM-05	Hydro Breccia	Exs1 + Ban1	0.35	697.75
T23-864	T23	MLM-05	Hydro Breccia	Exs1 + Ban1	0.14	604.63
T23-865	T23	MLM-05	Hydro Breccia	Exs1 + Ban1	0.17	621.20
T23-866	T23	MLM-05	Hydro Breccia	Exs1 + Ban1	0.15	611.39
T23-867	T23	MLM-05	Hydro Breccia	Exs1 + Ban1	0.15	609.89
T23-868	T23	MLM-05	Hydro Breccia	Exs1 + Ban1	0.27	667.05
T23-869	T23	MLM-05	Hydro Breccia	Exs1 + Ban1	0.16	614.43
T23-870	T23	MLM-05	Hydro Breccia	Exs1 + Ban1	0.20	638.29
T23-871	T23	MLM-05	Hydro Breccia	Exs1 + Ban1	0.16	616.38
T23-872	T23	MLM-05	Hydro Breccia	Exs1 + Ban1	0.19	629.22
T23-873	T23	MLM-05	Hydro Breccia	Exs1 + Ban1	0.15	611.29
T23-874	T23	MLM-05	Hydro Breccia	Exs1 + Ban1	0.18	628.26
T23-875	T23	MLM-05	Hydro Breccia	Exs1 + Ban1	0.15	609.45
T23-876	T23	MLM-05	Hydro Breccia	Exs1 + Ban1	0.23	651.78
T23-878	T23	MLM-05	Hydro Breccia	Exs1 + Ban1	0.18	625.27
T23-879	T23	MLM-05	Hydro Breccia	Exs1 + Ban1	0.16	616.69
T23-880	T23	MLM-05	Hydro Breccia	Exs1 + Ban1	0.30	678.55
T23-881	T23	MLM-05	Hydro Breccia	Exs1 + Ban1	0.18	625.54
T23-882	T23	MLM-05	Hydro Breccia	Exs1 + Ban1	0.18	626.94
T23-883	T23	MLM-05	Hydro Breccia	Exs1 + Ban1	0.18	623.45
T23-884	T23	MLM-05	Hydro Breccia	Exs1 + Ban1	0.28	672.58
T23-885	T23	MLM-05	Hydro Breccia	Exs1 + Ban1	0.18	626.70
T23-887	T23	MLM-05	Hydro Breccia	Exs1 + Ban1	0.46	727.49
T23-888	T23	MLM-05	Hydro Breccia	Exs1 + Ban1	0.16	612.09
T23-890	T23	MLM-05	Hydro Breccia	Exs1 + Ban1	0.16	616.58
T23-891	T23	MLM-05	Hydro Breccia	Exs1 + Ban1	0.35	696.60
T23-892	T23	MLM-05	Hydro Breccia	Exs1 + Ban1	0.19	633.62
T23-893	T23	MLM-05	Hydro Breccia	Exs1 + Ban1	0.32	691.11

ID	Transect	Sample	Mineralization Style	Texture	Mg [wt. %]	T°mean
T23-894	T23	MLM-05	Hydro Breccia	Exs1 + Ban1	0.57	762.82
T23-895	T23	MLM-05	Hydro Breccia	Exs1 + Ban1	0.16	612.58
T23-896	T23	MLM-05	Hydro Breccia	Exs1 + Ban1	0.34	693.14
T23-897	T23	MLM-05	Hydro Breccia	Exs1 + Ban1	0.24	659.47
T23-898	T23	MLM-05	Hydro Breccia	Exs1 + Ban1	0.14	605.80
T23-899	T23	MLM-05	Hydro Breccia	Exs1 + Ban1	0.19	633.86
T23-900	T23	MLM-05	Hydro Breccia	Exs1 + Ban1	0.14	601.22
1652	19	MLZ-01	Disseminated	Exs1 + Exs2	0.13	585.99
1724	130r	MLZ-12	Disseminated		0.10	587.48
T1-01	T1	MLM-06	Disseminated	Exs1	0.12	586.36
T1-02	T1	MLM-06	Disseminated	Exs1	0.13	595.92
T1-03	T1	MLM-06	Disseminated	Exs1	0.12	590.71
T1-04	T1	MLM-06	Disseminated	Exs1	0.12	590.51
T1-05	T1	MLM-06	Disseminated	Exs1	0.12	590.16
T1-06	T1	MLM-06	Disseminated	Exs1	0.12	585.32
T1-08	T1	MLM-06	Disseminated	Exs1	0.12	592.32
T1-09	T1	MLM-06	Disseminated	Exs1	0.12	586.98
T1-10	T1	MLM-06	Disseminated	Exs1	0.11	584.83
T1-11	T1	MLM-06	Disseminated	Exs1	0.12	588.10
T1-12	T1	MLM-06	Disseminated	Exs1	0.12	586.49
T1-13	T1	MLM-06	Disseminated	Exs1	0.12	585.15
T1-14	T1	MLM-06	Disseminated	Exs1	0.12	587.71
T1-15	T1	MLM-06	Disseminated	Exs1	0.08	555.17
T1-16	T1	MLM-06	Disseminated	Exs1	0.12	588.89
T1-17	T1	MLM-06	Disseminated	Exs1	0.12	589.72
T1-18	T1	MLM-06	Disseminated	Exs1	0.12	587.68
T1-19	T1	MLM-06	Disseminated	Exs1	0.12	591.34
T1-20	T1	MLM-06	Disseminated	Exs1	0.12	588.61
T1-21	T1	MLM-06	Disseminated	Exs1	0.13	593.23
T1-22	T1	MLM-06	Disseminated	Exs1	0.12	588.80
T1-23	T1	MLM-06	Disseminated	Exs1	0.12	589.30
T1-24	T1	MLM-06	Disseminated	Exs1	0.12	589.41
T1-25	T1	MLM-06	Disseminated	Exs1	0.13	594.10
T1-26	T1	MLM-06	Disseminated	Exs1	0.12	592.23
T1-27	T1	MLM-06	Disseminated	Exs1	0.13	592.55
T1-28	T1	MLM-06	Disseminated	Exs1	0.13	593.05
T1-29	T1	MLM-06	Disseminated	Exs1	0.13	593.83
T1-30	T1	MLM-06	Disseminated	Exs1	0.13	594.87
T3-51	T3	MLM-06	Disseminated	Exs1	0.12	589.60
T3-52	T3	MLM-06	Disseminated	Exs1	0.15	606.81
T3-53	T3	MLM-06	Disseminated	Exs1	0.14	604.28
T3-54	T3	MLM-06	Disseminated	Exs1	0.14	604.19
T3-55	T3	MLM-06	Disseminated	Exs1	0.15	612.00
T3-56	T3	MLM-06	Disseminated	Exs1	0.14	605.33
T3-57	T3	MLM-06	Disseminated	Exs1	0.14	600.96
T3-58	T3	MLM-06	Disseminated	Exs1	0.13	592.10
T3-59	T3	MLM-06	Disseminated	Exs1	0.12	588.50
T3-60	T3	MLM-06	Disseminated	Exs1	0.15	605.74
T3-61	T3	MLM-06	Disseminated	Exs1	0.13	595.50

ID	Transect	Sample	Mineralization Style	Texture	Mg [wt. %]	T°mean
T3-62	T3	MLM-06	Disseminated	Exs1	0.17	623.11
T3-63	T3	MLM-06	Disseminated	Exs1	0.12	587.88
T3-64	T3	MLM-06	Disseminated	Exs1	0.14	602.57
T3-65	T3	MLM-06	Disseminated	Exs1	0.16	613.76
T3-66	T3	MLM-06	Disseminated	Exs1	0.14	602.61
T3-67	T3	MLM-06	Disseminated	Exs1	0.14	600.92
T3-68	T3	MLM-06	Disseminated	Exs1	0.12	589.03
T3-69	T3	MLM-06	Disseminated	Exs1	0.13	592.85
T3-70	T3	MLM-06	Disseminated	Exs1	0.10	576.88
T4-71	T4	MLM-06	Disseminated	Exs1	0.07	543.52
T4-72	T4	MLM-06	Disseminated	Exs1	0.06	526.70
T4-73	T4	MLM-06	Disseminated	Exs1	0.07	547.08
T4-74	T4	MLM-06	Disseminated	Exs1	0.07	546.44
T4-75	T4	MLM-06	Disseminated	Exs1	0.07	543.66
T4-76	T4	MLM-06	Disseminated	Exs1	0.30	683.38
T4-77	T4	MLM-06	Disseminated	Exs1	0.07	538.12
T4-78	T4	MLM-06	Disseminated	Exs1	0.07	541.10
T4-79	T4	MLM-06	Disseminated	Exs1	0.18	633.02
T4-80	T4	MLM-06	Disseminated	Exs1	0.07	542.56
T4-81	T4	MLM-06	Disseminated	Exs1	0.07	544.52
T4-82	T4	MLM-06	Disseminated	Exs1	0.08	549.30
T4-83	T4	MLM-06	Disseminated	Exs1	0.06	532.01
T4-84	T4	MLM-06	Disseminated	Exs1	0.06	534.93
T4-85	T4	MLM-06	Disseminated	Exs1	0.06	531.88
T4-86	T4	MLM-06	Disseminated	Exs1	0.13	597.46
T4-87	T4	MLM-06	Disseminated	Exs1	0.07	537.95
T4-88	T4	MLM-06	Disseminated	Exs1	0.08	557.73
T4-89	T4	MLM-06	Disseminated	Exs1	0.06	526.44
T4-90	T4	MLM-06	Disseminated	Exs1	0.06	528.20
T6-111	T6	MLM-06	Disseminated	Exs1	0.06	527.50
T6-112	T6	MLM-06	Disseminated	Exs1	0.08	557.36
T6-113	T6	MLM-06	Disseminated	Exs1	0.07	547.67
T6-114	T6	MLM-06	Disseminated	Exs1	0.08	553.10
T6-115	T6	MLM-06	Disseminated	Exs1	0.07	542.72
T6-116	T6	MLM-06	Disseminated	Exs1	0.08	549.29
T6-117	T6	MLM-06	Disseminated	Exs1	0.08	552.47
T6-118	T6	MLM-06	Disseminated	Exs1	0.08	552.08
T6-119	T6	MLM-06	Disseminated	Exs1	0.08	549.61
T6-120	T6	MLM-06	Disseminated	Exs1	0.08	552.33
T6-122	T6	MLM-06	Disseminated	Exs1	0.07	538.83
T6-123	T6	MLM-06	Disseminated	Exs1	0.07	542.78
T6-124	T6	MLM-06	Disseminated	Exs1	0.07	537.92
T6-125	T6	MLM-06	Disseminated	Exs1	0.07	541.91
T6-126	T6	MLM-06	Disseminated	Exs1	0.08	556.16
T6-127	T6	MLM-06	Disseminated	Exs1	0.06	536.63
T6-128	T6	MLM-06	Disseminated	Exs1	0.07	547.25
T6-129	T6	MLM-06	Disseminated	Exs1	0.07	547.89
T6-130	T6	MLM-06	Disseminated	Exs1	0.25	664.41
T11-221	T11	MLM-03	Act-Px Veins	Other	0.09	565.70

ID	Transect	Sample	Mineralization Style	Texture	Mg [wt. %]	T°mean
T11-222	T11	MLM-03	Act-Px Veins	Other	0.08	556.23
T11-223	T11	MLM-03	Act-Px Veins	Other	0.09	565.87
T11-224	T11	MLM-03	Act-Px Veins	Other	0.09	559.60
T11-225	T11	MLM-03	Act-Px Veins	Other	0.10	574.78
T11-226	T11	MLM-03	Act-Px Veins	Other	0.10	569.97
T11-227	T11	MLM-03	Act-Px Veins	Other	0.10	568.48
T11-228	T11	MLM-03	Act-Px Veins	Other	0.11	577.39
T11-229	T11	MLM-03	Act-Px Veins	Other	0.12	585.83
T11-230	T11	MLM-03	Act-Px Veins	Other	0.10	575.42
T11-231	T11	MLM-03	Act-Px Veins	Other	0.06	535.06
T11-232	T11	MLM-03	Act-Px Veins	Other	0.11	576.78
T11-233	T11	MLM-03	Act-Px Veins	Other	0.12	584.01
T11-234	T11	MLM-03	Act-Px Veins	Other	0.11	576.25
T11-235	T11	MLM-03	Act-Px Veins	Other	0.10	573.14
T11-236	T11	MLM-03	Act-Px Veins	Other	0.11	579.96
T11-237	T11	MLM-03	Act-Px Veins	Other	0.11	577.96
T11-238	T11	MLM-03	Act-Px Veins	Other	0.10	572.98
T11-239	T11	MLM-03	Act-Px Veins	Other	0.11	577.82
T11-240	T11	MLM-03	Act-Px Veins	Other	0.10	567.58
T11-241	T11	MLM-03	Act-Px Veins	Other	0.11	580.78
T11-242	T11	MLM-03	Act-Px Veins	Other	0.11	576.44
T11-243	T11	MLM-03	Act-Px Veins	Other	0.20	637.67
T11-244	T11	MLM-03	Act-Px Veins	Other	0.11	576.65
T11-245	T11	MLM-03	Act-Px Veins	Other	0.10	574.44
T11-246	T11	MLM-03	Act-Px Veins	Other	0.11	578.42
T11-247	T11	MLM-03	Act-Px Veins	Other	0.10	573.29
T11-248	T11	MLM-03	Act-Px Veins	Other	0.11	581.84
T11-249	T11	MLM-03	Act-Px Veins	Other	0.08	552.97
T11-250	T11	MLM-03	Act-Px Veins	Other	0.11	582.76

Tabla Suplementaria 5: Resumen estadístico de los análisis EMPA realizados en magnetita.

Variable	Si	Al	Na	Mg	Ti	Ca	K	Fe	Cr	V	Mn	Zn	Cu	Ni
	[wt. %]	[wt. %]	[wt. %]	[wt. %]	[wt. %]	[wt. %]	[wt. %]	[wt. %]	[wt. %]	[wt. %]	[wt. %]	[wt. %]	[wt. %]	[wt. %]
CDL	0.006	0.005	0.021	0.009	0.007	0.003	0.004	0.009	0.006	0.007	0.007	0.014	0.011	0.012
Total (1172) : Minimum	0.00	0.01	0.01	0.06	0.02	0.00	0.00	51.12	0.00	0.08	0.01	0.00	0.00	0.00
Total (1172) : Maximum	5.89	3.41	1.25	3.90	11.22	5.76	1.22	76.08	0.05	0.66	0.55	0.10	0.01	0.01
Total (1172) : Mean	0.23	0.39	0.16	0.77	0.43	0.05	0.02	69.42	0.00	0.29	0.07	0.01	0.00	0.00
Total (1172) : Median	0.07	0.37	0.03	0.75	0.28	0.00	0.00	70.15	0.00	0.29	0.07	0.01	0.00	0.00
Total (1172) : Range	5.89	3.40	1.24	3.85	11.21	5.76	1.22	24.95	0.04	0.59	0.54	0.10	0.01	0.01
Total (1172) : Standard Deviation	0.40	0.23	0.20	0.51	0.77	0.19	0.06	2.06	0.00	0.17	0.04	0.01	0.00	0.00
Massive Mag : Count	548	548	548	548	548	548	548	548	548	548	548	548	548	548
Massive Mag : Minimum	0.00	0.07	0.01	0.52	0.02	0.00	0.00	56.02	0.00	0.09	0.02	0.00	0.00	0.00
Massive Mag : Maximum	2.43	1.09	1.06	2.48	5.44	0.39	0.81	71.13	0.00	0.50	0.55	0.02	0.00	0.01
Massive Mag : Mean	0.28	0.35	0.26	1.06	0.21	0.04	0.01	69.20	0.00	0.31	0.08	0.01	0.00	0.00
Massive Mag : Median	0.16	0.43	0.34	1.07	0.24	0.01	0.00	68.99	0.00	0.41	0.08	0.00	0.00	0.00
Massive Mag : Range	2.43	1.02	1.05	1.96	5.42	0.39	0.81	15.11	0.00	0.41	0.53	0.02	0.00	0.01
Massive Mag : Standard Deviation	0.32	0.21	0.21	0.34	0.38	0.06	0.04	1.64	0.00	0.15	0.03	0.00	0.00	0.00
Act-Px-Mag Veins : Count	237	237	237	237	237	237	237	237	237	237	237	237	237	237
Act-Px-Mag Veins : Minimum	0.00	0.17	0.01	0.25	0.12	0.00	0.00	51.12	0.00	0.26	0.02	0.00	0.00	0.00
Act-Px-Mag Veins : Maximum	3.52	1.24	0.94	3.90	11.22	0.91	0.24	71.27	0.00	0.66	0.33	0.07	0.00	0.01
Act-Px-Mag Veins : Mean	0.29	0.47	0.16	0.98	0.61	0.08	0.02	68.58	0.00	0.41	0.08	0.01	0.00	0.00
Act-Px-Mag Veins : Median	0.11	0.40	0.04	0.84	0.33	0.02	0.00	69.65	0.00	0.36	0.07	0.01	0.00	0.00
Act-Px-Mag Veins : Range	3.52	1.07	0.93	3.65	11.10	0.91	0.24	20.15	0.00	0.40	0.31	0.07	0.00	0.01
Act-Px-Mag Veins : Standard Deviation	0.48	0.16	0.19	0.46	1.14	0.15	0.03	2.61	0.00	0.14	0.03	0.01	0.00	0.00
Hydro Breccia : Count	259	259	259	259	259	259	259	259	259	259	259	259	259	259
Hydro Breccia : Minimum	0.00	0.16	0.01	0.06	0.21	0.00	0.00	59.05	0.00	0.08	0.02	0.01	0.00	0.00
Hydro Breccia : Maximum	3.54	1.91	0.19	2.19	7.27	0.81	0.36	71.38	0.01	0.15	0.46	0.10	0.00	0.00
Hydro Breccia : Mean	0.11	0.43	0.03	0.28	0.70	0.03	0.03	70.15	0.00	0.11	0.05	0.01	0.00	0.00
Hydro Breccia : Median	0.02	0.36	0.02	0.20	0.39	0.00	0.00	70.85	0.00	0.11	0.04	0.01	0.00	0.00
Hydro Breccia : Range	3.54	1.75	0.18	2.13	7.06	0.81	0.36	12.33	0.00	0.07	0.44	0.10	0.00	0.00
Hydro Breccia : Standard Deviation	0.32	0.20	0.02	0.24	0.95	0.11	0.07	1.78	0.00	0.01	0.05	0.01	0.00	0.00
Disseminated : Count	98	98	98	98	98	98	98	98	98	98	98	98	98	98
Disseminated : Minimum	0.02	0.15	0.01	0.06	0.16	0.00	0.00	58.35	0.00	0.12	0.01	0.00	0.00	0.00
Disseminated : Maximum	5.89	3.41	1.25	1.86	3.67	5.76	1.22	76.08	0.05	0.64	0.29	0.08	0.01	0.00
Disseminated : Mean	0.12	0.38	0.04	0.14	0.59	0.08	0.02	70.04	0.01	0.43	0.04	0.01	0.00	0.00
Disseminated : Median	0.02	0.34	0.02	0.12	0.49	0.00	0.00	70.69	0.01	0.36	0.02	0.01	0.00	0.00
Disseminated : Range	5.87	3.26	1.24	1.80	3.51	5.76	1.22	17.73	0.04	0.52	0.28	0.07	0.01	0.00
Disseminated : Standard Deviation	0.63	0.39	0.12	0.19	0.54	0.59	0.12	2.32	0.01	0.12	0.06	0.01	0.00	0.00
Act-Px Veins : Count	30	30	30	30	30	30	30	30	30	30	30	30	30	30
Act-Px Veins : Minimum	0.06	0.01	0.01	0.06	0.03	0.00	0.00	71.39	0.00	0.08	0.01	0.01	0.00	0.00
Act-Px Veins : Maximum	0.21	0.04	0.17	0.20	0.09	0.13	0.00	71.88	0.00	0.15	0.02	0.01	0.00	0.00
Act-Px Veins : Mean	0.11	0.02	0.03	0.11	0.06	0.02	0.00	71.77	0.00	0.12	0.02	0.01	0.00	0.00
Act-Px Veins : Median	0.09	0.01	0.03	0.11	0.06	0.00	0.00	71.80	0.00	0.12	0.02	0.01	0.00	0.00
Act-Px Veins : Range	0.15	0.03	0.16	0.14	0.06	0.13	0.00	0.49	0.00	0.07	0.01	0.00	0.00	0.00
Act-Px Veins : Standard Deviation	0.05	0.01	0.03	0.02	0.02	0.03	0.00	0.11	0.00	0.02	0.00	0.00	0.00	0.00